Instituto Tecnológico y de Estudios Superiores de Monterrey

Campus Monterrey

School of Engineering and Sciences

Processing and characterization of UHMWPE-TiO$_2$ nanocomposites for the development of a zygomatic bone prosthesis manufactured by SPIF.

A thesis presented by

Rodrigo Ortiz Hernández

Submitted to the
School of Engineering and Sciences
in partial fulfillment of the requirements for the degree of
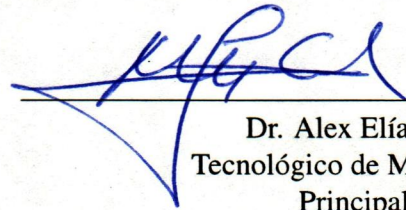
Master of Science

in

Nanotechnology

Monterrey, Nuevo León, December, 2019

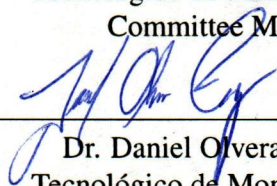# Instituto Tecnológico y de Estudios Superiores de Monterrey

Campus Monterrey

School of Engineering and Sciences

The committee members, hereby, certify that have read the thesis presented by Rodrigo Ortiz Hernández and that it is fully adequate in scope and quality as a partial requirement for the degree of Master of Science in Nanotechnology.

_____
Dr. Alex Elías Zuñiga
Tecnológico de Monterrey
Principal Advisor

_____
Dr. Oscar Martínez Romero
Tecnológico de Monterrey
Committee Member

_____
Dr. Daniel Olvera Trejo
Tecnológico de Monterrey
Committee Member

Tecnológico
de Monterrey

0 9 DIC 2019

Dirección Nacional de Posgrado
Dr. Rubén Morales Menéndez

_____
Dr. Rubén Morales Menéndez
Associate Dean of Graduate Studies
School of Engineering and Sciences

Monterrey, Nuevo León, December, 2019

i

Declaration of Authorship

I, Rodrigo Ortiz Hernández, declare that this thesis titled, "Processing and characterization of UHMWPE-TiO$_2$ nanocomposites for the development of a zygomatic bone prosthesis manufactured by SPIF." and the work presented in it are my own. I confirm that:

- This work was done wholly or mainly while in candidature for a research degree at this University.

- Where any part of this thesis has previously been submitted for a degree or any other qualification at this University or any other institution, this has been clearly stated.

- Where I have consulted the published work of others, this is always clearly attributed.

- Where I have quoted from the work of others, the source is always given. With the exception of such quotations, this dissertation is entirely my own work.

- I have acknowledged all main sources of help.

- Where the thesis is based on work done by myself jointly with others, I have made clear exactly what was done by others and what I have contributed myself.

Rodrigo Ortiz Hernández
Monterrey, Nuevo León, December, 2019

Dedication

To David, the best China's fast food restaurant chef and his sweet and sour chicken.

Acknowledgements

Processing and characterization of UHMWPE-TiO$_2$ nanocomposites for the development of a zygomatic bone prosthesis manufactured by SPIF.

by

Rodrigo Ortiz Hernández

Abstract

In the past years the use of nanotechnology for the development of new composite materials had become one of the most trending topics in the scientific community. Researchers around the world are working hard to prove that the addition of small quantities of nanoparticles (NPs) can be the differentiator that might change completely the way materials are seen nowadays. This master's program thesis focuses on bringing to medical disposition a novel material for craniofacial prosthesis capable of satisfying several of the biggest medical issues reported today in hospitals all over the world. In particular, the use of the developed UHMWPE-TiO$_2$ nanocomposite is, but not exclusively, aimed to be the principal material in the manufacture of a functional zygomatic bone prosthesis. For achieving this goal, UHMWPE-TiO$_2$ sheet nanocomposites were prepared using incipient wetting and compression molding processes at different concentrations (0.25 wt. %, 0.5 wt. %, 0.75 wt. % and 1 wt. %). Positive results were obtained through the dispersion of the TiO$_2$ NPs in a liquid solution observed at low concentrations ($<$0.75 wt. %). At higher concentrations, micro scaled agglomerations of NPs were seen with the use of SEM images which exhibit that the saturation point of TiO$_2$ NPs inside the polymeric matrix is situated between 0.75 wt. % and 1 wt. %. The degree of crystallinity and structural properties of the developed nanocomposites were investigated by X-ray diffraction and differential scanning calorimetry, the results presumes that the compression molding manufacturing procedure inhibits the normal crystallization phenomena of UHMWPE. It was observed the reduction in symmetry for the orthorhombic unit cells, found in(110) and (200), to monoclinic structures (001). Furthermore, FT-IR revealed the appearance of carbon-oxygen vibrational modes at 1740 cm^{-1} (C=O) and 1250 cm^{-1} (C-O) assuring a positive dispersion of TiO$_2$ NPs inside the polymeric matrix. Tensile tests and single point incremental forming processes were carried out indicating the enhance of the mechanical properties of the UHMWPE-TiO$_2$ nanocomposite superior to recent publications. Biological activity was analyzed using LIVE/DEAD Cell viability assays with favorable results showing almost null cytotoxicity. Finally a personalized, bio compatible, inert, resistant, cheap and light weighted zygomatic bone graft was crafted and mounted in a real partially damaged skull.

List of Figures

List of Tables

Contents

Chapter 1

Introduction and State of the Art.

1.1 Problem Statement

Technological developments are extremely important to help scientific society to generate knowledge among all the distinct worldwide researching teams. Nanotechnology, as a new branch of science has the goal and commitment to collaborate into different sectors of research with the idea of generating a new perspective of how things work and how colloquial process can be modified to behave in a completely different environment. However, generating knowledge is not the only goal of this thesis, it is expected to bring to medical disposition a disruptive prosthesis capable of satisfying one of the biggest medical issues reported today in all hospitals around the globe.

The zygomatic partial trauma or zygomatic fracture, figure 1.1, is defined as a discontinuity of hard and soft tissues such as bones, arteries and muscles in the front maxillofacial region of a patient. It is a result of a mechanical overload caused by an impact or excessive shear stress that overcomes the resistance of the affected and adjacent bone tissues [1]. In the actuality, the procedure that it has been followed to attack this particular traumas consists on an imminent surgical intervention of the patient with a partial replacement of the affected tissues. Most of the prosthesis used for this interventions do not fit correctly to the patients' physiognomy but they must be grafted immediately. If the pathology is not treated correctly within the first ten days of the accident/injury, several subsequent irreversible conflicts might occur. Cosmetic deformities, limited mandibular movements, respiratory difficulties, partial blindness and upper lip numbness to mention a few [2]. Additionally, cosmetic deformities can originate psychological depression disorders coming from the self esteem perception of the patient. Levine et al. studied the social and psychological post surgical impact of facial trauma on previously healthy patients. As a result of this publication, the study group statistically showed higher incidence in alcoholism, depression, unemployment, marital problems and physical appearance rejection in facial traumatized patients [3]. In Mexico, craniofacial traumas are located in the fourth place of mortality having 38.8 annual deaths per 100 thousands inhabitants. Affecting three times more frequently in middle age male population than females [4]. There are plenty of reasons that can lead to a zygomatic trauma but in the most relevant cases stand out the road traffic accidents, accidental falls, sport injuries and interpersonal violence. These accidents can occur at any age, any time and anywhere but with a stronger susceptible tendency of occurrence in male patients with an age range of 21 to 30

years old [1, 5]. Since this problematic is a pathology that can not be predicted or diagnosed previously to the injury and it requires a fast response. The need of developing a prosthesis with a fast personalized manufacture, bio compatible and capable of suiting the basic properties of the zygomatic bone is imminent.

Figure 1.1: Intraoperative view of the displaced fracture line at the zygomato-alveolar crest in a patient with a zygomatic bone fracture [6].

1.2 Facial Prosthesis Innovations.

Craniofacial prostheses for human procedures are described as an artificial device produced by different methods and materials with the purpose of replacing a missing part of the body which cannot be reconstructed nor repair. This specific type of prostheses are focused in fixing the anatomy of facial parts such as eyes, nose, ear, cheek and cranial plates with the primary objective of recovering its original tissue functionality or for personal esthetics. Prostheses are held in position with help of one of the two principal methods found in the market: adhesive and bone integrated implants. The adhesive approach is the same used in any day by day process which involves the need for sticking two different surfaces into a combined single material by creating an interface between both materials. This interface is made of a solution or substance which is normally fabricated with the goal of creating a physical or chemical stable interaction in the exposed superficial atoms. Several circumstances such as high humidity, poor adhesion, hydrophobic/hydrophilic surfaces or even the chemical body compositions of each patient can induce the possibility of detachment of the prosthesis. In addition, since that the prostheses are not secured under the skin and attached directly to the bone, they tend to wear out over the time which results in elevated maintenance costs. On the other hand the bone integrated implants, similar to the one proposed in this thesis, is a more reliable and secure option. For using this type of procedures, it is mandatory to at least do one surgical intervention to physically fix the prosthesis directly to any adjacent tissues (bones, muscles, ligaments, skin, etc.). By so doing, the prosthesis is fully restricted in movement and self protected/maintained with human immunological responses. They commonly use a couple of surgical biodegradable fixtures such as staples, screws, nails, tensors, to mention a few. In the case of bone tissue replacements the use of this type of fixtures allow the grafted material, depending on its nature, to exhibit one of three physicochemical scenarios [7]: Osteogenesis, Osteoconduction and Osseointegration. Osteogenesis referring to the capacity of

the new material to act as the precursor for the formation of new bone cells. Osteoconduction which is related with the capacitance of the material to propitiate the appropriate environment and support for human bone cells to grow inside the grafted material. And, osseointegration describing the possibility of adhesion of bone cells over the surface of the new material.

Recent activities in the development of new prosthesis for craniofacial environments are directed to the idea of introducing new concepts to reduce recovery time for patients, minimize surgery room time, avoid manufacturing excessive costs, achieve better mechanical properties and to find an appropriate interaction between the prosthesis and the human body. Today the use of 3D modelling techniques allow the development of personalized bone grafts with a faster production and with less geometrical errors. Typical manufacturing procedures used in the development of prosthesis are: single point incremental forming [8, 9], 3D printing [10, 11, 12], plastic injection, machining, thermoforming [13], and two stage casting, to mention a few. According to a review made by Philip Tack et al. it was illustrated that the use of 3D printing in the past years have been one of the most trending technologies used for the manufacturing of human prosthesis [14]. It was published that from the total amount of papers reviewed, 36.84% of the publications were spotted to attack the development of cranial and maxillofacial prosthesis. Additionally, Philip Tack was able to identify the positive impact of these new technologies on secondary medical procedures that results in beneficial advantages for patients. Unfortunately, the use of these processes increased the manufacturing costs on the personalized craniofacial prosthesis focusing to satisfy the needs of selected customers with high purchesing power with values from 200,000 MXN to 500,000 MXN depending on the complexity of the damaged tissue and the material by itself. As it was previously established, the use of a polymeric matrix reinforced with NPs, as the one proposed in this thesis, in addition with the use of SPIF manufacturing process allow to reduce the costs of production to an estimated price of 15,000 MXN plus transportation fees and research activity. Having this on mind, the socioeconomic impact factor of this project increases, with the scope of reaching a sector of the society who at this time is not consider to be suitable for this type of medical interventions.

The primary materials exert in the actuality for the development of craniofacial prosthesis involve the use of titanium, polyether ether ketone (PEEK), epoxide acrylate hydroxyapatite, hydroxyapatite, polymethyl methacrylate, polypropylene-polyester, polyethylene and acrylic based resins all of them with the clear objective of grafting a material with the appropriate biological properties to overcome the immunological human response. Before further it is extremely important to note out that even though the main scope of this thesis is entirely focused in the fabrication of a facial prosthesis it is not an impediment for the material to be used in different applications or sectors. In the next section, a more detailed presentation of the two elementary components of the designed material are being discussed in addition with the basic theory behind the characterization techniques used to study the behavior of the nanocomposite.

1.3 Ultra High Molecular Weight Polyethylene and Titanium Dioxide.

Polymers are defined as a group of macro organic molecules or carbon chains bonded together to form complex and continuous arrangements of atoms. The name polymer comes from **poly** which means many and **mer** related to units of atoms, from where the word polymer refers as the combination of many units of carbon bonded together. The use of polymers had a huge impact in the 1950's as a perfect alternative for conventional devices made of steel such as textile pickers, ship bumpers, furniture, to mention a few [15]. Due to the extensive diversity of polymers and the different manufacturing processes, it is almost impossible to generalize common properties for polymeric matrices. But, in contrast with metals, pure polymers have low density, strong resistance to corrosion, low thermal and electrical conductivity, low resistance, sound absorption, among others. Polymers are classified regarding its behavior under thermal environments, the amount and size of the molecules (molecular weight), the arrangement of the carbon chains, type and atom positions [Table. 1.1 and Fig. 1.2] [15, 16].
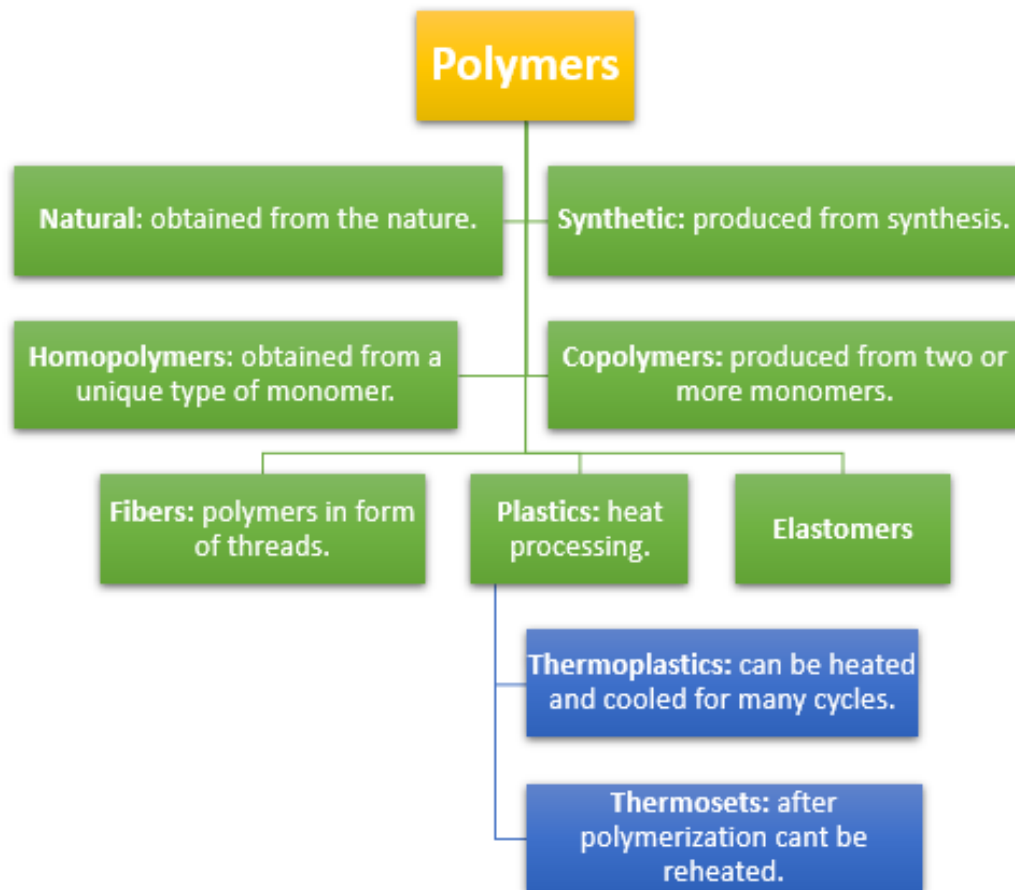
Figure 1.2: Brief overview of the classifications for polymers according to its structure, thermal behavior and/or production methods.

Table 1.1: General properties of polymers classified based on its thermal behavior.

	Thermoplastics	Thermosets	Elastomers
High Temperatures	Melts	Degrades	Degrades
Solvents	Soluble	Insoluble	Insoluble/ Swells
Structure	Linear	Cross-linked	Partial Cross-linked
Crystallinity	Semi-crystalline/Amorphous	Amorphous	Amorphous
Processing	No chemical reaction	Chemical reaction	Chemical reaction
Examples	PE, PP, PVC,	Resins	Rubber, Polybutadiene,
	Polyamide, Polyethers	(Epoxy, Phenol formaldehyde)	Synthetic rubber.

Nowadays the study related with polymers has reached levels of nano-molecular alterations that allow these chains of carbons to behave, under certain circumstances, as a substitution of complex and stronger materials. Adding nanotechnology to the internal constitution of polymeric structures has been used to develop new branch of hybrid materials with the mechanical and electrical properties of metals, while combining the low reactivity and density obtained from polymers. The important answers to the interrogative of why the scientific community keep looking for the best NPs capable of rising the mechanical, chemical and physical properties in polymers, instead of investing in the development of common metals such as titanium, is relatively simple: price, weight, biocompatibility and formability.

Ultra High Molecular Weight Polyethylene or consider from now on as "UHMWPE" is recognize to be a breed of polymeric structures, which consist of a dust, resin or flakes coming from a polymerization bulk at high temperatures and pressures. The main superior aspect to consider while having the opportunity of working with UHMWPE, compared with common polyethylene, is the amazing capability of compacting a high amount of atoms per unit volume. Leading to its high mechanical resistance, self lubricity, and the potential abrasion resistance of the material against a continuous force of friction. UHMWPE is commonly produced by a process known as addition polymerization which consists on the reaction of hydrogen peroxide with ethylene [Fig. 1.3]. After the addition of temperature and several catalyst, the double bonds found in ethylene mers are break down and then combined with more ethylene repetitive units, forming a partial carbon-hydrogen chain [Fig. 1.3 (b)]. This new chain is finally joined with hydroxide groups deriving from the hydrogen peroxide. The cycle is repeated until the ends of the carbon-hydrogen chains are closed with two hydroxide groups, synthesizing the molecule known as polyethylene [Fig. 1.3 (c)]. The molecular weight of the polyethylene chain can be controlled with the saturation of hydrogen peroxide and the amount of heat supplied to the system [16]. UHMWPE can reach up to a 400,000 carbon atoms per chain, increasing its molecular weight higher than six million of grams per mol. This represent a strong advantage compared to similar polymeric structures such as Low Density Polyethylene (LDPE), Linear Low Density Polyethylene (LLDPE), and High Density Polyethylene (HDPE), which have only a maximum molecular weight of 200,000 grams per mol [16]. Since that the mechanical, physical and chemical properties of polymers are strongly improved by the presence of higher molecular compact ratios. The difference in the molecular weight of these carbon-hydrogen chains facilitate to hold the idea that it is achievable to manufacture a stronger and reliable prosthesis made of UHMWPE rather than with a lower density polyethylene. On the other hand the limitations in the use of UHMWPE are

strictly limited to its poor behavior against thermal and mechanical stresses. Additionally, polyethylene composites present a strong tendency of degradation in contact with environmental factors such as UV light [17]. To overcome the deficiencies in the use of UHMWPE for facial prosthesis, TiO_2 NPs were dispersed inside the polymeric matrix with the objective of increasing the mechanical properties of neat UHMWPE while adding outstanding and beneficial characteristics to the final zygomatic bone graft.
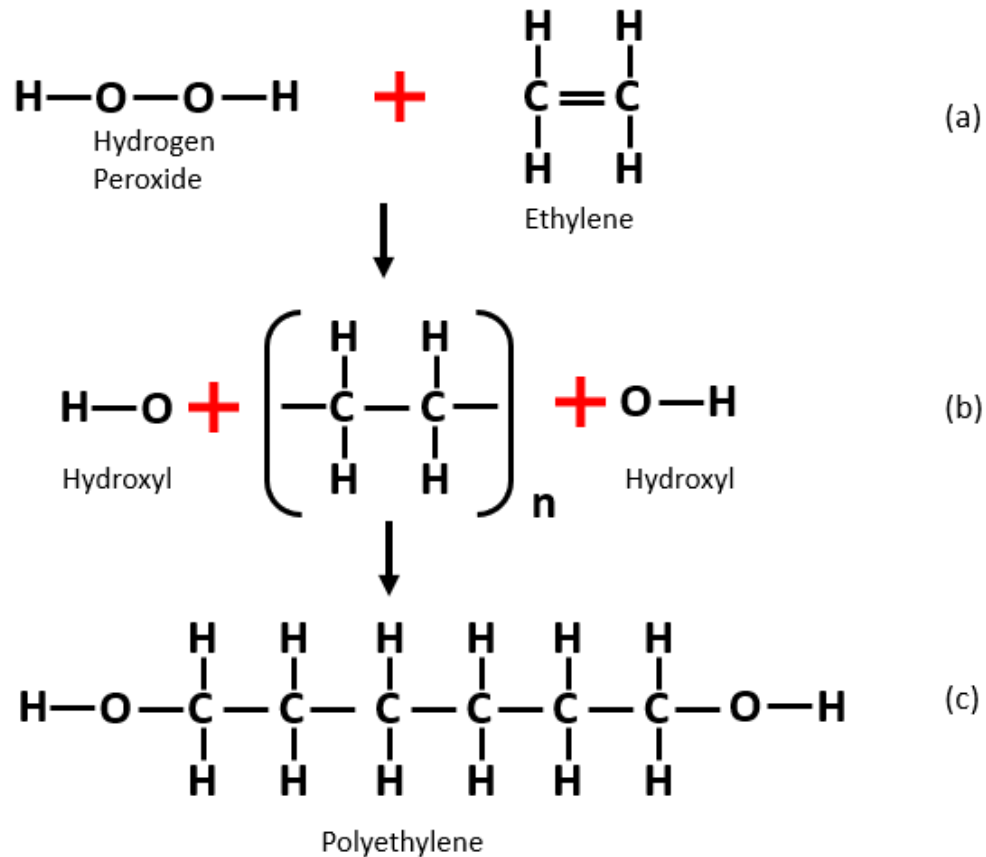
Figure 1.3: UHMWPE addition polymerization.

The use of TiO_2 began in the 20th century as a respond to the necessity of pigment paints, coatings, sunscreens, oral hygiene products among other commodities used for war activities. Titanium dioxide can be found around the world as a natural abundant resource obtained from the mining of ores that contain three of the main crystalline forms of TiO_2: rutile, anatase and brookite. The first industrial production started in 1918 in Norway, United States and Germany, gathering the raw material from one of the biggest mines situated in Sierra Leone, Western Africa [18]. Brookite phase is hardly produced in its pure form, commonly it is synthesized with the presence of anatase phase, it is natural made out of eight groups of TiO_2 per unit cell. As the rest of the phases, brookite phase has an octahedron internal structure but, with the peculiarity that the octahedron share edges and corners forming a structural composition named as orthorhombic structure. Anatase on the other hand is easily pure produced with techniques such as a sol-gel processes. It has four groups of TiO_2 per unit cell and presents a tetragonal structure with four shared corners resulting in a zigzag chains. Anatase

and brookite are both categorized to be metastable. This means that the system or body, at an existing level of energy, needs a small amount of power to start its transition to a stable state, this stable state is known as rutile phase. Rutile phase is the most stable phase and it is found with two groups of TiO_2 per unit cell in its composition. It shares two long edges of an octahedron internal structure forming linear molecular chains.

As mentioned before polymers might have suitable properties required for several applications in the market but they have a limit. Adding titanium dioxide NPs inside the composition of any polymer allow them to overcome those limitations and adapt its behavior to situations where strength, friction, conductivity and thermal interactions are mandatory. Moreover, a different characteristic important to note out in the use of UHMWPE-TiO_2 nanocomposites is the competence of decomposing bacteria and viruses due to the strong oxidizing properties of the titanium dioxide, acting as an ideal solution for medical procedures. Today there are known several synthesis procedures for the massive production of TiO_2 nanoparticles such as: hydrothermal method, solvothermal method, sol-gel method, direct oxidation, chemical vapor deposition, electro deposition and microwave method [19]. The typical nano scaled commercial presentation can be found as elongated tubes, nanosheets, nanofibers and nanoparticles with a maximum dimension of 100 nanometers. Publications related with the use of UHMWPE and TiO_2 are barely starting but a clear example of the increasing mechanical properties of commercial polyethylene (PE) with titanium dioxide nanoparticles are shown in [20]. In this study it is observed that depending on the increasing amount of the percentage of TiO_2 in polyethylene, mechanical properties such as the ultimate tensile strength, maximum elongation at break and elastic modulus are increased. The report illustrate as well that with an optimal concentration of 5 wt% TiO_2 in anatase phase, added by a master batch method, the elastic modulus increased up to 332 MPa, almost 1.5 times higher than the original polyethylene. In a more recent publication, the dispersion of TiO_2 NPs produced via a gelation/crystallization method in decalin and antioxidant solution at 150 °C, was able to report the highest increase in the elastic modulus of 610 MPa to 791 MPa. While reaching a maximum ultimate tensile stress of 35% higher than neat UHMWPE [21]. To understand if the combination of TiO_2 NPs with UHMWPE is suitable for the intended prosthesis application, it was mandatory to perform several characterization methods. A brief explanation of the theoretical approach and background of each characterization method is described in following paragraphs.

1.4 Experimental Characterization Equipment.

Since that the intended material is expected to have a controlled behavior inside a living organism, it is mandatory to subject the UHMWPE-TiO$_2$ composites to exhausting thermal, mechanical, chemical and biological tests assuring that the material will not be consider as a thread for the human body. In the next sections a brief explanation of the theory behind the characterization techniques used in this experimental research are described. Differential scanning calorimetry (DSC), x-ray diffraction (XRD), fourier-transform infrared spectroscopy (FT-IR), tensile mechanical tests, scanning electron microscopy (SEM), energy dispersive x-ray spectroscopy (EDX), single point incremental forming (SPIF) and surface roughness.

1.4.1 Differential Scanning Calorimetry.

Differential Scanning Calorimetry know as DSC, is strongly useful when rational quantities of samples are available for the study (5 to 10 mg). DSC technique has been modified through the years with several modules such as DSC-Microscopy, DSC-Photocalorimetry, DSC-Chemiluminescence to say a few. All of them with the primary objective of understanding the behavior of materials under different thermal environmental scenarios [22]. By definition according to the ASTM standard E473, DSC is consider to be a technique in which the heat flow rate difference into a substance and a reference. This change in heat flow is overview as a function of temperature while the sample is exposed to a controlled temperature variations [23]. The basic principle in the measurement of this change in temperatures observed along the reference and the samples is based in the law of conservation of energy for close systems [Equation 1.1]. Where ΔU is the change in internal energy; $\dot{Q}$ is related with the heat flow supplied or absorbed in the system and W the work done. From this statement, the development of two similar but somewhat different thermal analysis techniques were brought into science with the name of DSC (power compensation DSC and heat flux DSC).

$$\Delta U = \dot{Q} + W \tag{1.1}$$
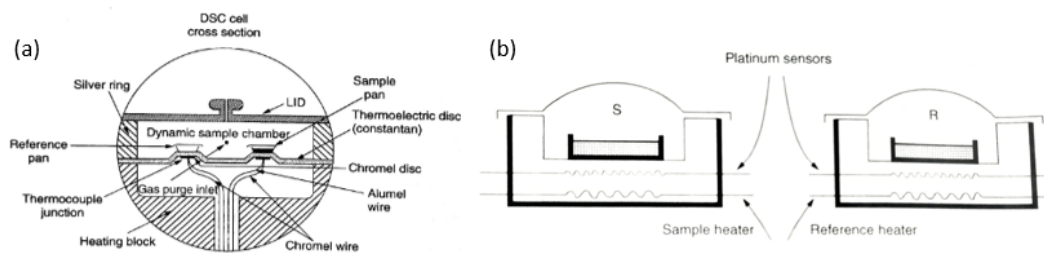
Figure 1.4: DSC configuration: (a) Heat flux DSC cell; (b) Power compensation DSC sample holder [22].

Heat Flux DSC is characterized to frequently have a critical cell [Fig. 1.4 (a)] located in an accessible spot situated in the top middle part of the device. It contains two identically sample holders (pan holders) divided by a controlled temperature bridge that acts as a heat

leak. Depending on the model, heat sensors and heaters (thermocouple junctions) are located bellow or above the pan holders. thermocouples are in charge of rising up the temperature of the chamber in a programmed increment tendency while sensors measure and determine the difference of temperature between the reference and the sample. Multiple control systems are located in the outside and inside of the furnace to assure a proper linear heating supply rate. Additionally, cooling systems can be added in order to decrease the temperature of the chamber in a more efficient way or when it is needed to work in cold environments bellow room temperature. Finally, inert gas can be pumped into the system through the purge gas inlets allowing to have a more accurate and controlled analysis [22].

The state of action in the heat flux cell is based on a thermal equivalence of the current Ohm's law were the current (I) equals to the voltage (V) divided by the resistance (R). In a thermodynamic approach, the current is expected to be the heat flow crossing thought the sample ($\dot{Q}$), the voltage is the change in temperature between the reference and the sample (ΔT). And finally (R) is to be the resistance opposed by the material [Equation 1.2] [24].

$$I = \frac{V}{R} \xrightarrow{analog} \dot{Q} = \frac{\Delta T}{R} \tag{1.2}$$

After combining the first law of thermodynamics [Equation 1.1] and the thermal equivalence of the Ohm's law [Equation 1.2], it is possible to calculate the change in internal energy observed in the sample in relation to the changes of temperatures between the sample and the reference through a defined period of time [Equation 1.3]. Two important constants must be added to the equation K_1 and K_2 related with the factory and the user calibration values for each sample [22].

$$\Delta U = \frac{\Delta T}{R} K_1 K_2 \tag{1.3}$$

Conversely, the operation of a heat flux DSC is focused in rising the temperature of a unique cell furnace containing the reference and the sample. If any thermal asymmetry occurs between the reference and the sample, being a phase transition or the detection of a different thermal capacity, a temperature difference will take place which will be detected by the sensors and used to calculate the heat exchange between the holders. Therefore, the thermal properties of the samples are determine. Since that the design of a heat flux DSC consists on a single furnace system, few disadvantages must be taken into consideration: poor sensitivity detected in small transitions, slower heating and cooling ramp rates, less accurate values for Cp and enthalpies [25].

The second type of DSC is called power compensation DSC, it was developed by Gray and O'neil in 1963 at the Perkin Elmer Corporation. In general terms, the final thermograms obtained from a heat flux DSC and a compensation DSC are relatively similar but it is achieved by completely different means. Contrary to the heat flux DSC, the power compensation DSC has two identical but separated reference and sample holders. Each particular cell has its own heater and sensor that will control independently the energy supplied [Fig. 1.4 (b)]. Both platinum/rhodium alloy holders are placed in a constant temperature block which can vary its temperature, depending on the model, from ≈ -196°C (liquid nitrogen as coolant) up to ≈ 400°C. It is controlled by two amplifiers which one of them (average amplifier) regulates the temperature of the block while the second amplifier (differential amplifier) regulates the power needed to have a thermal equilibrium between the reference and the sample holders.

The state of action in the power compensation DSC is focused in supplying energy to each individual cell by means of two identically heaters situated in the bottom of the sample holders. After the temperature is raised, if a thermal asymmetry is detected by the platinum sensors (difference in temperature), the programmer sends a signal to the average amplifier which tries to reduce it by heating or cooling at a constant linear heating rate [22]. The mathematical expression that governs this linear heating rate is expressed as:

$$T_{av} = \frac{T_s + T_r}{2} \tag{1.4}$$

where,

T_s is the temperature at the sample pan holder and T_r is the temperature at the reference pan holder. In addition to the mathematical expression used for the linear heating rate, the equations that describe the heat flow needed to achieve identical sample and reference temperatures in a power compensation DSC are:

$$\dot{Q}_r = \frac{\partial Q_r}{\partial t} = \lambda(T_r^{meas} - T_r) = W_{av} \tag{1.5}$$

$$\dot{Q}_s = \frac{\partial Q_s}{\partial t} = \lambda(T_s^{meas} - T_s) = W_{av} + W_d \tag{1.6}$$

where,

$\frac{\partial Q}{\partial t}$ is the heat flow rate, T^{meas} is the temperature of the reference and sample holders measured at the platinum thermometers, T is the true temperature, λ is the thermal conductivity, W_{av} is the power from the average amplifier and W_d the power coming from the differential amplifier in charge of regulating both temperatures.

Conversely, in power compensation DSCs, the holders keeping the sample and reference specimens are heated with an average amplifier to get a constant average heating rate. Since that the heat capacity between both specimens vary, a lagging thermal phenomena occurs, which is then compensated by the energy supplied from the differential amplifier. This heating compensation is proportional to the heat consumed or released in the sample. Therefore, it can be used to determine the thermal properties of the sample.

Disregarding what type of DSC is used and, with a dynamic temperature controlled heating rate ramp. It is possible to determine several information from the thermograms [Fig. 1.5] from which stand out the phase transitions, melting point, heat of fusion, crystallization temperature and glass transition temperatures. The phase transitions are defined as a thermodynamic system change that result as a modification of the temperature and/or pressure of a substance [26]. When the free energy in a thermodynamic system exhibits a partial derivative discontinuity is consider to be a first-order transition (melting, evaporation, sublimation, crystallization, deposition). For semi-crystalline polymers the sublimation and evaporation does not occur, due to the complexity of the carbon chains that can not be transformed into a gaseous phase without suffering degradation. The melting point, normally represented as (T_m), can be found at the highest spot of the melting peak which corresponds to the temperature needed to find a 50% of crystalline solid and 50% of isotropic liquid. Additionally to the

T_m, another important temperature normally situated at the beginning of the melting tempera-
ture curve can be found (T^{onset}). The onset temperature is defined as the temperature in which
the crystalline solid starts to absorb energy to change into an isotropic liquid. The heat of fu-
sion or enthalpy of fusion (ΔH_m) is the amount of heat that must be supplied into the system
to change 1 gram of substance from a crystalline solid to an isotropic liquid [26]. It can be
normally found after measuring the area under the curve of the melting peak. Analyzing the
thermogram from right to left (cooling), the crystallization temperature (T_c) is the temperature
where the energy in the system is reduced to prevent the excessive movement of particles in
an isotropic liquid, becoming a crystalline solid. At last, the glass transition temperature (T_g)
is the temperature in which it is possible to immobilize completely the particles moving in a
solid state until it change into a fragile crystalline solid. Formally, the glass transition state is
consider to be a second-order transition due to its jump of heat capacity [26].
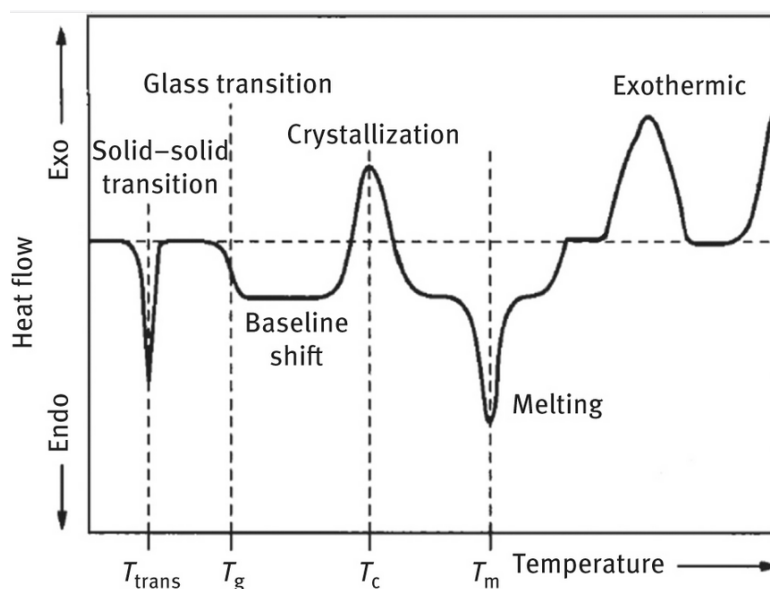
Figure 1.5: Schematic representation of DSC transition curves [27].

1.4.2   X-ray Diffraction.

Before starting with the definition and principles behind the use of X-ray Diffraction it is
important to describe few basic concepts that will facilitate the understanding of the results
obtained through the analysis. The first idea is related with the relevance of classifying solid
materials according to the regularity with which atoms or ions are positioned from one an-
other. If the atoms after solidification are located in recurrent three-dimensional patterns for
large atomic distances, it is defined as a crystalline material [28]. This patterns or atomic
arrangements are know as **crystal structures**. For metallic crystal structures the most com-
mon arrays are: Face Centered Cubic Crystal Structure (FCC), Body Centered Cubic Crys-
tals (BCC), and Hexagonal Close-Packed Crystal Structure (HCP). For polymers, the crys-
tal structures are simplified by defining the percentage of semi-crystals, group of polymeric

chains stack together (lamellae), in an ocean of free moving non ordered polymeric chains or amorphous content.

Often, given that the materials are not always uniform along the whole composition of the matter and since that there are plenty of possible crystal structures, it is convenient to subdivide the crystal structures in smaller repetitive arrangements of atoms, called **unit cells** [28]. These subdivisions are characterized to be parallelepipeds or prisms by having a set of three parallel faces. The unit cell is the basic configuration of a crystal structure and it defines the geometry and the atom positions of each material. The geometry is described in three edge lengths a,b,and c in addition with three interaxial angles α,β, and γ. These set of numerical values are also know as **lattice parameters**. The configuration of all the possible combinations of these parameters originate to seven distinct crystal systems: cubic, tetragonal, hexagonal, orthorhombic, trigonal, monoclinic, and triclinic [Fig. 1.6 (a)] [28]. The exact position and orientation of the unit cells are defined by a plane or set of parallel planes of atoms which intersect with the axes of a three dimensional coordinate system (x,y,z), known as Miller indexes [29]. Miller indexes are constructed in a manner that the reciprocals of the intersect points are conveniently written in a combination of three numbers (hkl) where "h" is the reciprocal of the intersection in the x coordinate, "k" is the reciprocal in the y coordinate and "l" the reciprocal at the "z" coordinate. If a plane is parallel to one of these axes, the intersection coordinate is defined as ∞ or $-\infty$ and its reciprocal as $\frac{(x/y/z)}{\infty/-\infty} = 0$. Taking as an example the plane illustrated in [Fig. 1.6 (b.2)], the coordinates (x,y,z) are ($\frac{1}{2}$,∞,∞) and its reciprocals or Miller indexes (hkl) are (2,0,0).
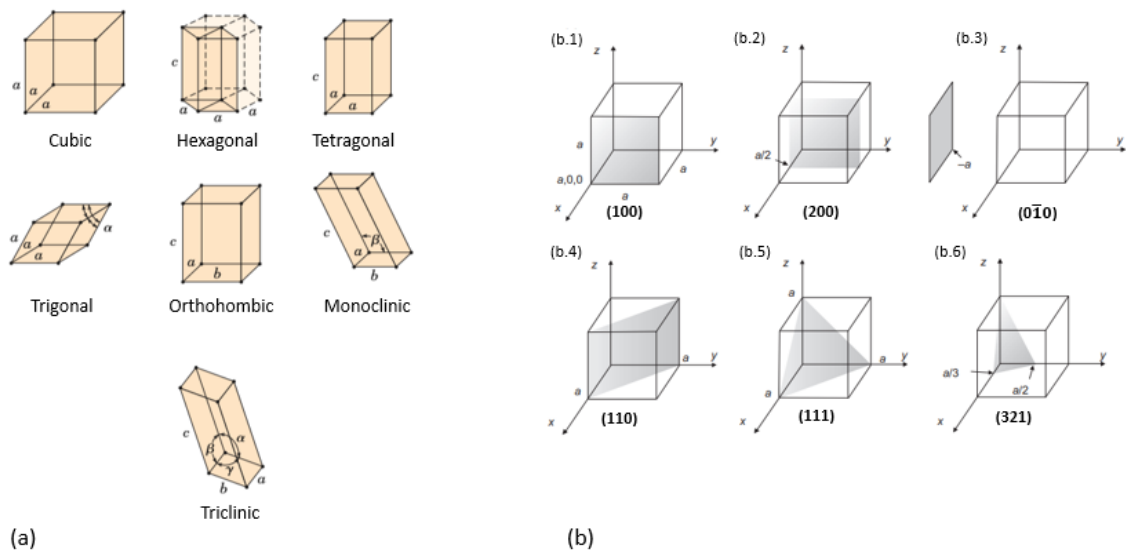
Figure 1.6: XRD basic concepts: (a) Crystal systems [28]; (b) Miller indexes [29]

.

Once the basic concepts were reviewed, the theory behind the instrument of XRD is settle in the well known principle first formulated by W.L. Bragg [Fig. 1.7 (a)], equation 1.7. Were it is established that the diffraction of any incident beam can only occur when the incident wavelength (λ), at a particular angle of diffraction (θ), is in the exactly same magnitude as the repeated rays projected in an adjacent plane separated by a distance (d) [30].

Addressing the subject in a more colloquial manner and by using the schematic [Fig. 1.7 (b)]. The technique known as X-ray diffraction is entirely focused in measuring the intensities, density electron presence, of X-rays diffracted from the collision of a primary X-ray beam with a set of imaginary planes that dissect a small unit fragment from a whole crystal at a particular angle. The configuration of all the diffracted intensities of the secondary beams against different possible angled planes positions is know as spectrum [31]. Depending on the material that it is being analyzed, the position signals of the crystalline diffraction planes and the intensities on each plane appearing in the spectrum might change. This variation is perfect for identifying the atomic contents of each molecular configurations.

$$\lambda = 2dsin\theta \tag{1.7}$$
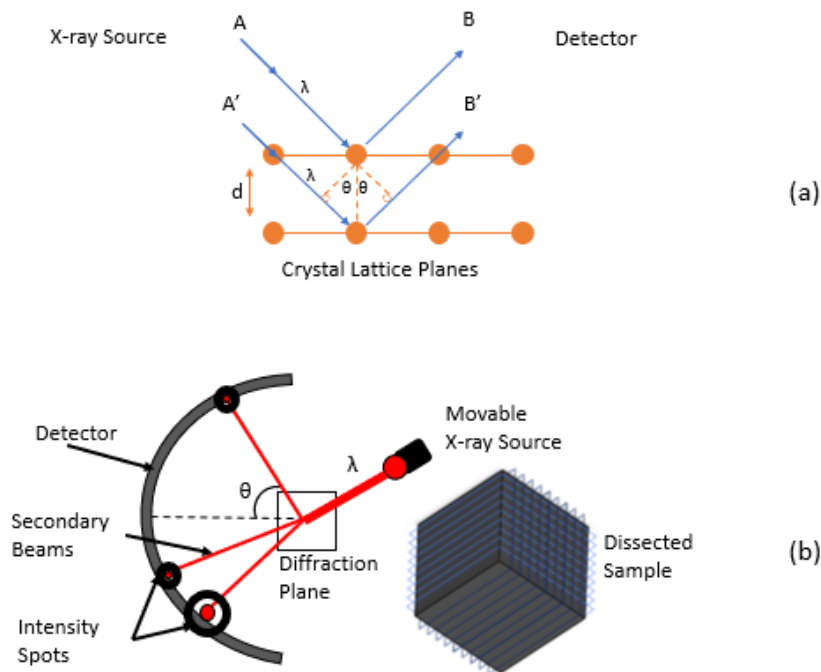
Figure 1.7: XRD fundamental schematic: (a) Wulff Bragg's law; (b) XRD analysis setup representation.

As it is observable, studying the quantitative analysis of phase compositions and the crystal structures of different materials is not a hard subject with the use of modern technology. Powerful instruments with extremely detailed databases can determine plenty of different morphologies in less than a 30 minutes test run. As a consequence, it is possible to identify the phase contents present in a sample by contrasting the diffraction plane intensities taken from the specimen, against the reference data provided by the scientific community. The complexity increases when the required study structure is not fully understood or defined in any database. In most cases these samples require extra experimental procedures or assumptions in the atomic arrangements and unit cell lattice parameters that will not result in an accurate measurement of crystallinity.

1.4.3   Fourier-Transform Infrared Spectroscopy.

A powerful spectroscopic technique found in the literature of many researchers around the globe in matter of material characterization, is the use of the Fourier transform infrared spectroscopy technique (FT-IR). This technique is widely reported by researchers due to its capacity of giving a better understanding of the internal structural arrangements in the molecules interacting with respect to one another and how they behave with their surroundings [32]. FT-IR method consists in the use of an infrared thin beam of light capable of stimulating the vibration of the molecules in the sample. The oscillation affecting the atoms of the molecules vibrate in different unique frequencies. This light frequencies are measured in wave number (cm^{-1}) corresponding to a particular functional group existing in the specimen. The sum of all the frequencies originate a fingerprint which can be used for determining the composition of the object. There are six principal molecular vibrations [Fig. 1.8], which corresponds to the motion of the atom in any of the three Cartesian coordinates. In addition, to simplify the complexity of the curve generated by the disruptive interference of the overlapping light waves or "Intergerogram". A mathematical procedure know as Fourier transform method, brakes down the complex data into an infrared spectrum of the sample. This spectrum is then displayed as a graph relating the percentage of transmittance (%T) against light frequency (cm^{-1}). The IR spectrum can be divided into two particular zones: the functional group region (4000 cm^{-1} - 1800 cm^{-1}), corresponding to the zone were it is possible to identify the specific absorption band signals for different functional groups and the fingerprint region (1799 cm^{-1} - 500 cm^{-1}) which relates the complex deformations of the molecules for each functional group.
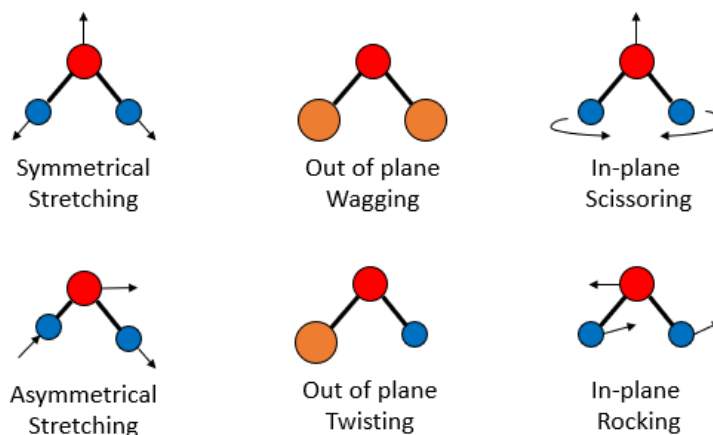
Figure 1.8: Different configurations for molecular vibrations.

In a FT-IR measuring instrument [Fig. 1.9], the infrared light ray first is crossed through an optical splitter dividing it into two halves. The first beam hits a fixed mirror which determines the constant pulse of emission generated by the IR source. The second beam is projected in a movable mirror in charge of controlling the periodicity of waves in the incident radiant power. Both halves are then converged in a new single distorted beam with intensity and periodicity defined by the user. The converged beam is reflected through a series of mirrors into a shutter and a filter with the single objective of driving the emission into a localized-clean beam. The surface of the sample is reached by the ray in a partial 90 degrees

angle. When the atoms in the molecules are hit by the light, the molecules start to vibrate absorbing part of the energy transmitted by the ray. This absorption is scanned by the detector or sensor that will then convert it to a ratio of the radiant power transmitted by the sample (I) over the radiant power incident on the sample (I_o) [Equation. 1.8] [33]. By doing so, the IR spectrum can be displayed and the signals can be correlated with worldwide databases.

$$A = log_{10}\left(\frac{1}{T}\right) = -log_{10}(T) = -log_{10}\left(\frac{I}{I_o}\right) \tag{1.8}$$
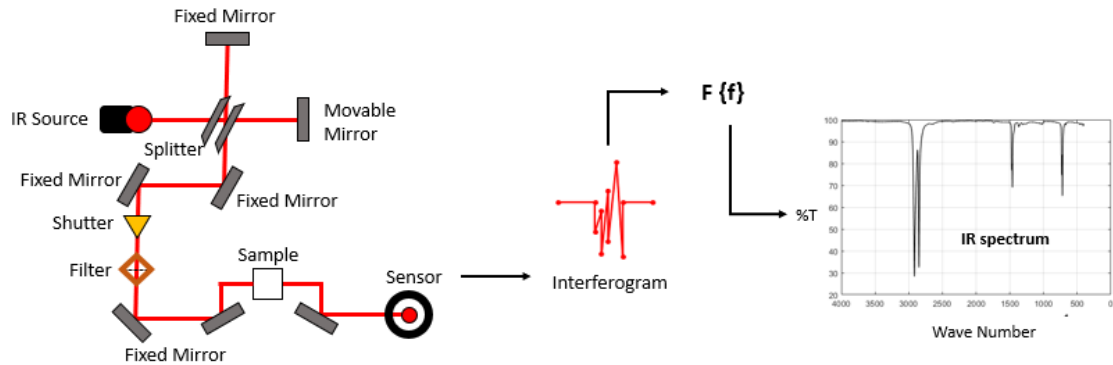
Figure 1.9: FT-IR optics and signal harvest flow diagram.

1.4.4 Tensile Mechanical Tests.

The behavior of the tensile properties is an obligated test that must be perform in almost all characterizations. The analysis covers the study of the resistance in a material under static and slowly dynamic forces. It is commonly used by the community since it is possible to gather plenty of information at a relative low cost and fully standardized methods. It is extremely important to consider that there are two notable classifications among materials, materials following the Hookean behavior and the Non-Hookean materials. The distinction is made by the response of the molecular bonds against a constant compression or tension load. When the materials are subjected to an external load, the atoms are drive out of their equilibrium positions generating forces of attraction or repulsion of new atoms, expanding or compressing the internal structure of the material [34]. Hookean elastic materials are based in two principal conditions [35]: (1) stress in a material is only in function of the strain; (2) a deformed material under a constant load has the property to recover its original shape after the removal of the applied force, it can behave as a linear or non-linear recovery. In practice, different diagrams and results can be obtained depending on the morphology of the samples but, it is possible to observe few key changes that can monitor the mechanical properties of the test specimen. The stress-strain curve diagrams for Hookean materials are divided in three sections [Fig. 1.10 (a)]: elastic region, plastic zone and necking zone [15]. The elastic region corresponds to the section where the material recovers its unformed state when the applied force is removed (linear and non-linear). The plastic zone refers to the section of the diagram

where the sample deforms permanently with a constant stress. Last of all, the necking zone illustrate a particular moment where the stress and strain are large enough to force the rupture of the sample [15]. It is relevant to establish that these zones can be combined, elongated or modified depending on the nature of the internal/superficial arrangements of the samples and the external environmental conditions [Fig. 1.10 (b)]. The yield strength and the young's modulus are located in the elastic region of the stress-strain diagram. They explain the maximum stress allowed in material before a plastic deformation occurs and the linear stress-strain slope originated by the first elastic deformations of the material [36]. The ultimate tensile strength (UTS) is located in the plastic zone. It illustrates the highest stress permitted in the sample prior to failing caused by the necking or stretching of the cross-sectional area in the test tube. A huge emphasis must be made in the basic principle that the manufacturing process for this thesis, single point incremental forming, is entirely focused in the capacity of deformation or formability of the material before it finally breaks. For this reason the ultimate tensile strength and the elongation at break will be highlighted as fundamental mechanical properties for understanding the behavior of the dopant inside the polymeric matrix of our study.
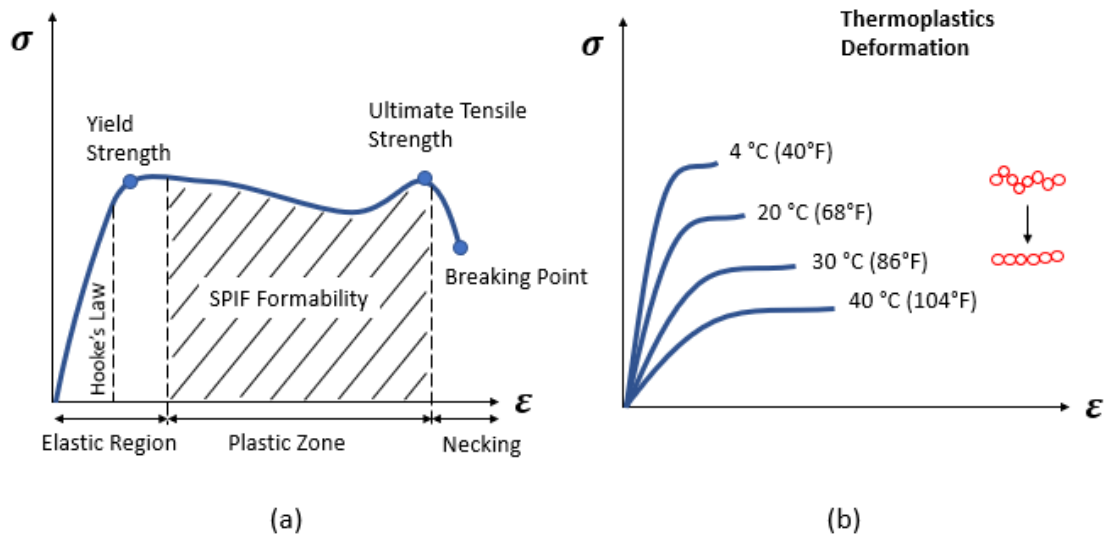
Figure 1.10: Stress-strain curve diagrams: (a) Diagram zones for metallic specimen; (b) Temperature response in thermoplastic matrices deformation against temperature.

$$\sigma = \mathbf{T}\mathbf{F}^{-1} \tag{1.9}$$

Tensile mechanical tests have the capacity to bring under simple extension and compression loads the internal structure of any material. This forces acting over the cross-sectional area of a material generate a well know principle which states that the engineering stress distribution (σ) found in a particular section of a solid body can be defined as the second order Cauchy's stress tensor ($\mathbf{T}$) multiplied times the inverse deformation gradient ($\mathbf{F}^{-1}$) [Equation. 1.9]. From where the deformation gradient is defined as the derivative of the displacement

field of a particle from its original position to a final deformed location, represented as (x), with respect to each component of the reference particle displacement (X) [Equation. 1.10].

$$\mathbf{F}_{ij} = x_{ij} = \frac{\partial x_i}{\partial X_j} = \begin{bmatrix} \frac{\partial x_1}{\partial X_1} & \frac{\partial x_1}{\partial X_2} & \frac{\partial x_1}{\partial X_3} \\ \frac{\partial x_2}{\partial X_1} & \frac{\partial x_2}{\partial X_2} & \frac{\partial x_2}{\partial X_3} \\ \frac{\partial x_3}{\partial X_1} & \frac{\partial x_3}{\partial X_2} & \frac{\partial x_3}{\partial X_3} \end{bmatrix} \tag{1.10}$$

By doing the inverse function of the previously stated matrix.

$$\mathbf{F}^{-1} = x_{ji} = \frac{\partial X_j}{\partial x_i} = \begin{bmatrix} \frac{\partial X_1}{\partial x_1} & \frac{\partial X_1}{\partial x_2} & \frac{\partial X_1}{\partial x_3} \\ \frac{\partial X_2}{\partial x_1} & \frac{\partial X_2}{\partial x_2} & \frac{\partial X_2}{\partial x_3} \\ \frac{\partial X_3}{\partial x_1} & \frac{\partial X_3}{\partial x_2} & \frac{\partial X_3}{\partial x_3} \end{bmatrix} \tag{1.11}$$

$$\mathbf{T} = \begin{bmatrix} T_{xx} & T_{xy} & T_{xz} \\ T_{yx} & T_{yy} & T_{yz} \\ T_{zx} & T_{zy} & T_{zz} \end{bmatrix} = \begin{bmatrix} \sigma_{11} & \sigma_{12} & \sigma_{13} \\ \sigma_{21} & \sigma_{22} & \sigma_{23} \\ \sigma_{31} & \sigma_{32} & \sigma_{33} \end{bmatrix} \tag{1.12}$$

Then, the Cauchy's stress tensor is described as a generic representation of the stresses form by the forces, also known as traction vectors (T), acting over each face of an infinitesimal volumetric cube [Fig. 1.11] [37]. Assuming that the chemical composition is constant through all the material, no change in temperature during the application of a load and, that the material is deformable, this volumetric cube can be used as a representation of the behavior in the whole body against a constant load. In an X,Y,Z coordinate system, each traction vector have three basic components pointing to every single coordinate axis, giving a total amount of nine traction vectors for a single volumetric cube, this is commonly known as the Cauchy's stress tensor [Equation. 1.12]. For conventional purposes, the T is substituted by σ and the subscript vectorial directions by a combination of two numbers. The first number defines the face of action while the second number refers to the component of the stress. Finally by plugging both matrices inside equation 1.9, the engineering stress can be calculated. Since that the tensile tests are only produced in an uni-axial direction, the components of the Cauchy's stress tensor in Y and Z axis are equal to 0. By doing so, equation 1.9 can be simplified as follows

$$\sigma = \frac{1}{\lambda} T_1 \tag{1.13}$$

where,

T_1 is the stress tensor in X direction and $\frac{1}{\lambda}$ is the inverse deformation gradient in only one direction.
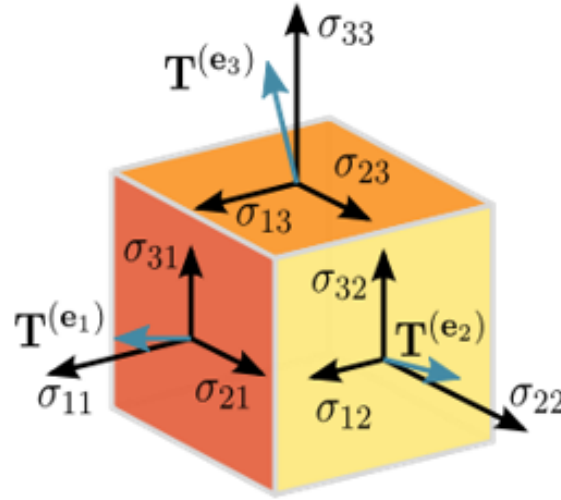
Figure 1.11: Infinitesimal volumetric cube subjected to axial loads: Traction vectors (T); Unitary vectors (e); Normal stresses acting perpendicular to each cube face (σ) [38].

1.4.5 Scanning Electron Microscopy and Energy Dispersive X-ray Spectroscopy.

The procedure of the scanning electron microscopy with energy dispersive X-ray spectroscopy (SEM-EDX) is one of the most used techniques applied to surface topography analysis. SEM-EDX is widely performed as a first approach since it is consider to be fast, non-destructive and low cost. It was originated since the discovery of the capacity of electrons to be deflected by magnetic fields in 1890s [39] and the replacement of the light source by a high electron beam with energy of 0.5 - 30 keV and a spot size less than 10 nm. The limit of resolution, defined as the minimum distance by which two structures can be separated and still appear as two distinct objects, is one of the most important parameters described by Ernst Abbe [39]. He proved that the wavelength of the illumination source is directly responsible of the limit resolution. This means that when the resolution limit is exceed, at a particular light source wavelength, the image blurs [40]. This phenomena is represented by the following Abbe's mathematical expression [Equation 1.14 and Fig. 1.12].

$$d = 0.612\frac{\lambda}{n sin\alpha} \tag{1.14}$$

where, d is defined as the resolution, λ is the wavelength of imaging radiation, n is the index of refraction between the point source and lens and α is the half angle of the light cone perceived by the objective.

After reviewing the basic principles of resolution used for the measurement of SEM, it
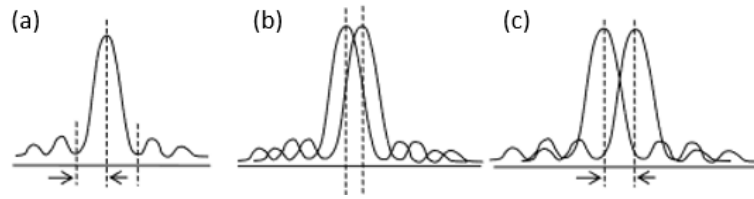
Figure 1.12: Abbe's resolution illustration: (a) Light source wavelength perfectly aligned (clear image); (b) Light source wavelength in transition; (c) Light source wavelength completely out of focus (blur image) [40].

is mandatory to explain that the images generated by SEM are dependent of the signals received from the collision of an incident electron beam with the sample. These interactions are divided in two groups, elastic interactions and inelastic interactions. Elastic interactions are consider to have null loss of energy after its collision with the sample and to have the capacity of scattering into different angles [40]. The inelastic interactions in the chamber refer to the incident electron collisions that looses energy after its encounter with the electrons and atoms of the sample. The amount of energy loss is proportional to the level of excitement of the electrons in the sample and the binding energy found between the electrons and the atoms. The absorbency of energy, as the result of the sample excitement, lead to the generation of secondary electron beams (3 - 5 eV) which are then traced by multiple sensors situated inside the vacuum chamber. The detectors in charge of analyzing the low energy secondary beams are called Everhart Thornely detectors which uses a scintillator that transforms the energy of the electrons into photons. These created photons travel through a series of Plexiglas and polished quartz pipes around the chamber untill they reach a photomultiplier tube. The quantum energy is then transform ones again into amplified electrons. A high resolution image is then produced matching the intensity of the secondary energy beams sensed in function of the position of the initial incident electron beam [41]. The image clarity is defined by the amount of secondary beams that can reach the detector. Multiple shadows might appear in the SEM display corresponding to diffracted secondary beams that could not reach the detector. Moreover, several additional signals are produced beyond the ones used for the imaging process: back scattered electrons (elastic interaction scattered in an angle grater than 90°), X-rays (used in EDX study), Auger electrons and cathodoluminescence [40]. Back scattered electrons (BSE) are also extremely useful as a source for detecting compositions and topographic information of the sample. BSE consists on elastic collisions (50 eV) between an electron and the sample atomic nucleus causing a backscattering event of 10-50% of the energy coming from the primary beam. Depending on the atom that it is being hit, the percentage of energy absorption is change leading to a powerful tool used to control the contrasts and shadows generated while imaging with secondary beams. Finally a quantifying method for identifying the elemental concentration, chemical composition, of each atom over the surface of the material is observed behind the use of X-rays. This analysis is well know as Energy Dispersive X-Ray Analysis which is based in the theoretical approach of forcing an inner shell electron to be displaced through the collision of a primary electron beam. The outer shell electrons are attracted to reestablish and balance the inner shell electron orbital space. Therefore, an X-ray photon emission and a quantifiable spectrum is generated. Once again depending on the atom that it

is being hit, the intensity of the X-ray photons change resulting in the possibility of measuring the chemical composition over the surface of a material [40].

1.4.6 Single Point Incremental Forming.

The post manufacturing process known as single point incremental forming consists on a progressively temperature-controlled deformation of the plastic integrity of a metal or polymeric sheet, known as blank [42]. The single point forming tool, guided by a CNC machine center tool path, apply a constant vertical and horizontal pressure in the material's surface. The material overpasses the elastic zone and then acquires its new shape according to the geometry programmed in the CAM software. Interesting advantages of using SPIF are based on the incredible capacity of manufacturing a rapid prototype, as well as an easy solution for small quantity productions without the need of investing in die blocks and punch plates in stamping procedures. Some aspects to consider while using this technique are that the formability of a metal/polymer sheet depends on several machine parameters that must be controlled in order to avoid material failures such as cracks and extremely low material thicknesses. Parameters such as initial material wideness, tool diameter, tool type, feedrate, direction of rotation, stepdown and spindle RPMs which are studied and compiled together in recent publications shown in [42, 43, 44]. Simultaneously researchers are working hard in the study of external factors that can affect positively the deformation of nano polymeric sheets such as the application of a thin dummy layer of a different material, mainly steel, over the composite to avoid the excessive intermolecular tension generated by the friction of the blank with the spindle of the CNC milling machine during SPIF procedures. This technique reduces and even avoids circumferential and torsion failures [42] but increases the radius of the tool and therefore the meridional stress over the wall.
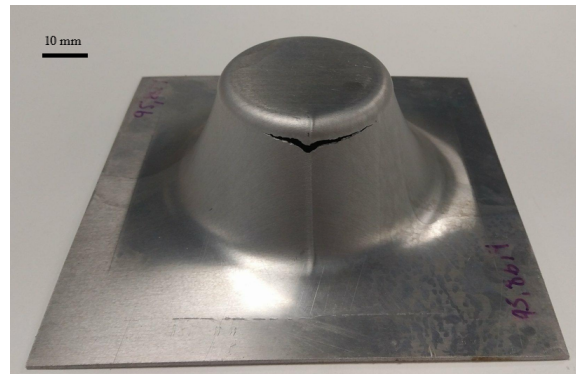
Figure 1.13: Circumferential failure originated by the excessive friction between the tool and the surface of the sheet blank.

Circumferential failures [Fig. 1.13], mainly occur during a SPIF manufacturing process when the friction between the spindle and the deformed material is high enough to force both components to stick together, ripping the blank in the direction of the spindle rotation [45]. On the other hand linear failures are caused by the meridional stress or known as longitudinal stress which refers to the force acting on an cross sectional area of the wall in the direction of the stepdown [44]. These types of problems can be solve by controlling the appropriate

speed, lubrication and movement of the spindle. Theoretical approaches have been made with the main objective of modelling the behavior of polymeric and metal sheets during SPIF procedures [46]. Marques et al. was able to precisely predict the stresses originated from the cold deformation of materials performed on a conventional CNC machining center to avoid circumferential and meridional failures. Some assumptions must be made so as to follow this modelling criteria: (1) the material deformed is assumed to be isotropic; (2) it must be rigid-perfectly plastic; and (3) the yield criteria is a modified version of the von Mises theorem proposed by [47, 48, 49]. After solving for the total sum of forces applied along the thickness, circumferencial and meridional directions of the deformation as well as the effects of the constant friction originated by the deforming tool. It is possible to define the stresses distribution during SPIF manufacturing processes: meridional stress (σ_Φ), circumferential stress (σ_Θ), and thickness stress (σ_t).

$$\sigma_\Phi = \sigma_1 = \frac{\sigma_y \sqrt{1 - \beta \sigma_{kk}}}{1 + \frac{t}{r_{tool}}} \tag{1.15}$$

$$\sigma_\Theta = \sigma_2 = \frac{1}{2}(\sigma_1 + \sigma_3 - \beta \sigma_y) \tag{1.16}$$

$$\sigma_t = \sigma_3 = -(\sigma_y \sqrt{1 - \beta \sigma_{kk}})(\frac{t}{r_{tool}} + t) \tag{1.17}$$

where,
β = normalized form of the strength-differential effect $(\sigma_{yc} - \sigma_{yt})/\sigma_y^2$.
t = thickness of the polymeric sheet.
r_{tool} = radius of the SPIF tool.
σ_y = yield stress.
σ_{yt} = yield stress in tension.
σ_{yc} = yield stress in compression.
$\sigma_{kk} = \delta_{ij}\sigma_{ij}$

1.4.7 Surface Roughness Analysis.

Surface morphology is a delicate subject that it is being in the ascendant of becoming one of the most important topics for tissue engineering science. The presence of protuberances, micro defects, coatings and even free radical bonds over the surface of the material can modify completely the chemical and mechanical behavior of any composite [50]. A real solid surface may appear to be ideally smooth, clean and polished but, even the most carefully treated surface is composed of a complex environment of multiple layers formed by external factors such as manufacturing processes, temperature and corrosion, to mention a few [Fig. 1.14]. No manufacturing process, no matter how precise, is capable of producing a fully 100% molecular flat surface on quotidian materials. Even the most refine material in the world has nano or micro deformities with heights that overpass the inter atomic distances of a molecular structure.

Surface roughness is commonly reported as the variation in the height of a surface in relation with a reference line. In some cases the reference line can be a set of parallel lines, which are then called as a surface map. In normal circumstances, these variations in height are
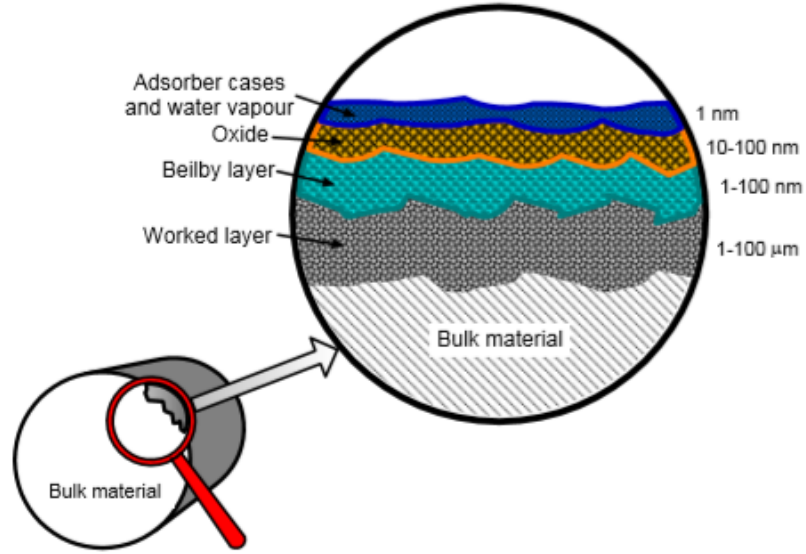
Figure 1.14: Schematic representation of a metal surface [50].

described by three main statistical descriptors, R_a/CLA (center line average), R_q/RMS (root mean square) and R_z (ten point height of irregularities) defined by the National Standards Institute (ANSI) and the International Standardization Organization (ISO) [52]. Additional parameters [Table. 1.2] are described with the main objective of having a better awareness of the multiple methodologies that can be used for understanding the complexity of a surface. Exemplifying the three parameters used for this research [Fig. 1.15] and tanking into consideration a random profile called k(x), it is possible to define a mean line (M), the top peaks and the valleys from where the area formed between the measured profile and the mean line can be calculated [Equation. 1.18 and Fig. 1.15 (a)] [52].

$$R_a = CLA = AA = \frac{1}{L} \int_0^L |k - m| dx \tag{1.18}$$

where, L is the length of the measured surface.
The variance observed in the surface can be expressed as:

$$\sigma^2 = \frac{1}{L} \int_0^L (k - m)^2 dx = R_q^2 - m^2 \tag{1.19}$$

where, σ is the standard deviation and R_q is the standard deviation of the profile height.

Since the intended final prototype of the composite is for medical grafts, it is important to understand the positive or negative consequences that can be originated from the interaction of different superficial geometries with human tissues. It is well studied that the presence of micro deformations in the surface of the materials in surgical prosthesis can propitiate the growth of human cells. In a recent study published by the Pennsylvania State University, researchers investigated the human osteoblastic cell response to different nano-topographies reaching promising results that in fact illustrate that the change in topography affect and even

Table 1.2: Conventional roughness parameters ISO I 13565-2 adapted from [51].

Parameter	Description
R_a	Profile average height
R_t	Maximum profile height
R_q	Standard deviation of the profile height distribution
R_p	Maximum profile peak height
R_v	Maximum profile valley depth
R_{DelA}	Average slope of the profile
R_{sk}	Skewness of the profile height distribution
R_{ku}	Kurtosis of the profile height distribution
R_{sm}	Mean spacing of the profile
R_{DelQ}	Root mean square slope of the profile
R_z	Average maximum height of the profile
R_{tp}	Bearing length ratio of the profile

controls the formation and growth of human cells [54]. Moreover, Woon Lee et al., experimentally proved that the adhesion of epithelial cells was higher over the surface of titanium with a 5 μm laser dimples than on polished titanium [55].
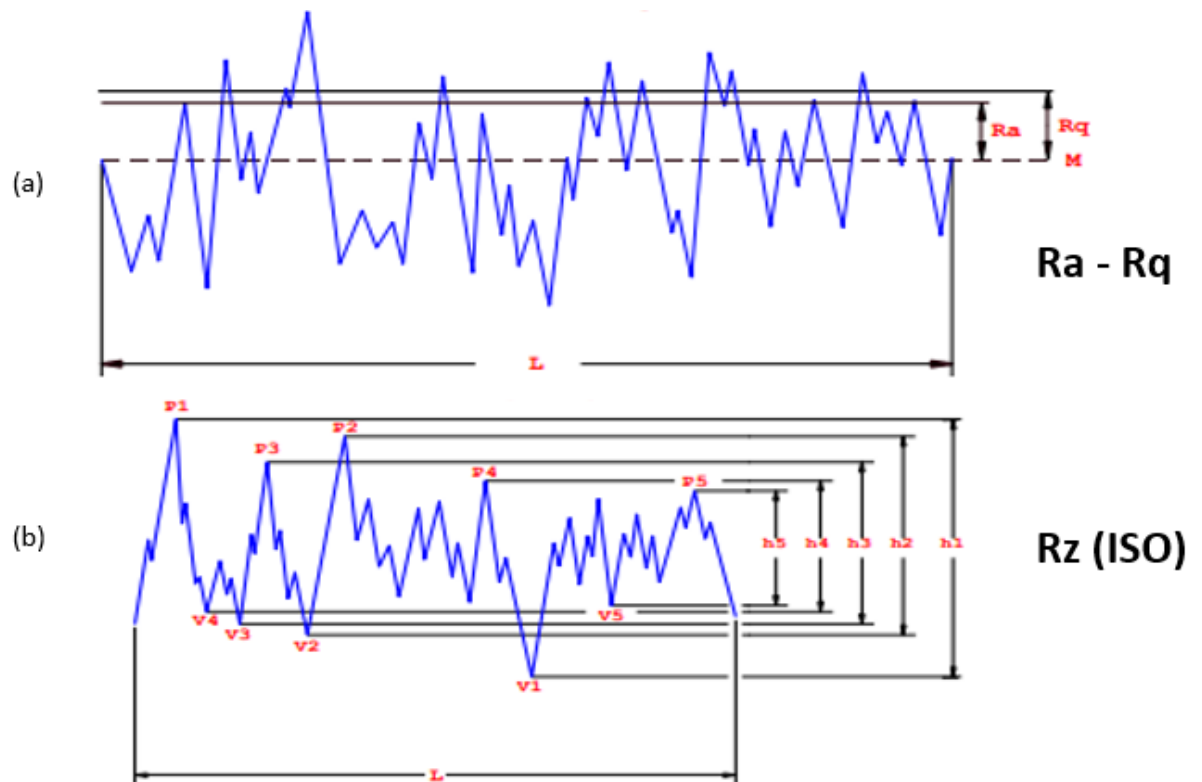
Figure 1.15: Schematic representation of the parameters used for this research: (a) Ra and Rq; (b) Rz (ISO) [53].

Chapter 2

Objectives and Hypothesis.

2.1 Hypothesis

The semi-crystallization of the UHMWPE structure is affected by the presence of TiO_2 NPs. The modified structure enhance the mechanical, biological and chemical properties of neat UHMWPE for the development of a zygomatic bone prosthesis.

1. Does the final mechanical and chemical properties of the UHMWPE-TiO_2 composites enhance the behavior of the neat UHMWPE matrix?

2. Will the proposed composite be suitable for cell adhesion and proliferation?

3. Will single point incremental forming be acceptable for the production of personalized facial bone grafts ?

4. Does the addition of TiO_2 NPs will modify the crystallization of the UHMWPE-TiO_2 composites?

2.2 Project Objectives and Scope

Adding up all the sections mentioned in the introduction as well as the pure nature of the subject, the main scope as a global goal is the replacement of recent human facial bone grafts with personalized smart material devices.This contribution will reduce the amount of medical interventions, lower the cost of a personalized prosthesis and most important avoid the excessive recovery time spent by the patient. The partial objectives to consider in this thesis are:

1. Proving that the addition of TiO_2 contribute to the crystallization phenomena of UHMWPE-TiO_2 composites. The modified structure enhance the mechanical, biological and chemical properties of neat UHMWPE.

2. Testing the formability during single point incremental forming procedures in UHMWPE-TiO_2 composites. Encouraging less geometrical errors than the ones observable in bare UHMWPE.

3. Validating that the UHMWPE-TiO_2 composite behave as a biocompatible environment appropriate for human cells growth.

We consider our hypothesis valid , increasing the mechanical response of the material tested prior to failure, proving an increment in the crystallization of the polymeric matrix, assuring a null toxicity environment for cell proliferation per concentration, and finally achieving the exact geometry of the patient's prosthesis.

2.3 Work Plan Schedule and Methodology

The work plan [Fig. 2.1] summarize the appropriate period of time for each step of the methodology in order to successfully satisfy the development of this thesis. The work plan started in January 2018 and will finish in December 2019. After this period if the objectives and goals are accomplished, a new work plan for the real implementation of the material and the prosthesis will be establish. A synthesis of the methodology of the experimental process is illustrated in figure 2.2. The project is divided in three main stages: "preparation of UHMWPE-TiO_2 sheet nanocomposites", "UHMWPE-TiO_2 nanocomposite characterization" and "prosthesis development and medical feasibility". On the first stage, the definition of the concentrations and the procedures used in the manufacture of the composite plates are established. The second stage of the methodology, is related with the idea of forcing the limits of the polymeric matrix by the use of mechanical, physical and chemical processes. All of them with the main objective of understanding the internal interaction of the titanium dioxide nanoparticles with the UHMWPE matrix and defining the composite properties achieved after the bonding of both materials. The final stage is the development of the real prototype in which the use of different designing and manufacturing techniques are used to produce a functional zygomatic bone graft.
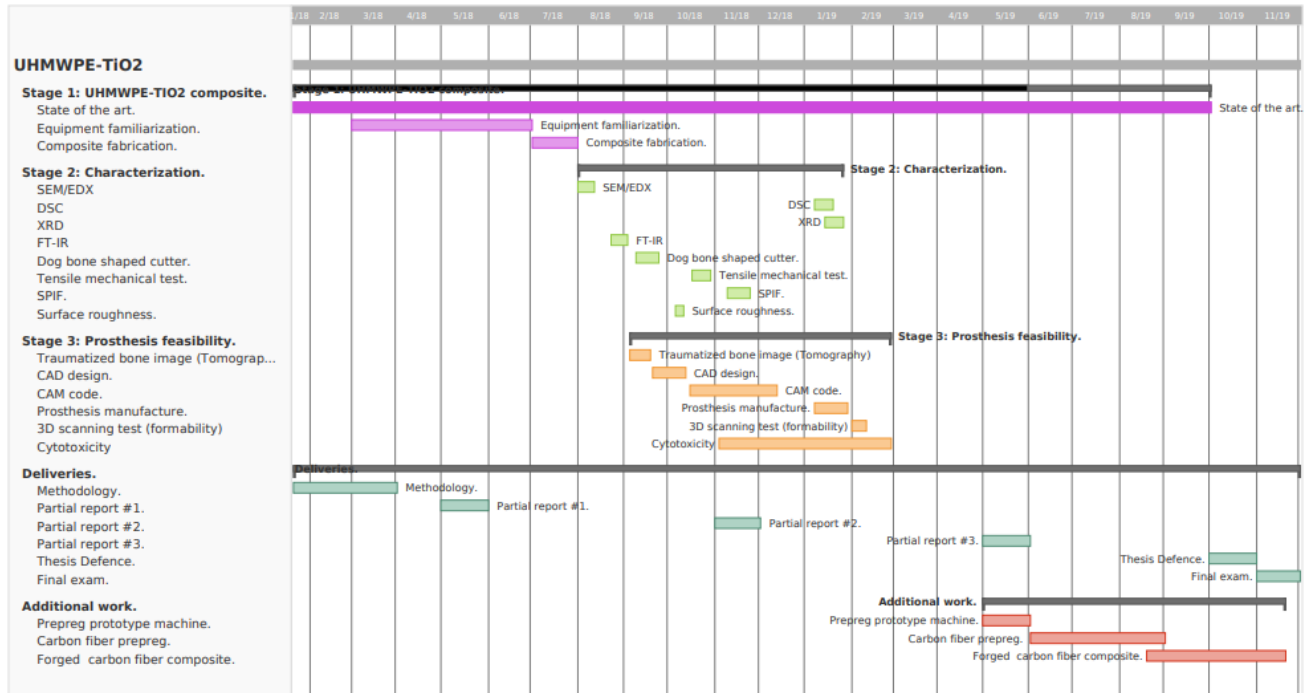
Figure 2.1: Work plan schedule for the development of this thesis.

Stage 1:	Ultrasonic dispersion of TiO$_2$ nanoparticles. (5 minutes, 30%)
Preparation of UHMWPE-TiO$_2$ sheet nanocomposites.	Incipient wetting. (TiO$_2$ + UHMWPE + 2-Propanol alcohol)
	Mechanical blend.
	Solution drying. (6 hours, 80°C)
	Compression molding. (25 minutes, 150°C, 22 psi)
Stage 2: UHMWPE-TiO$_2$ sheet nanocomposite characterization.	Differential scanning calorimetry. (Tm, Tc, ΔH_m)
	X-ray diffraction. (Degrees of crystallinity)
	Fourier-transform infrared spectroscopy. (Methylene bands analysis)
	Tensile mechanical tests. (Yield strength, UTS, Young's modulus, Strain)
	Scanning electron microscopy and energy dispersive x-ray spectroscopy.
	Single point incremental forming. (Generatrix, Parameters, Dynamometer)
	Surface roughness analysis. (Ra, Rz)
Stage 3: Prosthesis development and medical feasibility.	Computed tomography scan. (Patient's traumatized bone geometry)
	Computer aided design. (Prosthesis design)
	Computer aided manufacturing. (CNC codes)
	3D-scanning formability test. (GOM Inspect)
	Cytotoxicity. (Fibroblast cell growth)

Figure 2.2: Flowchart of the experimental procedure followed during this research.

Chapter 3

Experimental Methodology.

To begin with the first stage, step related with the manufacture of the polymeric reinforced plates, it is needed to define the amount of TiO_2 nanoparticles inside the polymeric structure. These concentrations are going to be critical for the development and behavior of the polymeric matrices. Therefore, a step by step procedure of the ultrasonic and mechanical dispersion of the nanoparticles inside the UHMWPE is described. In this stage a comparison between different composites proposed by few authors are discuss, as well as the reasons behind the selection of the exact quantities of grams and milliliters of reactants used in this research. Additionally, detailed information of the materials spent for each sample and the suppliers of the raw materials are mentioned in this section. At last, the parameters needed for the production of the reinforced plates via compression molding followed by a complete description of the characterization process methodology.

3.1   Materials.

The principal materials used in this study are Titanium (IV) oxide nanopowder (Anatase phase with an average particle size less than 25 nm) and UHMWPE (M_w 3,000,000-6,000,000), both purchased from Sigma-Aldrich (St. Louis, MO, USA). Isopropyl alcohol (2-Propanol alcohol, 99.5% purity grade) was bought from Jalmek Cientifica (Monterrey, NL, Mxico). The human fibroblast cell line (BJ, CRL-2522) was acquired from American Type Culture Collection (Manassas, VA, USA). At last, the Dulbecco's Modified Eagle Medium (DMEM/F12) supplemented with 10% fetal bovine serum was purchased from Gibco Invitrogen (Carlsbad, CA, USA). All the materials were used without any further purification. All the materials were used without any further purification.
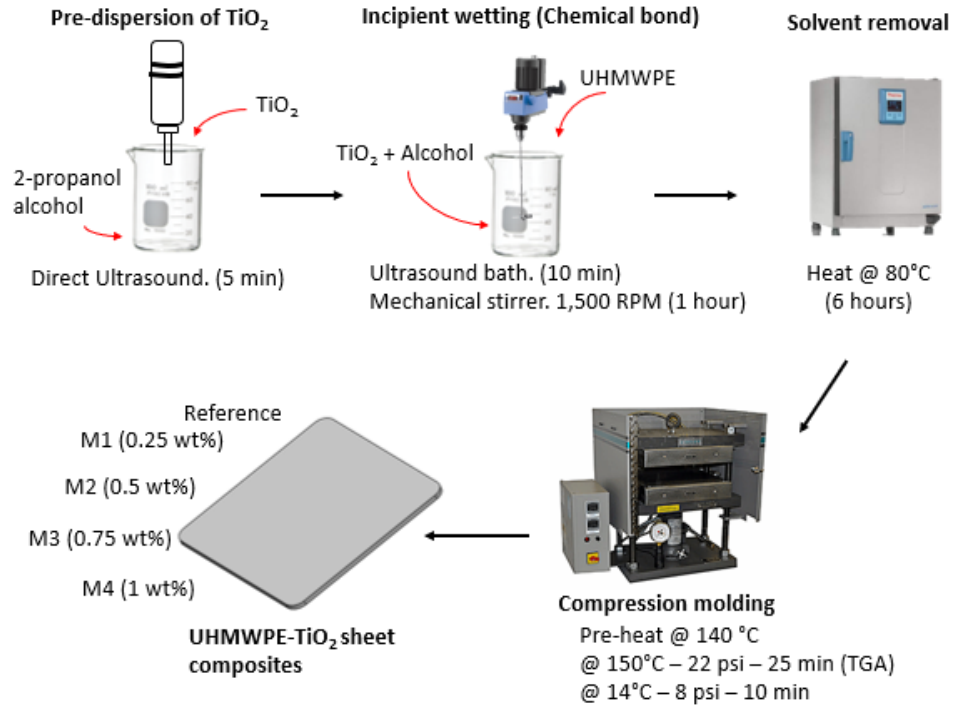
Figure 3.1: Schematic representation of the process used for the manufacture of the UHMWPE-TiO$_2$ nanocomposites.

3.2 Physical Synthesis.

In order to fully succeed with the development of the UHMWPE-TiO$_2$ composite it was mandatory to define the weight percentage (wt%) of the TiO$_2$ added to the mixture. Few researchers that had been working with TiO$_2$ molecules and polymeric matrices, mainly of polypropylene (PP) and low density polyethylene (LDPE) [20, 56, 57], reported an increasing behavior in the mechanical properties of the polymeric composites but with the peculiarity of a considerable sink after the 5 wt%. Studies reveal that the elastic modulus increased almost 1.5 times higher than the original polyethylene (PE), and the growth in tensile strength balanced around 20% to 26% more than its pure PE batch [20]. Taking this initial advises in consideration and to avoid excessive use of dopant, the exact NPs concentrations used for this research are shown in table 3.1. Incipient wetting and mechanical mixing were the processes chosen for encouraging the nanoparticles to disperse properly inside the composite. The appropriate concentration of TiO$_2$ was placed in a beaker with 100 ml of 2-propanol alcohol [Fig. 3.2 (a)] and then exposed 5 minutes to a direct tip ultrasound attack (30% of the maximum amplitude at 20KHz) [Fig. 3.2 (c)]. Both, attacked TiO$_2$ and 47 grams of UHMWPE are then poured together through a 10 minutes indirect bath (40 Hz) in a Cole-Parmer ultrasonic homogenizer tank [Fig. 3.2 (b)]. Furthermore, the samples were mixed for 1 hour at room temperature in an IKA RW20 mechanical stirrer at 1,500 RPM encouraging the particles to fully attach [Fig. 3.2 (d)]. Finally, the wet dusty sample was placed in an oven at 80°C for 6 hours to completely remove the solvent.

Table 3.1: Description of the amount of substances used for the preparation of the UHMWPE-TiO$_2$ nanocomposites produced by incipient wetting and a hot compression molding processes.

Sample	TiO$_2$ (mg)	wt %
Reference	$\cdots$	UHMWPE
M1	117.0	0.25%
M2	235.0	0.5%
M3	352.0	0.75%
M4	470.0	1.0%

3.3   Nanocomposite Plates Manufacture.

Manufacturing the reinforced polymer plates involve the use of a technique known as compression molding which refers to the use of a constant pressure and temperature to melt the polymer. The preheated open mold is filled up with a solid solution, dust or pellets, and then pressurized until the temperature of the mold reaches the melting temperature of the solution. As a difference from plastic injection molding were it is needed to work with close molds and a premelted material. This allowed the research to spend more time in testing and less hours in the design of a more complex mold. The parameters used for generating the blanks were taken from [58] and based in a TGA analysis [Appendix B] adapted to satisfy a manufacturing mold criteria and to work below the degradation temperature of the UHMWPE. The upper and lower steel molds with dimensions of 150 x 150 x 2 mm were preheated at 140°C in a CAVIER 4122 hydraulic heating press [Fig. 3.3 (c)]. The preheated mold is then removed from the heating source and opened to deposit a thin layer of acetate paper over the surface of the molds acting as a releasing agent between the steel and the melted composite [Fig. 3.3 (a)]. The UHMWPE-TiO$_2$ dust [Fig. 3.3 (b)] is now uniformly placed along the surface of the lower mold and compressed for 25 minutes under 150°C (above the melting temperature) with a constant load of 22 psi, at this point the mixture is fully melt and homogenized. Finally, the mold is cooled at 14°C with a load of 8 psi for 10 minutes from where the UHMWPE-TiO$_2$ plate is removed [Fig. 3.3 (d)]. The process is repeated for each concentration.

Stage 2 involves one of the most interesting steps in the production of the prosthesis. In these following sections it is possible to reproduce and understand how the human graft will behave against different scenarios. A brief explanation in the functionality of each technique is described as well as the methodology, parameters, followed for each test in our research. The study involve two thermal analysis (DSC and TGA), three mechanical tests (SPIF, traction and roughness) and three optical explorations (FT-IR, XRD and SEM).

3.4   Degree of Crystallinity in Polymers via DSC Analysis.

For our intended ideology of testing the crystallinity induced with the dispersion of TiO$_2$ NPs. The degrees of cristallinity (χ_c^{dsc}) were calculated in a power compensation DSC according to a well know principle which states that the enthalpy of fusion (ΔH_m) is found with the area under the curve formed by the phase transition of a semi-crystalline solid into an isotropic
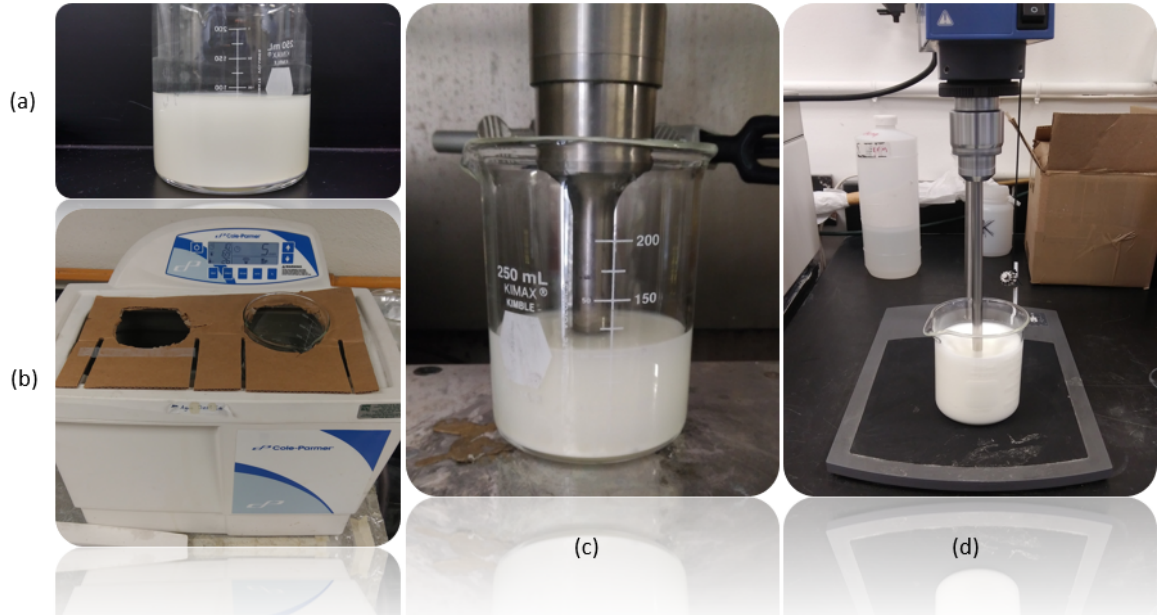
Figure 3.2: Physical synthesis: (a) Solution made of UHMWPE + TiO$_2$ NPs + 2-propanol alcohol; (b) Indirect ultrasonic bath for the dispersion of TiO$_2$ NPs inside the UHMWPE lamellae; (c) Direct tip ultrasonic attack helping the pre-dispersion of agglomerated TiO$_2$ NPs; (d) Mechanical stirrer IKA RW20 as a final dispersion mechanism.

liquid, exactly at the melting temperature (T_m) [59]. Divided by the standard enthalpy of fusion for a full perfect crystalline UHMWPE structure ($\Delta H_m^\circ = 289 Jg^{-1}$) [60]. Times the concentration of the dopant present in the matrix [Equation. 3.1].

$$\chi_c^{dsc} = \frac{\Delta H_m}{\Delta H_m^\circ (1 - w_t)} * 100 \tag{3.1}$$

The measurement of the melting temperature along with the change in enthalpy of fusion were evaluated in a PerkinElmer DSC 8000 [Fig. 3.5]. An approximate amount of 5 - 8 mg per UHMWPE-TiO$_2$ composite concentration (plate portion) were placed in several aluminum DSC sample holders [Fig. 3.4 (a)] with a total average weight of 30 mg (sample, pan and cover) [Fig. 3.4 (c)]. After weighing, the sample holders containing the nanocomposite, are then closed with a universal crimper press [Fig. 3.4 (b)] and placed inside the DSC chamber. The method involves an isothermal process for one minute at 30°C followed by a rise in temperature with a rate of 10°C per minute up to 180°C. After the sample is cooled at the same rate, the cycle is repeated once again to assure a proper thermal history [Fig. 3.4 (d)]. The DSC analysis curves presented in future sections for the material samples were carried out for the materials as received (first run data).
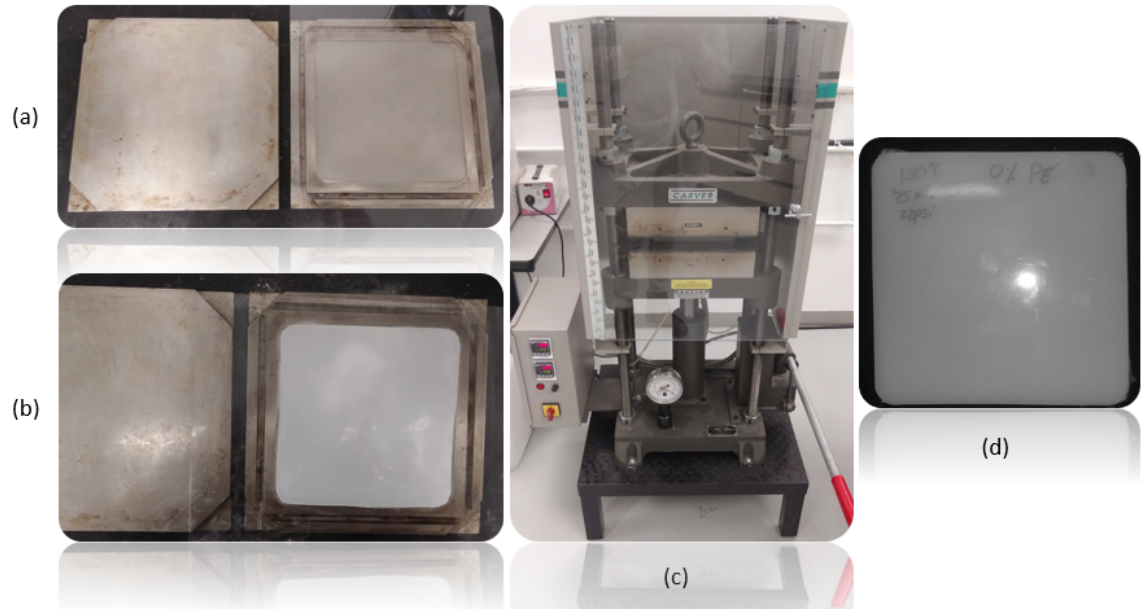
Figure 3.3: Nanocomposite plate manufacture: (a) Preheated open mold with acetate paper; (b) UHMWPE-TiO$_2$ dust placed over the surface of the bottom mold; (c) CAVIER 4122 hydraulic heating/cooling press; (d) UHMWPE-TiO$_2$ nanocomposite final plate.

3.5   Degree of Crystallinity in Polymers via XRD Spectra.

To solve this problematic it is possible to determine the crystallinity of a polymeric matrix by using the equation 3.2, which comes from the understanding of the Bragg-Brentano focusing geometry, where the total spectrum observed after an analysis of XRD is composed from different phases combined inside the sample. For an UHMWPE-TiO$_2$ composite, a crystalline and an amorphous component [Fig. 3.6]. Before further, it is important to establish that for using equation 3.2 it is mandatory to define the degrees of crystallinity, through a different characterization technique (DSC analysis equation 3.1), from a reference material with a similar composition and with the same manufacturing process. By so doing, the offset known as background or (β) in equation 3.2 can be established. This offset normally appears in almost all spectra due to the lost of diffracted X-rays caused by hard surface roughness, dust particles or even decalibration of the instrument [Fig. 3.6].

$$\chi_c^{dsc} = \chi_c^{xrd} = \frac{\sum I_C}{\sum (I_C + I_A)} + \beta \tag{3.2}$$

Taking our research as an example of the methodology that must be follow. A neat UHMWPE sample plate (20 x 20 x 2 mm) was mounted in a zero background sample holder plate [Fig. 3.7 (a)]. Care must be made to assure a flat upper surface, allowing to achieve a random distribution of lattice orientation and a proper interaction of the incident beam with the surface of the sample. Then, the sample holder is placed inside the sample stage [Fig. 3.7 (b)], which is located exactly between the X-ray source and the X-ray detector. This type of configuration allow to concentrate a uniform and controlled multi-angle X-ray attack over the surface of the material. It was measured in a PanAnalytical X'Pert Pro PW1800 at 45 mA and
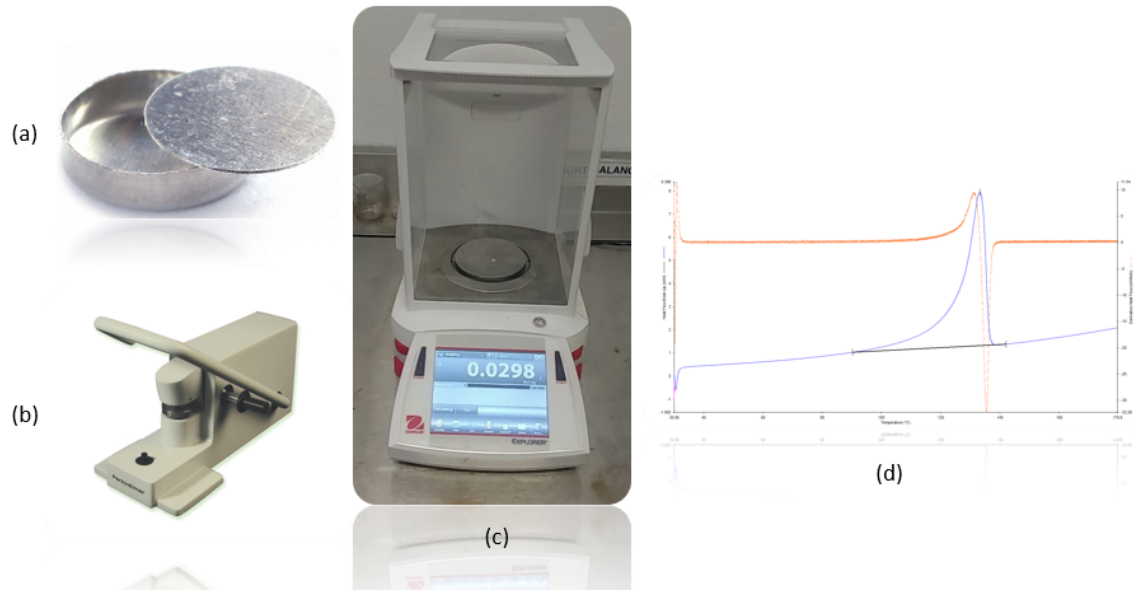
Figure 3.4: DSC preparation methodology: (a) Sample holders (pan and cover); (b) Universal crimper press used for closing the sample holders; (c) Portioning of UHMWPE-TiO$_2$ composites for DSC analysis; (d) Representative DSC analysis curves for UHMWPE-TiO$_2$ composites.

40kV [Fig. 3.7 (c)]. The data was collected in the 2Θ range of 10° to 40° with a scanning rate of 2°/min and using Cu-K_α radiation.

Once the analysis was performed, the spectrum resulting from this study [Fig. 3.6] illustrate the intensities related with the crystalline diffraction planes (I_C) and the amorphous content phase (I_A). The three components: I_C, I_A and χ_c^{dsc}, previously calculated with DSC, are plugged in the equation 3.2 from were the background constant beta can be isolated. This constant value is valid only for samples coming from the same manufacturing process and the same measuring conditions. Having said that, the samples corresponding to 0.25, 0.5, 0.75 and 1.0 wt % of TiO$_2$ were subjected to the same measuring parameters of the XRD analysis. The new intensities related to the crystalline diffraction planes and the amorphous content, of each dopant concentrations, were once again written in the same equation but now with the background that was previously calculated. As a result, the degrees of crystallinity with the XRD technique (χ_c^{xrd}) can be deduced.

3.6   Degree of Crystallinity in Polymers via FT-IR Spectrum.

In 1989, Hagemann and his coworkers decided to evaluate the possibility of understanding the process of crystallization and its dependence of temperature in a semi crystalline polymer. The research is based in the Beer's law which state that the intensity observed in an infrared band associated with the crystalline or amorphous component of the matrix, is proportional to the

Figure 3.5: Equipment used for DSC analysis. PerkinElmer DSC 8000.

product of concentrations of phases in the intrinsic intensity of the band [61]. In other words, the absorbency of light, intensity, in a semi crystalline structure is directly related with the concentration of the crystalline and amorphous components of the matrix. The results stated by the author mention that there are two sets of specific bands that can be used for tracking the percentage of phases in the polymeric matrix. The 1475-1420 cm^{-1} bands corresponding to a methylene scissoring mode [Fig. 3.8 (A)]. And, the 735 - 715 cm^{-1} that can be monitored with the methylene rocking bands [Fig. 3.8 (b)]. A slightly change in the intensity of those peaks indicate the variation in the crystallinity of the material. An interesting fact to consider is that the set of crystalline peaks previously explained are overlapped with the intensity absorbed by the amorphous content of the matrix. For this reason, Hagemann decided to perform their experiments in a control temperature chamber which allow them understand the IR absorbency of those peaks at different temperatures. By so doing, the crystalline peaks, noted in figure 3.8 as C, were mitigated. At this moment, only the amorphous content is visible in the FT-IR signal which can be used to satisfy the last variable in the equation 3.3. With this mathematical array, the researchers were capable of determining the degrees of crystallinity in the sample (χ_c^{FT-IR}).

$$\chi_c^{FT-IR} = \frac{I_C}{I_C + \alpha I_A} = \frac{I(722 + 730)}{I(722 + 730) + \alpha I(723)} \tag{3.3}$$

Where (I) is the observed intensities at a given band, crystalline (I_C) and amorphous (I_A), and (α) is the material coefficient related with the intrinsic absorption intensities in the amorphous component.

Since that our institutional facilities did not have a controlled temperature chamber mounted in the FT-IR equipment. For this research, the use of the FT-IR technique was entirely focused in identifying changes for the crystalline arrangements in a qualitative analysis by monitoring the intensities in the methylene rocking bands. Additionally, it was possible
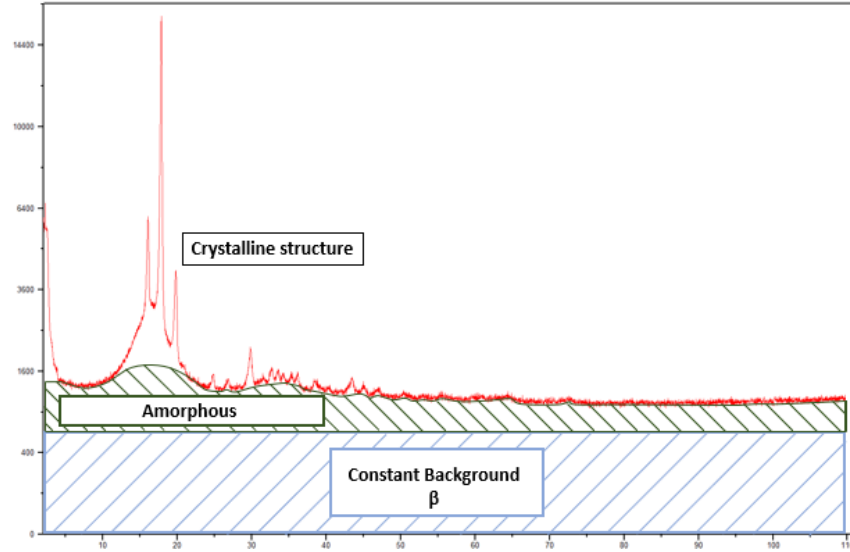
Figure 3.6: Schematic representation of the contributions found in a X-ray diffraction spectrum. For UHMWPE-TiO_2 nanocomposites: The crystalline structures correspond to the orthohombic and monoclinic crystal systems, the amorphous content to the disordered polymeric chains and the background is the measuring error produced due to the lost of diffracted X-rays.

to define a set of vibration bands that allowed the investigation to understand the interactions between the TiO_2 NPs and the UHMWPE matrix. The chemical interaction between the TiO_2 NPs and UHMWPE matrix was analyzed using FT-IR equipment (Perkin-Elmer Frontier Paragon 1000) with a UATR accessory [Fig. 3.9]. The procedure consisted of placing the developed sheet composites on the ZnSe-diamond crystal of the UATR and pressing with a tip to assure good contact between the sample and the incident IR beam. The IR spectra were measured in the interval range of 4000 cm^1 to 400 cm^1 with a resolution of 8 cm^1, and considering an average of 16 scans.

3.7   Tensile Tests Experimental Parameters

One batch of eight samples per concentration were arranged using the same methodology previously proposed for the preparation of the nanocomposite UHMWPE-TiO_2 sheet blanks, from which four of those samples per concentration were tested under a constant deformation uniaxial test. The samples were prepared by sectioning a portion of the complete UHMWPE-TiO_2 plates with a dog-bone shaped cutter [Fig. 3.10 (a)], obtaining detailed unharmed test samples [Fig. 3.10 (b)]. The new sectioned specimens were then mounted in a universal testing machine [Fig. 3.10 (c)] with no additional environmental external factors. Four principal mechanical properties were evaluated using the tensile universal machine to prove the reinforcement of the UHMWPE-TiO_2 composites: yield strength (Mpa), ultimate tensile strength (Mpa), young's modulus (Mpa) and the maximum elongation at break in (mm/mm). The
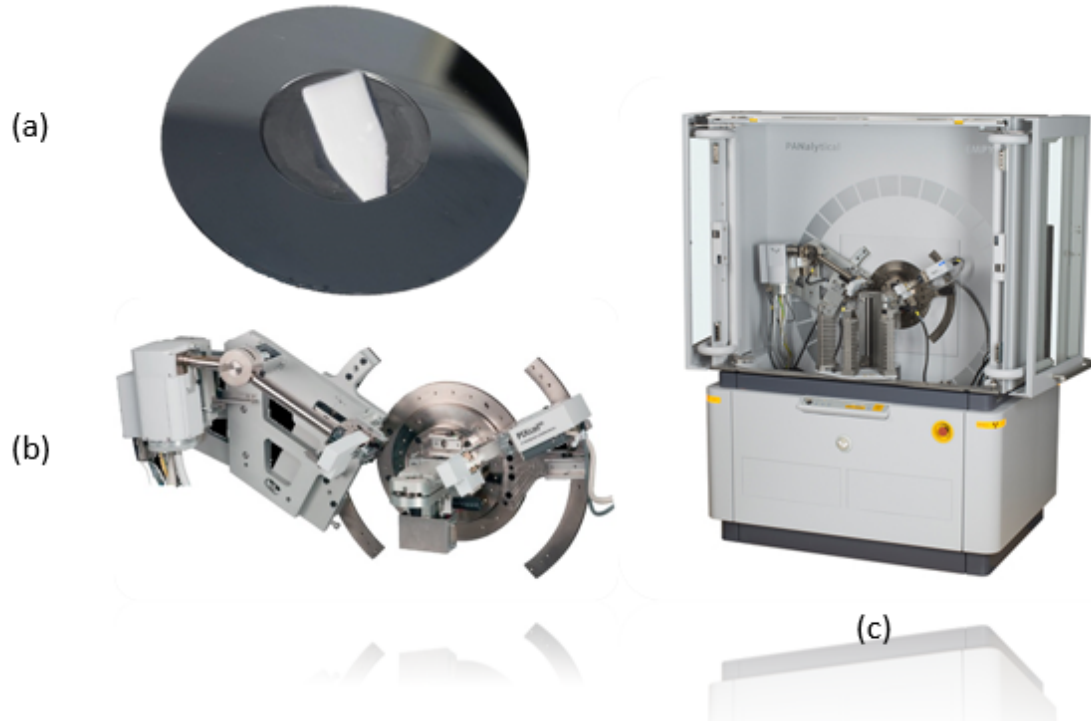
Figure 3.7: X-ray diffractometer configuration: (a) UHMWPE-TiO$_2$ specimen mounted in a zero background sample holder plate; (b) X-ray diffractometer sample stage; (c) PanAnalytical X'Pert Pro PW1800.

mechanical properties of the UHMWPE-TiO$_2$ composites were inspected through a repetitive analysis with a crosshead speed of 50 mm/min, based in the norm ASTM D638 - 14 for polymers type IV with dimensions of 33 x 6 x 2 mm [Fig. 3.10 (d)] [62].

3.8 SEM/EDX Experimental Parameters.

In our investigation, the arrangement of the samples and the analysis through the SEM-EDX technique were entirely aimed to identify agglomerations, discontinuities and chemical local compositions in the UHMWPE-TiO$_2$ composites. It was mandatory to cut a section of 15 x 10 x 2 mm of each concentration with the use of liquid nitrogen, assuring a clean and straight cut [Fig. 3.11 (a)]. Each fragment were then exposed to a coating process which involves a deep washing with isopropyl alcohol and a deposition of a thin film of gold in a rotary-pumped sputter coater (Q150R ES) [Fig. 3.11 (b)]. This process allow to improve the superficial conductivity of electrons of the UHMWPE-TiO$_2$ composites getting a better and more accurate propagation of the incident beams over the surface of the material leading to an improvement in image resolution. Then, the coated sections were mounted in a sample holder and placed inside the vacuum chamber [Fig. 3.11 (c)]. The analysis was employed in a ZEISS EVO MA 25 microscope [Fig. 3.11 (d)], with a spot size of 435, a voltage of 10 keV and a working distance of 7 mm. For the EDX spectroscopy a voltage of 20 keV was required,
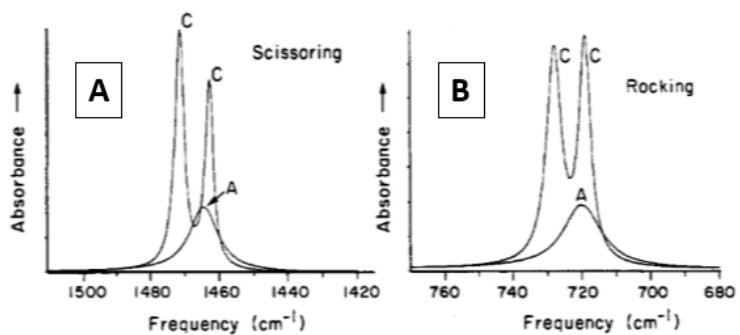
Figure 3.8: Methylene bands in polyethylene arrangements used for the calculation of crystallinity: (A) 1475-1420 cm^{-1}; (B) 735-715 cm^{-1}[61].

Figure 3.9: Equipment used for the vibrational bands found in the UHMWPE-TiO$_2$ nanocomposites. PerkinElmer Paragon 1000 FT-IR.

Figure 3.10: Tensile test arrangement: (a) Dog-bone sample cutter; (b) Representative batch of the dog-bone cut specimens based in ASTM D638; (c) Instron 336; (d) Representative sample result of the tensile tests per concentration.

higher intensities damaged the sample.

3.9 SPIF Experimental Parameters

For this experimental research the adequate SPIF parameters [Table 3.2], are based on the theoretical comparison in reference [44] and the resources available at the university. It was performed in a kryle VMC 535 vertical CNC milling machine [Fig. 3.12 (a)]. The setup of the mounting device consists of a fixed square base with a working area of 120 x 120 mm bolted to a Kistler 9257B dynamometer [Fig. 3.13]. A hemispherical D2 steel tool with 10 and 5 mm of diameter were used for the process [Fig. 3.12 (b)]. The selection behind the diameter of the tool is entirely focused on reducing as much as possible the friction over the surface of the material. The use of a smaller tool, also benefit the final detailed geometry of the desired prototype. In addition, since that the excessive amount of heat and friction can contribute to material failures. Cutting lubricant mineral oil (approx. 6 ml) was spilled over the polymeric sheet blank avoiding possible stresses and deformations caused by the high
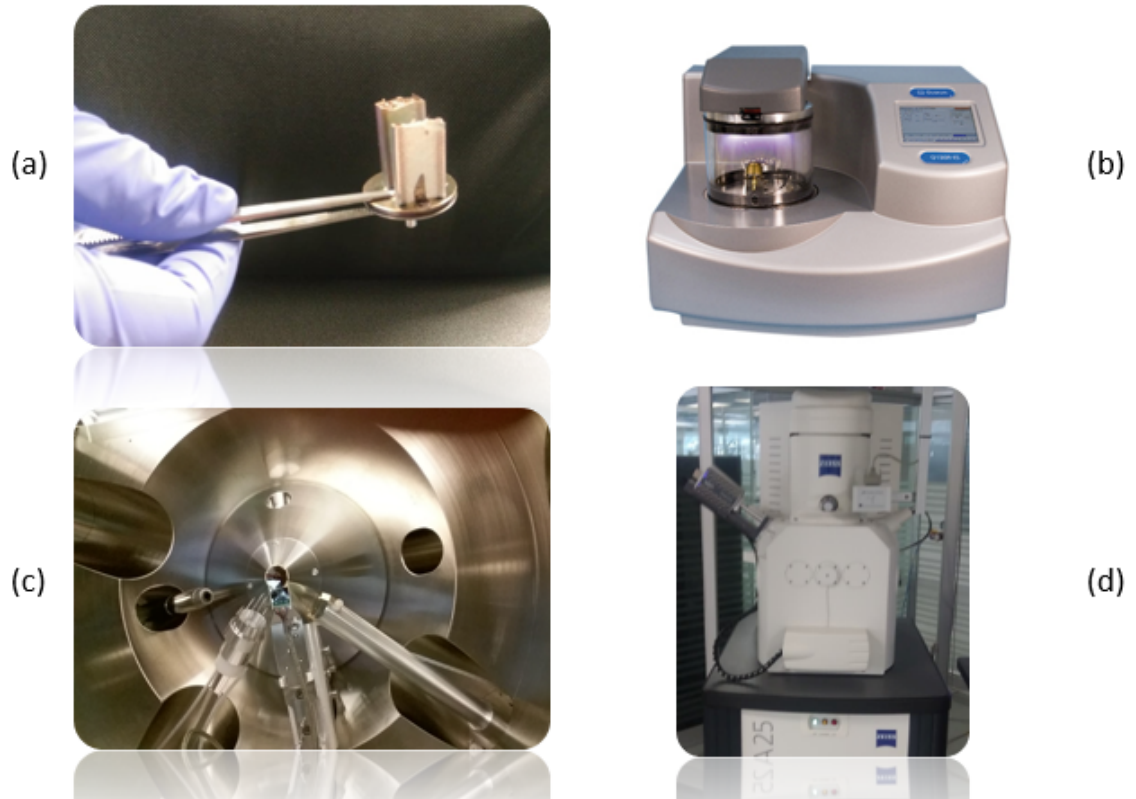
Figure 3.11: SEM-EDX arrangement: (a) Sample holder containing sectioned and coated specimens; (b) Q150R ES gold sputter coater; (c) Internal SEM chamber; (d) ZEISS EVO MA 25.

levels of temperature.

The path and geometry followed by the CNC machine are based in the model of an axi-symmetric part originated from the selection of an arc as a generatrix [Fig. 3.12 (c)]. The theory consulted for the selection of this geometry is described in [45] which allows to predict the wall thickness distribution along the depth of the working piece and the maximum elongation possible prior to failure. The initial diameter of the cone is 100 mm with an initial wall angle of 45°. According to the information gathered in [45] it is well know that the most aggressive approach to the sheet blank during the SPIF machining occurs at a wall angle of 90°, since the main goal of the research is to study the presence of nanoparticles inside the UHMWPE matrix by the forces opposing to the deformation prior to failing. The maximum depth was 40 and 28 mm with an exit wall angle of 78.05° and 69.07°, followed by a generatrix radius of 80 mm. An example of the CNC code used for the axi-symmetric part is written in appendix C.1 and it was modified according to the parameters needed for each test run.

Finally, the data retrieval consisted on the identification of the forces in z axis (f_z), y axis (f_y) and x axis (f_x). These forces were measured using a kistler piezoelectric dynamometer and a voltage amplifier previously tested [64]. In other words, the forces applied in any direction on the surface of the material are distributed among the blank holder. As a consequence of the deformation sensed by the piezoelectric dynamometer, bolted to the blank holder, a small pulse is then released and transmitted directly to the amplifier. The amplified signal
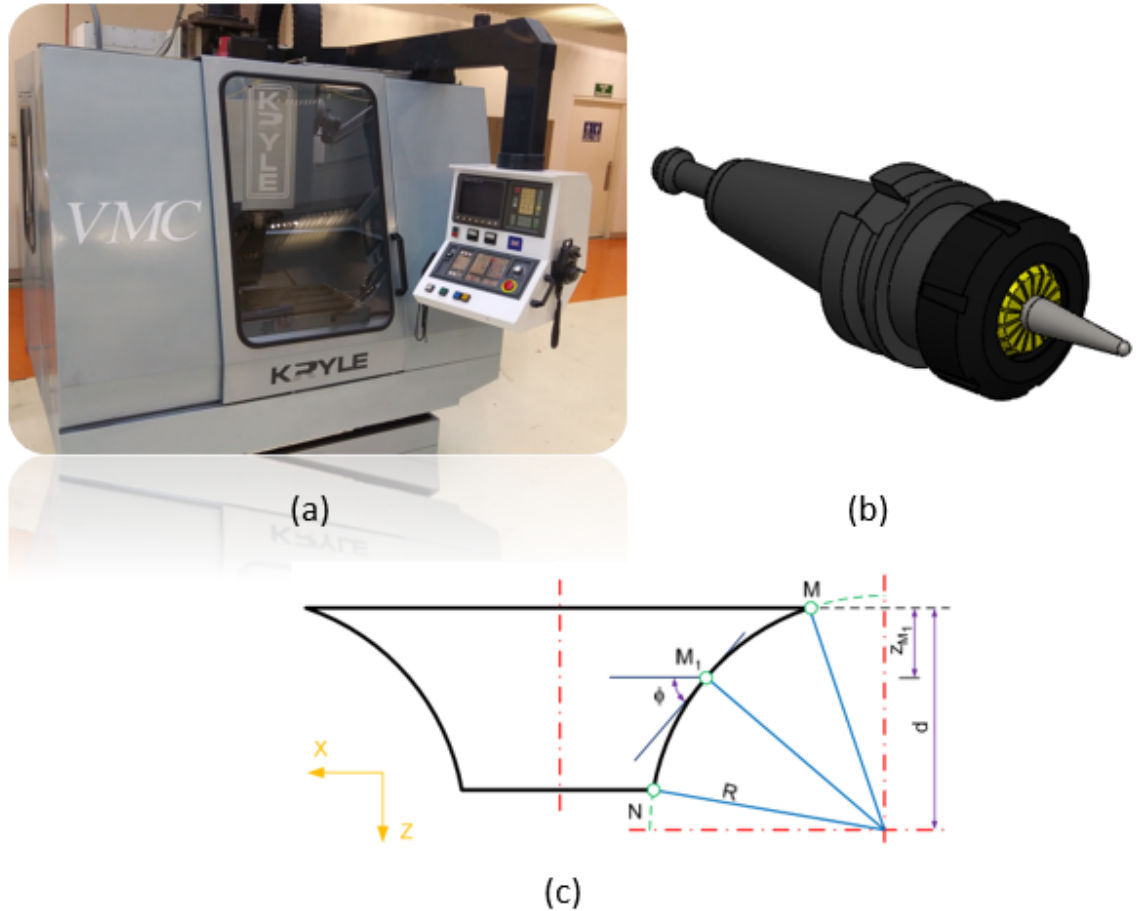
Figure 3.12: Single point incremental forming: (a) Kryle VMC 535 vertical CNC milling machine; (b) Hemispherical D2 steel tool; (c) Axi-symmetric SPIF geometry [63].

corresponding to an exact force applied in an exact time is storage in a USB data acquisition card where it is processed in real time with help of a software called "Matlab Simulink". The voltage signal is then translated into units of force known as Newtons. After the test run is finish, the registry of the forces applied to the material in all directions are exported in an "XLS" file. Since that the measurements coming directly from the tests are full of noisy data, a new Matlab code was written in order to smooth and report the results. Code shown in appendix A.1.

3.10   Roughness Experimental Parameters.

The methodology followed in the study of the roughness for the UHMWPE-TiO$_2$ composites involve a partial sectioning of the axi-symetric parts made by SPIF for each concentration [Fig. 3.14 (a)] were a bidirectional, longitudinal and circumferential analysis was performed. The longitudinal measurement cover the study of the macro sharp edges formed by the stepdown
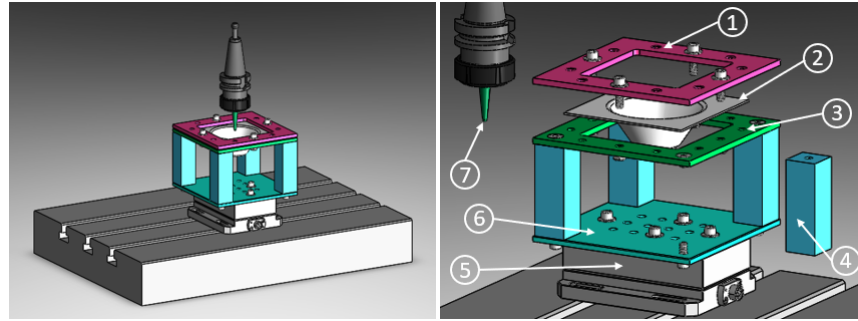
Figure 3.13: CNC milling machine set up for single point incremental forming process; (1) Top plate; (2) Sheet blank; (3) Clamping plate; (4) Hollow support; (5) Dynamometer; (6) Bottom plate; (7) Forming tool.

Table 3.2: Optimized parameters used during the conforming process by SPIF.

Parameters	SPIF	Generatrix Tool Path
Spindle speed	0 rpm	$\cdots$
Tool diameter	5 mm and 10 mm	$\cdots$
Feed rate	300 mm/min	$\cdots$
Vertical step down (Δz)	0.25 mm and 0.5 mm	$\cdots$
Initial diameter	$\cdots$	100 mm
Generatrix radius	$\cdots$	80 mm
Initial angle	$\cdots$	45°
Exit angle	$\cdots$	69.0° and 78.0°
Maximum depth	$\cdots$	28 mm and 40 mm

movement (Z axis) of the tool path. While the circumferential test run is a consequence of the feed rate or friction of the tool against the deformation over the sheet blank in X and Y axis. Both tests aimed for defining the average roughness of the surface (Ra) and the ten point mean roughness (Rz) of each concentration. Looking for a correlation between the roughness indicators and the promising cell proliferation results. A Mitutoyo SJ-210 profilometer was used to avoid as much as possible the measuring uncertainty [Fig. 3.14 (b)]. Lastly, a reference sample without the post manufacturing process of each concentration were submitted to the same run tests. Due to the nature of the results, the explanation and summering data are written and explained in Appendix B.3.

Figure 3.14: Roughness testing: (a) Partial section taken from UHMWPE-TiO$_2$ composites processed by SPIF for roughness analysis; (b) Mitutoyo SJ-210 profilometer equipment used for the study of superficial roughness.

Chapter 4

Results and discussion.

4.1 Characterization Discussion.

In the next chapter, a well explained discussion of the results are described with an interesting approach of correlating three different studies (DSC, XRD and FT-IR) in a single crystallization phenomena. It is important to reestablish that the results presented in this chapter are completely oriented to the understanding of the internal structural interaction of TiO_2 embedded in an UHMWPE matrix. Focusing in the improvement of the mechanical properties of the material while adding unique characteristics. Starting from this statement, two partial hypothesis where suspected beyond the addition of TiO_2 nanoparticles [Fig. 4.1]. The first one is related with the idea previously discussed by Grady et al. (2002), from where it was established that the interaction of nanofillers inside polymeric matrices must act as a centered nucleus for attraction of carbon chains [65]. In a more recent publication, the interaction of functionalized carbon nanotubes in UHMWPE propitiated the increment in degrees of crystallinity in almost 22% compared with its pure batch [58]. On the other hand, the second hypothesis believed that the nanoparticles were so big, macro scale, that they would inhibit the growth of polyethylene chains around the nanoparticles. Leading to a loss of semi-crystals and a reduction in the mechanical properties of the composite.

Hypothesis #1   Hypothesis #2
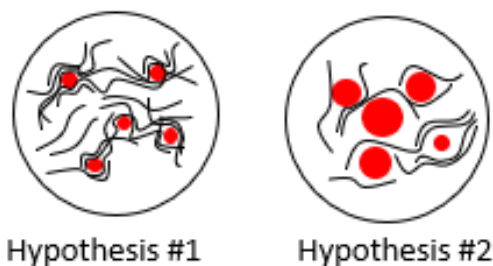
Figure 4.1: Crystallization of the UHMWPE-TiO_2 composite: Hypothesis #1 TiO_2 NPs act as a nucleation focus point for polyethylene chains; Hypothesis #2 TiO_2 NPs are big enough to inhibit the natural order of semi-crystals.
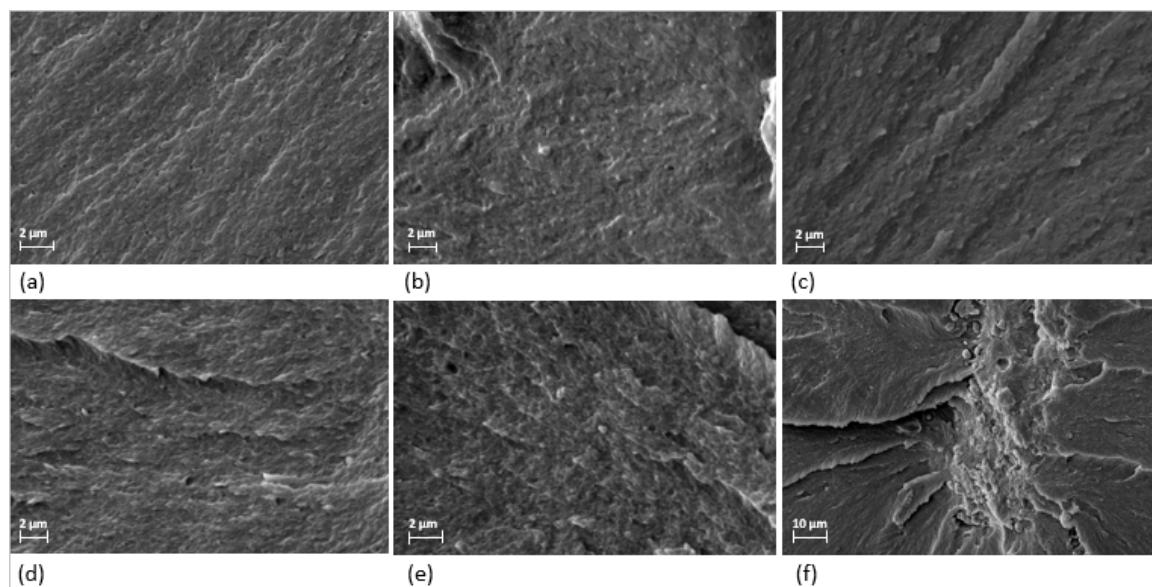
Figure 4.2: SEM images of the cross-sectional area for UHMWPE samples: (a) Reference (0%); (b) M1 (0.25%); (c) M2 (0.5%); (d) M3 (0.75%); (e-f) M4 (1%). Homogeneous dispersion of NPs are found at low concentrations ($\leq$0.75 wt.%) with considerable clusters after 1 wt. %. No phase separations were found.

The first approach to validate one of the previously mentioned hypothesis is to characterize the surface of the material through the use of SEM [Fig. 4.2]. Despite the small agglomerations observed in samples M1, M2, and M3, the TiO_2 NPs dispersion was satisfactory. The presence of such agglomerations is due to the difficulty of deagglomerating some TiO_2 NPs clusters during the incipient wetting process. As it is reported by Panaitescu et al. in Ref. [20] for polymers composed by single carbon chains (PE and LDPE) the saturation level for TiO_2 NPs occurs above five wt %. However, the results in this work show an increment considerable of agglomeration in sample M4 [Fig. 4.2 (e) and (f)], which suggest that for those polymers composed by long carbon-hydrogen chains (UHMWPE) the saturation level occurs above one wt %.

Table 4.1: Onset melting temperature (T_m^{onset}), enthalpy of fusion (ΔH_m) and degree of crystallinity (χ_c^{dsc},χ_c^{xrd}) retrieved from DSC and XRD.

Sample	$T_m^{onset}(^{\circ}C)$	ΔH_m (J g^{-1})	$\chi_c^{dsc}(\%)$	$\chi_c^{xrd}(\%)$
Reference	126.0	91.0	31.5	31.9
M1	125.6	94.8	32.8	31.1
M2	125.7	92.8	32.3	30.4
M3	125.9	92.6	32.3	31.9
M4	125.9	88.6	30.9	29.2
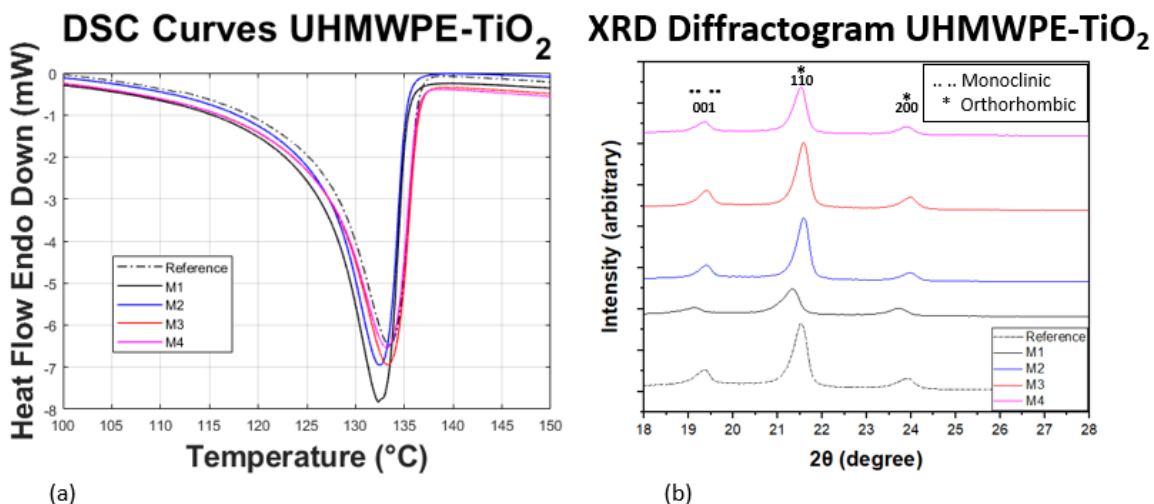
Figure 4.3: (a) DSC Thermograms and (b) XRD diffractogram of the UHMWPE sample (Reference) and sheet composites (M1-M4). The DOC behave partially constant through the addition of TiO_2 but, with the formation of a monoclinic crystal phase as a consequence of the compression molding process.

Once the superficial arrangement of particles is studied, the use of a DSC and XRD analysis are essential for understanding the crystallization phenomena occurring in the UHMWPE-TiO_2 composites. The endotherms for all the samples (Reference sample and M1-M4 composites) [Fig. 4.3 (a)] show similar behaviors, exhibiting a well-defined lineshape between 110°C - 138°C with an onset temperature for melting around 125°C. The relative increment of amplitude for M1 and M3 indicates that the TiO_2 NPs contribute to the crystallization process in the composites, but not with a high intensity to modify the degrees of crystallinity in a considerable magnitude [Table 4.1].

As mentioned in chapter 3 a complementary analysis of XRD was conducted, focusing directly in comparing if the phases in the diffractograms for all the samples (Reference sample and M1-M4 composites) [Fig. 4.3 (b)] matched the crystallinity results calculated by DSC. After taking several measurements, it was possible to statistically validate that with a 95% confidence that there is not enough evidence to reject the parity in the degrees of crystallinity within the UHMWPE-TiO_2 composites, and between the data extracted from DSC [Table 4.1]. However, the data obtained from the XRD showed a slight shift and two peaks at 21.5° and 23.9°, which corresponds to (110) and (200) plane of an orthorhombic unit cell [66], and a new peak at 19.4° corresponding to (001) plane of a monoclinic unit cell [66]. The presence of a well-defined plane (001) at 19.4° suggests that a stress component, induced during the hot-pressing manufacturing process, reduces a fraction of the symmetry from orthorhombic to monoclinic.

Using FT-IR as an analytic method for defining the interaction between both components of the UHMWPE-TiO_2 composite [Fig. 4.4]. It was possible to characterize that the position of infra-red absorption vibrational bands has no change with the addition of TiO_2 NPs. The modes detected for UHMWPE reference sample (Reference) show peaks at 2924 cm^{-1} and 2851 cm^{-1}, which correspond to the asymmetric and symmetric stretching mode of
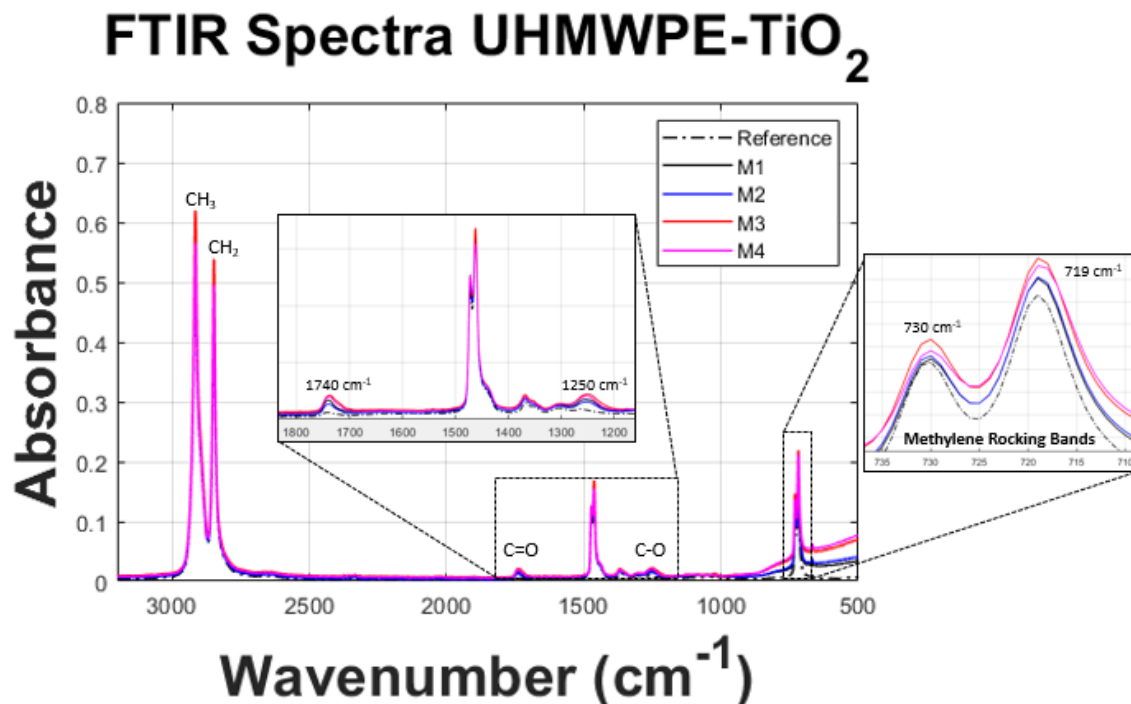
Figure 4.4: FT-IR spectra of the UHMWPE (Reference) and UHMWPE-TiO$_2$ sheet composites (M1-M4). An interaction of TiO$_2$ NPs with the polymeric chains are observable in bands 1740cm^{-1} (C=O) and 1250 cm^{-1} (C-O).

C-H, respectively [67]. The mode at 1469 cm^{-1} is related to the in-plane bending vibration of C-H, and the modes at 730 cm^{-1} and 719 cm^{-1} correspond to methylene rocking vibrations, which are attributed to the high degree of polymerization and long molecular chains of UHMWPE [67]. However, the incorporation of the TiO$_2$ NPs in the UHMWPE polymeric matrix (M1-M4 composites) promotes carbon-oxygen interactions as it was detected in the modes at 1740 cm^{-1} (C=O) and 1250 cm^{-1} (C-O). The detection of such modes indicates that the TiO$_2$ NPs have been dispersed homogeneously and their presence can be explained by the photocatalytic activity of TiO$_2$ [17]. Additionally, as a result of the incorporation of TiO$_2$ in different concentrations, the methylene rocking modes at 730 cm^{-1} and 719 cm^{-1} show an increment of amplitude which is associated to a crystallization process in the composite matrices [61]. Adding up, the carbon oxygen interaction indicates that the TiO$_2$ NPs are covered by polymeric chains. This is confirmed by the SEM-EDS image, Figure 4.5, that shows the presence of an amorphous layer of the polymer material that covers the TiO$_2$ NPs surface [68, 57].

Further studies (traction test and SPIF) related with the mechanical behavior of the composite were evaluated, focusing entirely in the performance of the UHMWPE matrix prior and post the dispersion of TiO$_2$ NPs. The results of the traction test [Fig. 4.6 and Table 4.2] illustrate that the use of TiO$_2$ nanoparticles does not have a clear impact in the elastic region of the polymeric matrices. All of the tested samples behave barely constant. The yield strength
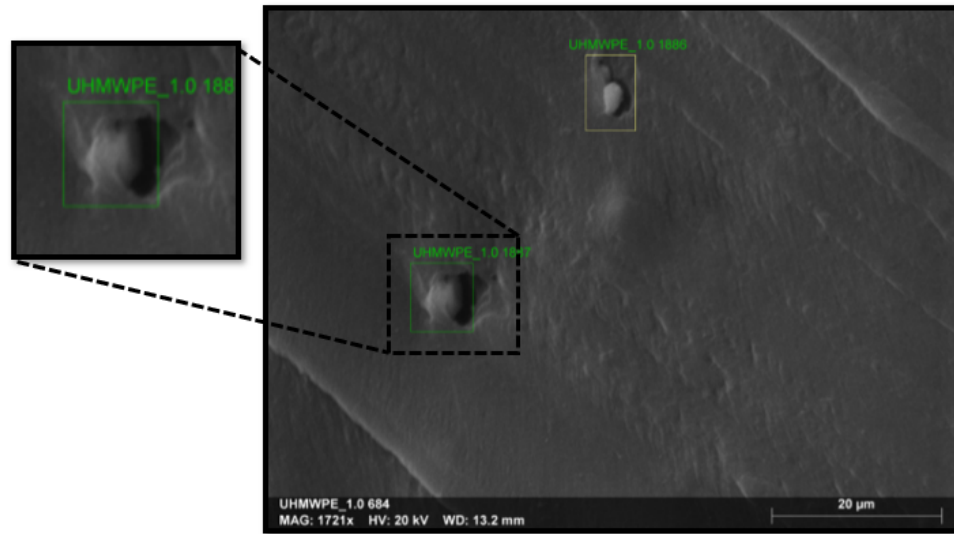
Figure 4.5: Energy dispersive X-Ray spectroscopy (EDS) micrograph that shows agglomerated TiO_2 nanoparticles covered with UHMWPE

and the elastic modulus does not have a considerable change, which rely on similar stiffness and resilience properties. It is marked a small deviation in the Young's modulus of the M2 (UHMWPE-TiO_2 at 0.5%) sample with a minor tendency of increment accordant to the growth in titanium (IV) concentration.

Table 4.2: Stress-Strain curve results of the UHMWPE sample (Reference) and sheet composites (M1-M4). M3 exerting the best mechanical performance from all the samples.

Sample	Average Yield strength (MPa)	Average Ultimate Tensile Strength (MPa)	Average Young's modulus (MPa)	Average Maximum strain (mm/mm)
Reference	15.1 ± 0.76	23.4 ± 0.53	450.5 ± 32.04	0.83 ± 0.05
M1	15.6 ± 0.83	24.7 ± 0.48	455.5 ± 14.0	0.84 ± 0.06
M2	15.9 ± 0.47	27.8 ± 2.23	476.0 ± 32.27	0.93 ± 0.042
M3	16.4 ± 0.14	30.4 ± 1.79	501.7 ± 16.71	0.91 ± 0.03
M4	16.6 ± 1.18	27.8 ± 1.48	509.3 ± 16.97	0.89 ± 0.095

Nevertheless, the plastic region exerts a small but defined increment in the ultimate tensile strength and maximum elongation possible prior to failure. The ductility granted for the sample M3 (UHMWPE-TiO_2 at 0.75%) distinguishes in relation with its pure batch and the rest of the specimens, considering the fact that the increment of strain raised almost 10% with an ultimate tensile strength reaching up to 30% of improvement. The mechanical properties observed in the nanocomposite sheet samples suggest that the maximum TiO_2 concentration allowed in UHMWPE is 0.75 wt. % (M3). This result is consistent with the cross-sectional SEM images [Fig. 4.2], detecting an increment of NPs agglomerations for sample M4. It is important to note out that the best mechanical properties achieved in this research reach the most recent UHMWPE-TiO_2 nanocomposite publication, proposed by G. Celebi et al. but, with the use of lower concentrations of TiO_2 NPs [69].
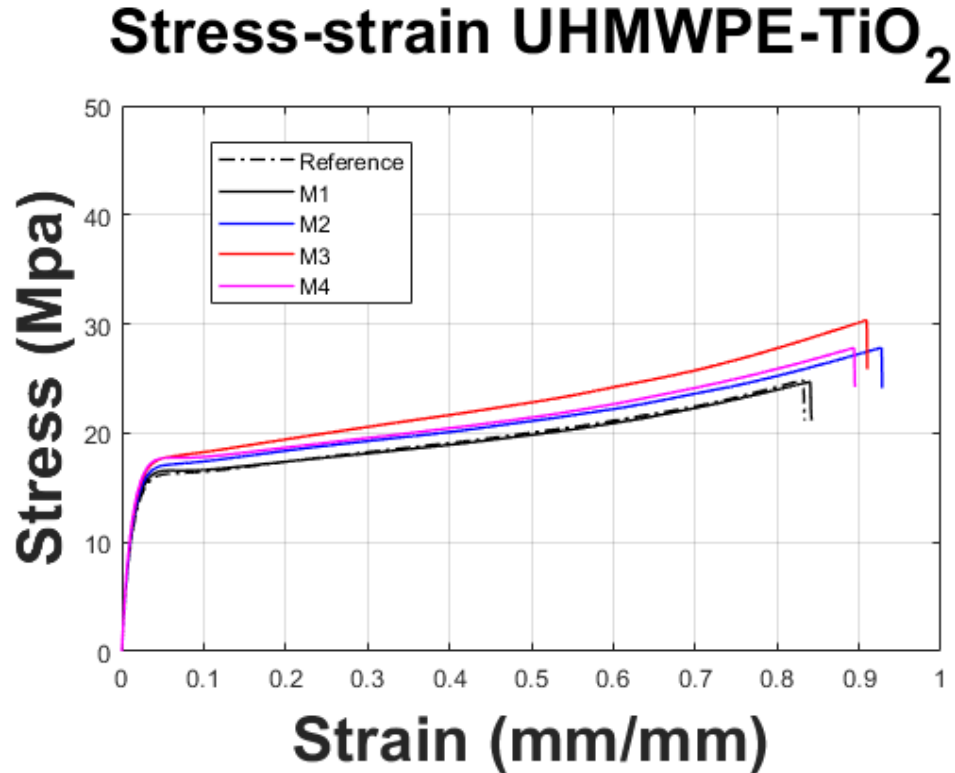
Figure 4.6: Stress-strain curves of UHMWPE-TiO$_2$ nanocomposites. Mechanical properties increased with the addition of TiO$_2$ NPs until saturation point. For M3 sample, a 30% increase in UTS was achieved in addition to a 10% of maximum strain before failure.

The SPIF manufacturing process was carried out considering two different tool diameters, 5 mm and 10 mm, allowing to have partial control in the deformation behavior of the UHMWPE-TiO$_2$ sheet composites. In concordance to the previous traction analysis, the maximum forces acting against the deformation of the polymer plate during SPIF manufacture [Fig. 4.7] exhibit a similar behavior than the obtained by the tensile strength tests. Therefore a constant growth in opposing forces is enhanced in sample M3 (UHMWPE-TiO$_2$ at 0.75%) reaching a maximum force [F_z^{10mm}] of 688.0 Newtons subsequent to a decay in mechanical properties and forces at higher concentrations. This behavior reconfirms that the highest saturation level of TiO$_2$ NPs inside the UHMWPE-TiO$_2$ composite is 0.75 wt. %. A strong relation between the diameter of the tool and increment of the wall-stress acting against the deformation is observable [Table 4.3 and Table 4.4]. This occurs since that a smaller hemispherical tool act as punctual force, increasing the pressure applied over the wall [44].

Summing up from the characterization results explained in this section, it was possible to refute both of the previously stated hypothesis. In fact, the interaction of TiO$_2$ NPs with the long active chains of carbon in the polymeric matrix propitiate the creation of non stable energy links. Since the changes in the degrees of crystallinity are almost null, and a new crystalline plane was observed in the XRD analysis. A third hypothesis was established stating that the TiO$_2$ in addition with a compression molding manufacturing process, do not have the sufficient energy capable of promoting the creation of robust and reliable lamellae. In simple

Table 4.3: Maximum forces measured during SPIF with a tool of 10 mm. The opposing forces F_z^{10mm} increases with the same tendency of reinforcement as the tensile test results previously reported with a sink after 1 wt. %.

Sample	F_x (N)	F_y (N)	F_z (N)
Reference	407.67	389.64	577.66
M1	417.87	406.26	597.01
M2	407.67	405.68	602.38
M3	448.44	442.37	688.00
M4	401.58	399.52	595.33

Table 4.4: Maximum forces measured during SPIF with a tool of 5 mm. The opposing forces behave barely constant but, with a stronger reinforcement after the addition of TiO_2

Sample	F_x (N)	F_y (N)	F_z (N)
Reference	181.39	175.30	299.59
M1	199.76	199.79	360.74
M2	195.63	191.61	345.42
M3	191.64	201.77	348.47
M4	199.70	197.69	351.52
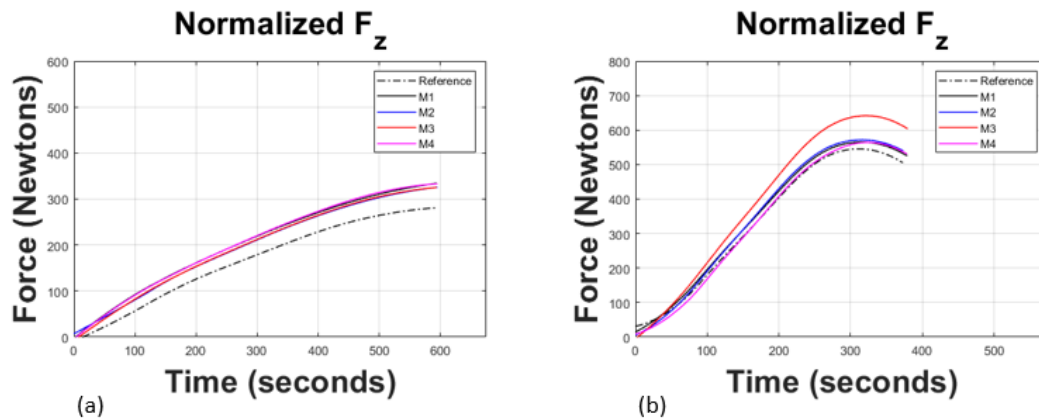
Figure 4.7: Normalized forces in Z-axis acting over the surface of the nanocomposite plate during SPIF: (a) with a tool diameter of 5 mm; (b) with a tool diameter of 10 mm. The results support the reinforcement of the nanocomposite bellow 0.75 wt. % with a considerable sink due to the presence of clusters at higher concentration.

terms, small network bridges of physical attraction between lamellae were formed allowing a beneficial stress distribution of the internal and external forces exerted into the material without compromising the total degrees of crystallinity of the composite. A visual approach illustrating the stability of crystals measured through both methods against the mechanical response of the composite is postulated [Fig. 4.8].
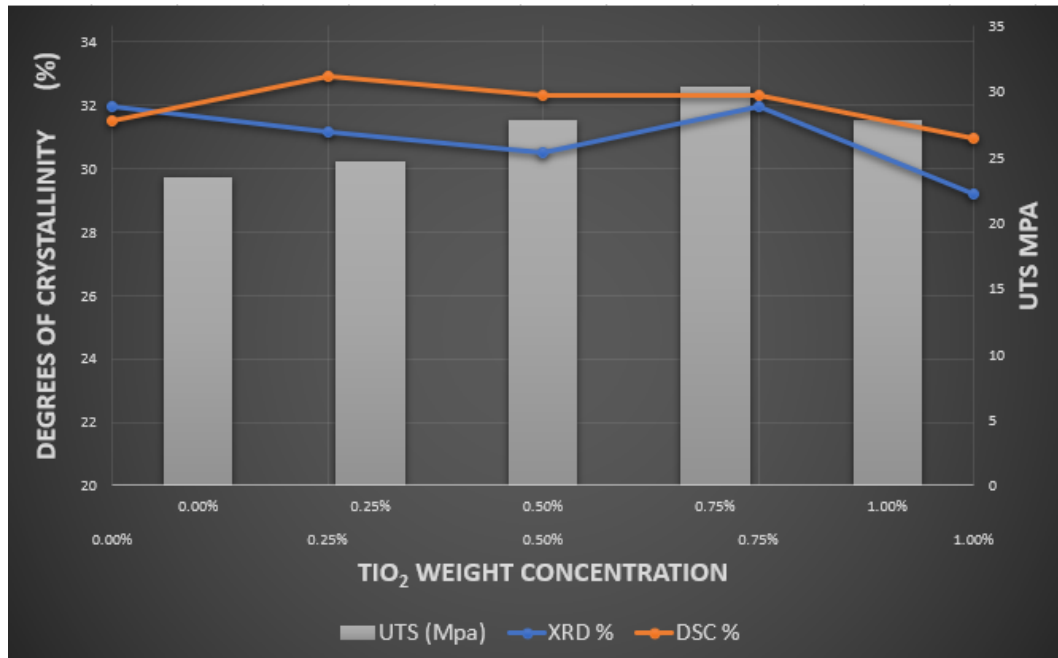
Figure 4.8: Comparison of the composite degrees of crytallinity against the ultimate tensile strength per concentration. The mechanical properties are related with the presence of TiO_2 NPs and not strictly with the DOC found in the samples.

As explained before, having irregular shapes in the prosthesis as well as an inadequate material's morphology or even a late intervention, could originate to physiological problems in the post-surgical recovery of many patients. The following entirely sections are aimed primary in the development of a real prototype capable of satisfying the specific geometrical and biological needs requested by the patients' facial trauma. An overview of the designing and manufacturing procedures are described. Followed by the analysis of the geometrical errors produced in the final shape of the implant after SPIF procedures, via a 3D scanning system. Finally, a cell imaging kit was used in order to test the cytotoxicity response of human cells against the surface of the composite matrix.

4.2 Prototype Design and Manufacture.

The patient's face dimensions, obtained from a technique known as section scanning imaging, were used to avoid geometric defects in the manufacturing process.This medical instrument take an infinite number of 2D human body images which are then stacked together in a single 3D model [Fig. 4.9 (b)]. This model can not be modified or adjusted to design the prosthesis by its own but, it can function as a reference for measuring the magnitude of the damaged

tissue and the missing geometrical bone space. Once the boundaries of the affected tissue are fully defined, the use of a computer-aided design software (CAD) comes into place.

CAD is explained as tool capable of substituting the design made by hand with an automatized deploy of controlled vectors, surfaces, solids and assemblies that can be modify, share, storage, visualize and measure at any time. This technologies allow the designers to create from scrap, 3D/2D complex geometries, in a fast and precise protocol. From the variety of CAD software, the use of Solidworks 2018 was applied to perform the design of the facial prosthesis. The drawing coordinates and parameters were taken from the tomography of the patient, giving as a result a detailed and personalized graft [Fig. 4.9 (d)]. When the complexity of the designs overcomes the capacity of the manual manufacturing means, it is requested to appeal the use of a computer aided manufacturing processes (CAM). The application of CAM is directly encourage in the creation of detailed instructions that will control the actions of CNC machinery, without the intervention of human interaction. The instructions, normally known as G codes, define a tool path based in the geometry designed in Solidworks. The tool path of the prosthesis [Fig. 4.9 (a)], was developed in Simens NX 9 manufacturing environment with the same parameters applied in the SPIF characterization process for a 5 mm tool diameter [Table 3.2].

(a)　(b)

(c)　(d)
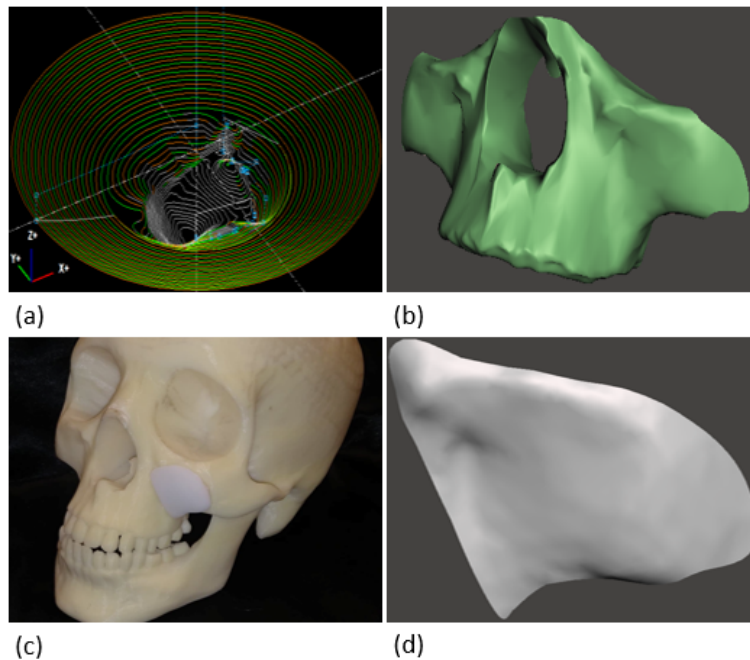
Figure 4.9: Facial prosthesis design. (a) SPIF tool path; (b) Patient tomography; (c) Real manufactured facial prosthesis; (d) CAD sectioned facial graft.

Since that the best mechanical, biological and thermal properties were obtained with a concentration of 0.75 wt %. The final prototype [Fig. 4.9 (c)] was perfectly manufactured and mounted in a skull model with the same geometrical space as the patient's skull and according to the previously mentioned concentration.

4.3 Nanocomposite Plate Formability.

Formability is expressed as the ability of any material to go through plastic deformations without suffering permanent damage [70]. This characteristic rely mainly in the mechanical properties of the material and the parameters used in the post manufacturing deformation procedures. It is important to consider that every time a material is forced to be plastic misshaped, an opposing force is acting against the deformation. This contradictory forces, commonly know as spring back or material recovery, are key concepts that will predict the final shape of the geometry and the maximum formability of the material. For our intended purpose and in order to avoid as much as possible the error between the designed graft's shape and the final prototype affected with the material recovery. A 3D hand held scanning system, Creaform EXAscan [Fig. 4.10 (a)], was used to recreate a virtual mesh image of the manufactured part. Once the virtual mesh was created, a calculation of the shape distance (Δd) existing from the intended designed surface in comparison with the real manufactured sample, was made using GOM Inspect software [Fig. 4.10 (b)]. The results per concentrations are reported in table 4.5, appendix Fig. D.1 and appendix Fig. D.2.
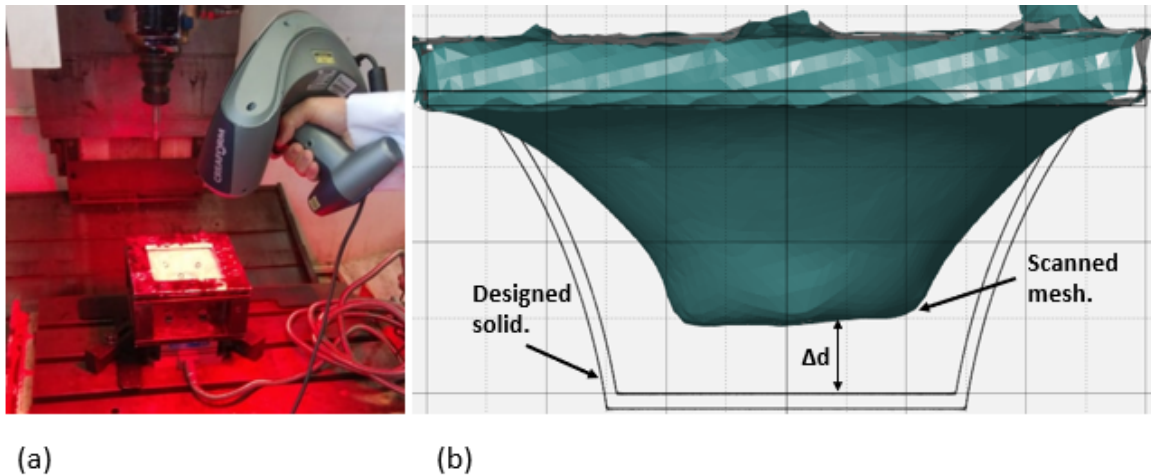
Figure 4.10: Polymeric plate formability: (a) Creaform EXAscan; (b) Overlaying of the scanned mesh with the designed solid in GOM Inspect.

From the recollected data, it is possible to conclude that the geometrical error is not strictly related with the presence of the NPs inside the polymeric matrix. As proved before, there is a reinforcement of the UHMWPE-TiO$_2$ composites but, it does not benefit the formability of the final sample geometries. In fact, the small increase in the mechanical properties reported in chapter 4 contribute to the spring back forces opposing to the deformation of the material. Also, it must be emphasize that the geometrical errors are more sensible to changes in the manufacturing parameters than to the concentration of the dopants inside the polymeric matrix [44]. As proved by Duflou J.R. et al. [71] and Palumbo G. et al. [72] the use of localized heating environments allow to reduce the spring back recovery of the material enhancing the formability of the final piece. Further studies must be made with the modification of SPIF trajectories and the inclusion of external heating factors that will allow the UHMWPE-TiO$_2$ nanocomposite to have less geometrical errors. Finally, the test runs with a smaller step down,

reduced tool diameter and almost half the working depth, illustrated a considerable reduction in the geometrical error in comparison with the analysis made for a 10 mm diameter. This was originated due to the capacity of the tool to reach small spots that can not be deformed with the use of a high diameter tool tips.

Table 4.5: Geometrical error results per TiO_2 concentration and tool diameter. The geometrical error is not affected by the presence of TiO_2, it is more sensitive to the manufacturing parameters used during SPIF.

Sample	Maximum depth 10 mm / 5 mm	Average distance from CAD (Δd) 10 mm / 5 mm
CAD Reference	40 – 28	—
Reference	30.81 – 24.57	9.69 – 4.91
M1	31.15 – 23.65	9.53 – 5.24
M2	31.21 – 23.82	9.55 – 5.20
M3	30.9 – 23.52	10.05 – 5.02
M4	31.05 – 23.47	9.56 – 5.38

4.4 Nanocomposite Cell Cytotoxicity.

Cells were seeded at $1x10^4$ cells/well and incubated at 37°C. After 4 h post-seeding, non-adherent cells were removed with a PBS wash, the remaining cells were detached with 0.25% trypsin/EDTA and the cell number was quantified according to the trypan blue exclusion assay. In addition, the results, expressed as a percentage of the original seeded cells, were also compared with a tissue culture treated plate. To study cell proliferation, cells were seeded in a 96 well plate at a density of $1x10^4$ cells per well ($3.12x10^4$ cells/cm^2). Cell viability was evaluated after 24, 48, and 72 h post-seeding using CellTiter96 AQueous one solution cell proliferation assay. Then, 20 μL of CellTiter96 were added to each well and incubated at 37°C for 1 h, the supernatants were transferred to a new 96-well plate. The absorbance was acquired at 490 nm (Synergy HT, BioTec, Winooski, Vermont, USA). Each nanocomposite was compared against a tissue culture treated well (control) and the results were expressed as a percentage. The biological feasibility of the sheet composites was investigated by studying cell adhesion and cell growth and the results are shown in Figure 4.12. The percentage of adherent cells on the composite material samples was lower than the control well plate. Notice that the UHMWPE is able to support the cell attachment without any treatment due their biocompatibility properties. It is also observed in Figure 4.12, that the addition of up to 1 wt % of TiO_2 has no statistically variations against UHMWPE however, it has been reported that the use of higher TiO_2 concentrations can increase the hydrophobicity and therefore, improve cell behavior [73]. Furthermore, the results of cell viability through time, Figure 4.12 b, indicates that all the produced samples do not have deleterious effects on cell growth. At the beginning of the assay, the cell viability of samples was among 88-95% compared with the control; after 72 hours, the sample M3, with 0.75 wt % of TiO_2, presented the highest viability value (109%). This show that the addition of TiO_2 to the polymeric matrix influences cells growth.

The cell attachment was also observed by fluorescence microscopy (Figure 4.11). After 72 hours post-seeding, cells were associated with a favorable growth due to the high confluence and uncompromised state (green color) and the almost null propidium iodine infiltration in treatments (red color). Moreover, the cells presented a normal elongated phenotype.
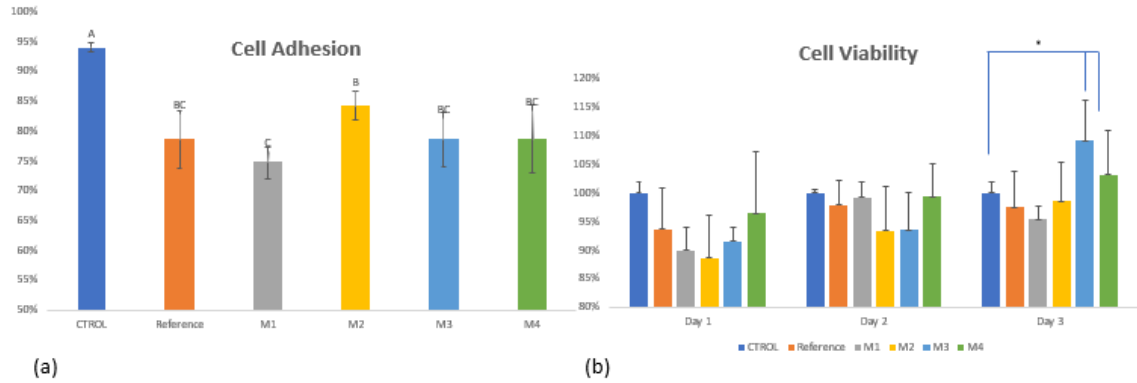
Figure 4.11: Biological feasibility of UHMWPE-TiO$_2$ composites: (a) Cell Adhesion after 4 hours post seeding; (b) Cell viability on the surface of UHMWPE-TiO$_2$ composites after 72 hours. Appropriate adhesion of cells were observed after post seeding with a favorable environment for cells growth.
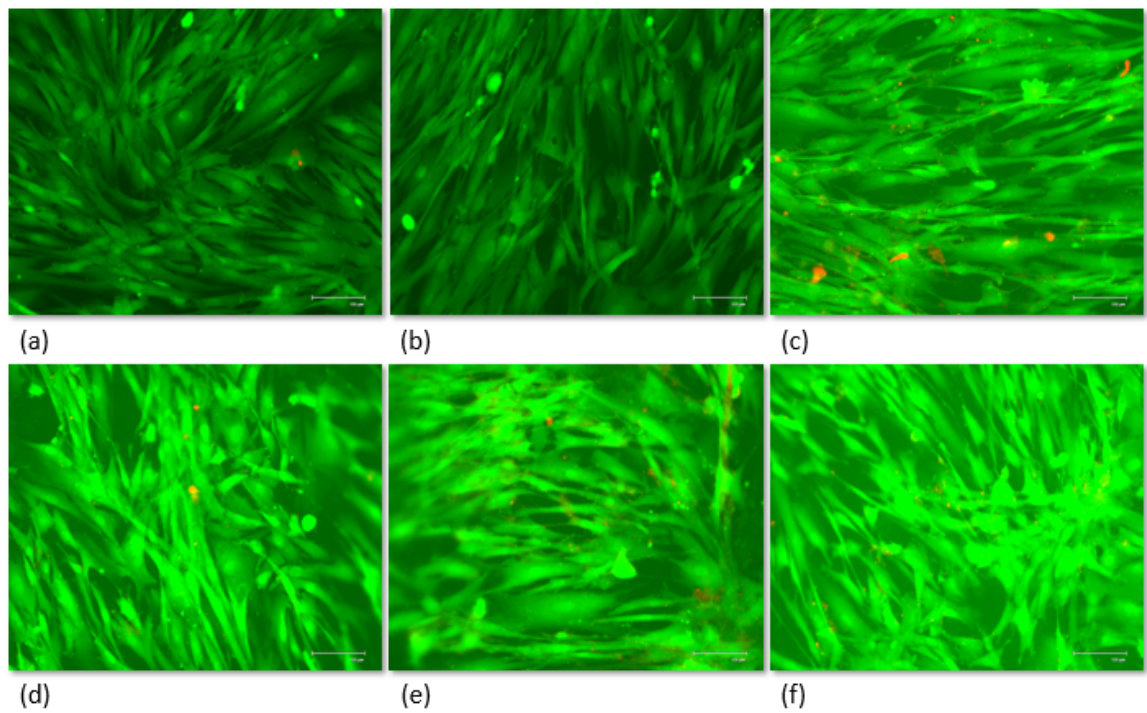
Figure 4.12: Fluorescence microscope images of human fibroblast cell growth on the surface of UHMWPE composites after 72 hours: (a) Control sample; (b) Reference (0%); (c) M1 (0.25%); (d) M2 (0.5%); (e) M3 (0.75%); (f) M4 (1%). Almost null cytotoxicity is reported.

Chapter 5

Conclusions.

Nanotechnology applied to materials science in biomedic environments is a trending topic. It involves the development of nanocomposites capable of combining two or more opposing characteristics in useful prototypes, which exerts the recent understandings of medicine. The zygomatic partial trauma, as it has been establish in this thesis, is a problematic that it is causing physiological, social and emotional irreversible pathologies among the modern society. For this reason the study of new technologies such as nanomaterials are of extreme importance to develop advanced composites with authentic mechanical, chemical and biological characteristics suitable for fitting the basic properties of the zygomatic bone. In this thesis, UHMWPE-TiO$_2$ sheet composites were prepared using incipient wetting and compression molding processes. Positive results were obtained through the dispersion of the NPs in a liquid solution observed at low concentrations (<0.75 wt. %) with a particular visual sink after 1 wt. %. This phenomena was confirmed with the use of SEM images which illustrated massive agglomerations of NPs in the order of micrometers. The hot/cold-pressing manufacturing procedure (compression molding) presumes to inhibit the normal crystallization phenomena of the carbon chains in the UHMWPE-TiO$_2$ nanocomposites. After doing a correlation between the results visualized with DSC and the XRD spectra it was possible to observe the reduction of symmetry in the orthorhombic unit cells, found in (110) and (200), to monoclinic structures (001). **This implies that even though the degrees of crystallinity were not increased in the development of the UHMWPE-TiO$_2$ nanocomposites, the semi-crystalline arrangement in the polymeric chains were modified by the presence of the TiO$_2$ NPs and the compression molding process.** As a confirmation of the change of crystal structures observed in XRD analysis, the use of FT-IR revealed a variation in the intensity of the methalyne rocking bands in correspondence to the addition of TiO$_2$ NPs. Furthermore, the appearance of carbon-oxygen interactions were detected in the vibrational modes at 1740 cm^{-1} (C=O) and 1250 cm^{-1} (C-O) assuring a positive dispersion of TiO$_2$ NPs inside the polymeric matrix.

In concordance to the results obtained with SEM images, **it was found out that the mechanical behavior of the sheet nanocomposites had an improvement along with the increment of the dopant concentration, reaching up to a 10% of maximum strain before failure and 30% of growth in the ultimate tensile strength** in samples with 0.75 wt. % or less. Matching the properties proposed in recent publications but, with less amount of TiO$_2$ NPs [69]. After reaching the concentration of 1 wt % the mechanical tensile properties diminished due to the presence of robust clusters of the dopant. A post manufacturing

process known as SPIF was used proving once again that the highest opposing forces to the deformation were found with the samples corresponding to 0.75 wt. % with a considerable decay at superior concentrations. Moreover, geometrical analysis were performed after machining illustrating that **the addition of TiO$_2$ NPs did not benefit the formability of the nanocomposite sheets. In fact some of them were reported to have a higher percentage of geometrical error,** this was originated due to an increase in the spring back recovery force behavior of the new nanocomposite. After evaluating the behavior of the UHMWPE-TiO$_2$ nanocomposite against SPIF deformations, **a fully functional, personalized, and biocompatible zygomatic bone prosthesis was produced with a geometrical error less than 2 mm**. Finally, a fibroblast cells culture analysis was performed and monitored after 24, 48, and 72-hours post seeding **reporting almost null cytotoxicity and a favorable environment for cells growth.**

Gathering up and as a last discussion, the answers to the hypothesis questions are written bellow with the clear idea of validating that the main objectives of this thesis were partially or fully accomplished.

1. Does the final mechanical and chemical properties of the UHMWPE-TiO$_2$ composites enhance the behavior of the neat UHMWPE matrix?

   Yes. Looking back to the results, there is a barely small increment in the mechanical properties of the new nanocomposite compared with the neat UHMWPE matrix. These results were compared with the analysis made by G. Celebi et. al achieving similar results but with less amount of TiO$_2$.

2. Will the proposed composite be suitable for cell adhesion and proliferation?

   Yes. Cell culture results point out that the surface of the UHMWPE-TiO$_2$ nanocomposites have an appropriate environment for human cells growth reporting null cytotoxicity and good adhesion.

3. Will single point incremental forming be acceptable for the production of personalized facial bone grafts ?

   Yes. Single point incremental forming technique is useful for this type of materials when the dimensions of the final piece does not overpass levels above 20 mm. If so, the spring back behavior will propitiate higher geometrical errors. This process is beneficial for the production of facial bone grafts since it is characterized to be fast, low cost and fittable to any patient.

4. Does the addition of TiO$_2$ NPs will modify the crystallization of the UHMWPE-TiO$_2$ composites?

   Yes. It was expected to increase the degrees of crystallinity with the addition of TiO$_2$ NPs but, according to the results obtained through DSC, XRD and FT-IR, the degrees of crystallinity in the nanocomposites barely change. However, the crystalline structures were modified from orthorhombic unit cells to a monoclinic structures.

As it is possible to observe there is a consistent validation of the hypothesis previously postulated in this thesis. What it is important to understand is that even though the mechanical

properties were not considerable improved, new properties were added to the production of zygomatic bone prosthesis such as: having a bio compatible environment, inert antibacterial behavior and photo catalytic eco-friendly responses.

5.1   Potential Directions (Future Work).

After the revision of few articles and the results obtained in this thesis, the future work for this branch of research must be guided to the understanding of different functionalization methodologies. By so doing, it is expected to increase the saturation point of TiO_2 NPs which will potentialize the already proved properties of the UHMWPE-TiO_2 nanocomposite. Furthermore, studies related with the use of new SPIF trajectories (G code), heating localized environments, external supports and dummy metallic layers must be develop to mitigate the geometrical error produced after 20 mm of machining depth. This will propitiate a controlled handling of the spring back recovery of the material. Moreover, the next step on the development of craniofacial prosthesis must be conducted to the objective of analyzing the behavior of the material during sterilization process, distribution, surgery and post surgical period. Additionally, scientific community must start thinking in the periodical study of the socioeconomic impact of these new developments to evaluate its relevance in the modern society. Finally, a deeper study must be made finding the relation between the superficial roughness of the material after machining with cellular adhesion. It is expected that the control in the superficial roughness of the material might define the amount of cellular adhesion and in the best scenario possible even the direction of adhesion.

Appendix A

Matlab Data Processing Codes.

MATLAB is defined as a fourth-generation programming language which combines a friendly computer environment with a high level programming code expressed in matrices and mathematical arrays [74]. Its invention was attributed to a computer science professor from the university of New Mexico, Cleve Moler, in the 1970s. MATLAB has been used since then in many fields for smart grids design, control systems, data processing, communication and dynamic modelling, just to mention a few.

The code presented in the next section was developed with the intended purpose of interpreting the signals obtained from the partial deformations registered by the dynamometer. The amplified signal, called from a previously generated excel format file, is cleaned by removing the noisy data originated from the vibration of the tool in the initial seconds of the test run. Then, the signal is smoothed through a local regression using weighted linear least squares and a 2nd degree polynomial model. Finally, the data was plotted and reported according to convenience.

A.1 SPIF Data and Smoothing Code.

```
clear all
clc
format long;
datosFz1=xlsread('fz0.xlsx');
datosFz1=flipud(datosFz1);
datosFz2=xlsread('fz025.xlsx');
datosFz2=flipud(datosFz2);
datosFz3=xlsread('fz05.xlsx');
datosFz3=flipud(datosFz3);
datosFz4=xlsread('fz075.xlsx');
datosFz4=flipud(datosFz4);
datosFz5=xlsread('fz1.xlsx');
datosFz5=flipud(datosFz5);
""..... FORCE VECTOR SIZE DEFINED.....""
numdatosFz1=size(datosFz1);
```

```
numdatosFz2=size(datosFz2);
numdatosFz3=size(datosFz3);
numdatosFz4=size(datosFz4);
numdatosFz5=size(datosFz5);
""....LAST VALUE OBTAINED FROM THE SAMPLE....""
ultimosampleFz1=numdatosFz1(1,1);
ultimosampleFz2=numdatosFz2(1,1);
ultimosampleFz3=numdatosFz3(1,1);
ultimosampleFz4=numdatosFz4(1,1);
ultimosampleFz5=numdatosFz5(1,1);
""....CORRECTION FACTOR OF ALL CURVES....""
ultimovalorFz1=datosFz1(ultimosampleFz1,1);
ultimovalorFz2=datosFz2(ultimosampleFz2,1);
ultimovalorFz3=datosFz3(ultimosampleFz3,1);
ultimovalorFz4=datosFz4(ultimosampleFz4,1);
ultimovalorFz5=datosFz5(ultimosampleFz5,1);
pendienteFz1=ultimovalorFz1/ultimosampleFz1;
pendienteFz2=ultimovalorFz2/ultimosampleFz2;
pendienteFz3=ultimovalorFz3/ultimosampleFz3;
pendienteFz4=ultimovalorFz4/ultimosampleFz4;
pendienteFz5=ultimovalorFz5/ultimosampleFz5;
vectorFz1=(1:1:ultimosampleFz1)';
vectorFz2=(1:1:ultimosampleFz2)';
vectorFz3=(1:1:ultimosampleFz3)';
vectorFz4=(1:1:ultimosampleFz4)';
vectorFz5=(1:1:ultimosampleFz5)';
fuerzaFz1=-pendienteFz1*vectorFz1+datosFz1;
fuerzaFz2=-pendienteFz2*vectorFz2+datosFz2;
fuerzaFz3=-pendienteFz3*vectorFz3+datosFz3;
fuerzaFz4=-pendienteFz4*vectorFz4+datosFz4;
fuerzaFz5=-pendienteFz5*vectorFz5+datosFz5;
""....INITIAL AND FINAL NOISY DATA ARE REMOVED....""
    for i=numdatosFz1(1,1):-1:1
    if(i==1)
            break;
        end
        if(fuerzaFz1(i-1,1)-fuerzaFz1(i,1)>15)
            ultimosampleFz1=i-5;
            break;
        end
    end
""....INITIAL FORCE 0 DATA REMOVED....""
    for i=1:ultimosampleFz1
        if(ultimosampleFz1==i)
            break;
```

```
            end
            if  (( fuerzaFz1 ( i +1,1)− fuerzaFz1 ( i ,1)) >6.1145498715)
                nuevosampleFz1=i ;
                break ;
            end
        end
"".....FZ2....""
    for  i=numdatosFz2 (1 ,1): − 1:1
            if ( i ==1)
                break ;
            end
            if ( fuerzaFz2 ( i −1,1)− fuerzaFz2 ( i ,1) >15)
                ultimosampleFz2=i −5;
                break ;
            end
        end
"".....INITIAL  FORCE  025  DATA REMOVED.....""
    for  i =1: ultimosampleFz2
            if ( ultimosampleFz2==i )
                break ;
            end
            if  (( fuerzaFz2 ( i +1,1)− fuerzaFz2 ( i ,1)) >6.1145498715)
                nuevosampleFz2=i ;
                break ;
            end
        end
"".....F3....""
    for  i=numdatosFz3 (1 ,1): − 1:1
            if ( i ==1)
                break ;
            end
            if ( fuerzaFz3 ( i −1,1)− fuerzaFz3 ( i ,1) >15)
                ultimosampleFz3=i −5;
                break ;
            end
        end
"".....INITIAL  FORCE  050  DATA REMOVED.....""
    for  i =1: ultimosampleFz3
            if ( ultimosampleFz3==i )
                break ;
            end
            if  (( fuerzaFz3 ( i +1,1)− fuerzaFz3 ( i ,1)) >6.1145498715)
                nuevosampleFz3=i ;
                break ;
            end
```

```
        end
  ""..... F4 ....." "
    for  i=numdatosFz4 (1 ,1): -1:1
        if ( i ==1)
            break ;
        end
        if ( fuerzaFz4 ( i -1,1)- fuerzaFz4 ( i ,1) >15)
            ultimosampleFz4=i -5;
            break ;
        end
    end
"" ..... INITIAL  FORCE  075  DATA  REMOVED ....." "
    for  i =1: ultimosampleFz4
        if ( ultimosampleFz4==i )
            break ;
        end
        if  (( fuerzaFz4 ( i +1,1)- fuerzaFz4 ( i ,1)) >6.1145498715)
            nuevosampleFz4=i ;
            break ;
        end
    end
"" ...... F5 ....." "
    for  i=numdatosFz5 (1 ,1): -1:1
        if ( i ==1)
            break ;
        end
        if ( fuerzaFz5 ( i -1,1)- fuerzaFz5 ( i ,1) >15)
            ultimosampleFz5=i -5;
            break ;
        end
    end
"" ..... INITIAL  FORCE  1  DATA  REMOVED ....." "
    for  i =1: ultimosampleFz5
        if ( ultimosampleFz5==i )
            break ;
        end
        if  (( fuerzaFz5 ( i +1,1)- fuerzaFz5 ( i ,1)) >6.1145498715)
            nuevosampleFz5=i ;
            break ;
        end
    end
"" ..... NEW  FORCE  VECTORS  WITHOUT  INITIAL  AND  FINAL  NOISY  DATA ....." "
tamnuevosdatosFz1 =( ultimosampleFz1 -nuevosampleFz1 )+1;
tamnuevosdatosFz2 =( ultimosampleFz2 -nuevosampleFz2 )+1;
tamnuevosdatosFz3 =( ultimosampleFz3 -nuevosampleFz3 )+1;
```

```
tamnuevosdatosFz4=(ultimosampleFz4-nuevosampleFz4)+1;
tamnuevosdatosFz5=(ultimosampleFz5-nuevosampleFz5)+1;
fuerzalimpiaFz1=zeros(tamnuevosdatosFz1,1);
fuerzalimpiaFz2=zeros(tamnuevosdatosFz2,1);
fuerzalimpiaFz3=zeros(tamnuevosdatosFz3,1);
fuerzalimpiaFz4=zeros(tamnuevosdatosFz4,1);
fuerzalimpiaFz5=zeros(tamnuevosdatosFz5,1);
fuerzalimpiaFz1(2:tamnuevosdatosFz1,1)=
                  fuerzaFz1(nuevosampleFz1+1:ultimosampleFz1,1);
fuerzalimpiaFz2(2:tamnuevosdatosFz2,1)=
                  fuerzaFz2(nuevosampleFz2+1:ultimosampleFz2,1);
fuerzalimpiaFz3(2:tamnuevosdatosFz3,1)=
                  fuerzaFz3(nuevosampleFz3+1:ultimosampleFz3,1);
fuerzalimpiaFz4(2:tamnuevosdatosFz4,1)=
                  fuerzaFz4(nuevosampleFz4+1:ultimosampleFz4,1);
fuerzalimpiaFz5(2:tamnuevosdatosFz5,1)=
                  fuerzaFz5(nuevosampleFz5+1:ultimosampleFz5,1);
fuerzaFz1=fuerzalimpiaFz1(1:tamnuevosdatosFz1);
fuerzaFz2=fuerzalimpiaFz2(1:tamnuevosdatosFz2);
fuerzaFz3=fuerzalimpiaFz3(1:tamnuevosdatosFz3);
fuerzaFz4=fuerzalimpiaFz4(1:tamnuevosdatosFz4);
fuerzaFz5=fuerzalimpiaFz5(1:tamnuevosdatosFz5);
tiempo=(1:1:tamnuevosdatosFz1)'*(0.003)*(10/3);
tiempo2=(1:1:tamnuevosdatosFz2)'*(0.003)*(10/3);
tiempo3=(1:1:tamnuevosdatosFz3)'*(0.003)*(10/3);
tiempo4=(1:1:tamnuevosdatosFz4)'*(0.003)*(10/3);
tiempo5=(1:1:tamnuevosdatosFz5)'*(0.003)*(10/3);
"".....SMOOTH NOISY DATA TO A SINGLE CURVE.....""
SuaveFz1=smoothdata(fuerzaFz1,'loess');
SuaveFz2=smoothdata(fuerzaFz2,'loess');
SuaveFz3=smoothdata(fuerzaFz3,'loess');
SuaveFz4=smoothdata(fuerzaFz4,'loess');
SuaveFz5=smoothdata(fuerzaFz5,'loess');
"".....PLOT ALL CURVES IN A SINGLE GRAPH.....""
figure(1)
axes('LineWidth',0.2,'FontWeight','bold','FontSize',16,
    'YMinorTick','on','YGrid','on','XMinorTick','on','XGrid','on',
    'TickDir','out');
set(gcf,'numbertitle','off','name','Fuerza Z');
grid\quad on
 plot(tiempo,SuaveFz1,'k','LineWidth',1);
 hold on
 plot(tiempo2,SuaveFz2,'b','LineWidth',1);
 plot(tiempo3,SuaveFz3,'c-.','LineWidth',1);
 plot(tiempo4,SuaveFz4,'r--','LineWidth',1);
```

```
plot(tiempo5,SuaveFz5,'g-.','LineWidth',1);
legend('UHMWPE','0.25','0.5','0.75','1.0');
    axis([0\quad 550\quad 0\quad 800]);
    xlabel('Time (seconds)','FontWeight','bold','FontSize',25);
ylabel('Force (Newtons)','FontWeight','bold','FontSize',25);
title('Normalized Fz','FontWeight','bold','FontSize',25);
grid\quad on
```

Appendix B

Polymeric Matrix Characterization Charts.

In this section it is expected to find few extra characterization analysis made to the polymeric matrix composite to assure certain properties during the manufacturing process of the samples. Some of them are not reported directly on the main content of this thesis but, they are added with the idea of having a better panorama of the chemical, mechanical and physical properties of the UHMWPE-TiO$_2$ composites.

B.1   TGA Thermogram.

TGA analysis was implemented to define the exact degradation temperatures of the UHMWPE matrix in two different atmospheres (Nitrogen and Air). Assuring that the parameters were suitable for manufacturing the UHMWPE-TiO$_2$ composites, without affecting the integrity of the material. Since that the research had to evaluate the pure nature of the composite, a test run was effectuated under a nitrogen atmosphere. Additionally, an air test run was studied replicating the manufacturing conditions suffered during the compression molding process.

Table B.1: Weight loss and onset temperatures registered in nitrogen and air atmospheres.

Atmosphere	Weight loss (%)	T_{onset} (°C)
Nitrogen	92.37	463.09
Air	93.67	464.33
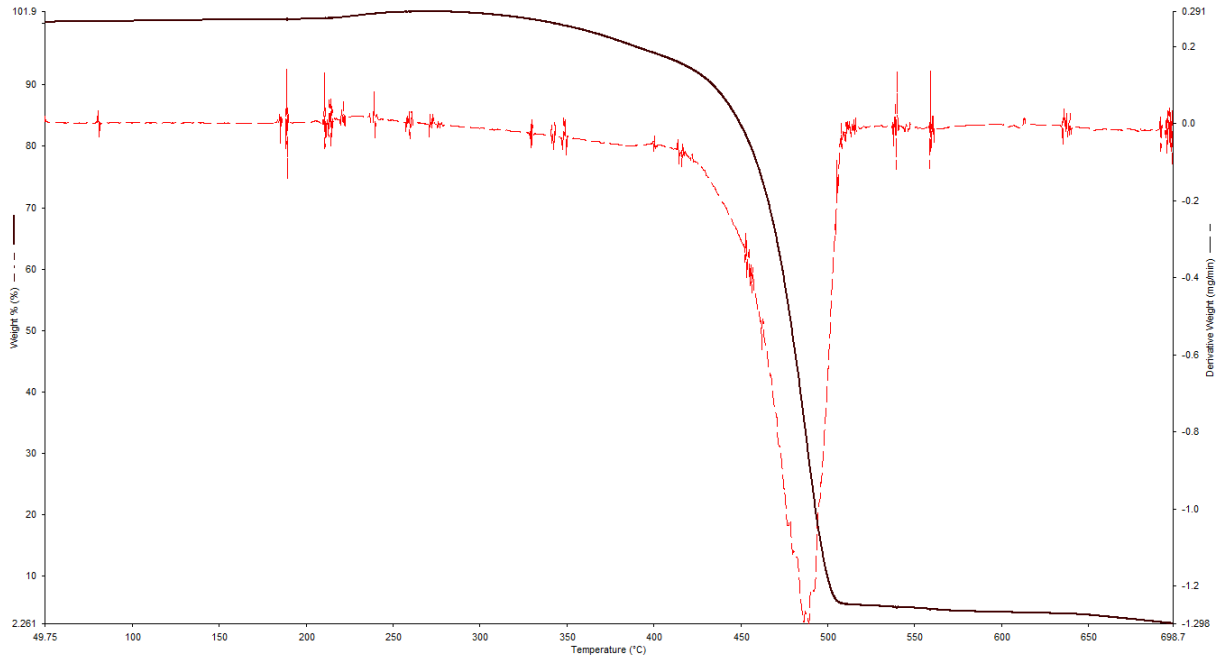
Figure B.1: TGA analysis of pure UHMWPE in an inert nitrogen atmosphere.The degradation temperature for the UHMWPE is above the temperature used for compression molding, assuring a proper handle of the melting temperatures without compromising the integrity of the polymeric chains.

B.2   XRD Spectra.

In this section a full comparison of all the diffraction planes observed in the UHMWPE-TiO$_2$ composite samples (Reference and M1-M4) is plotted with an additional measure corresponding to an UHMWPE matrix combined with functionalized carbon nano tubes at a low concentration.
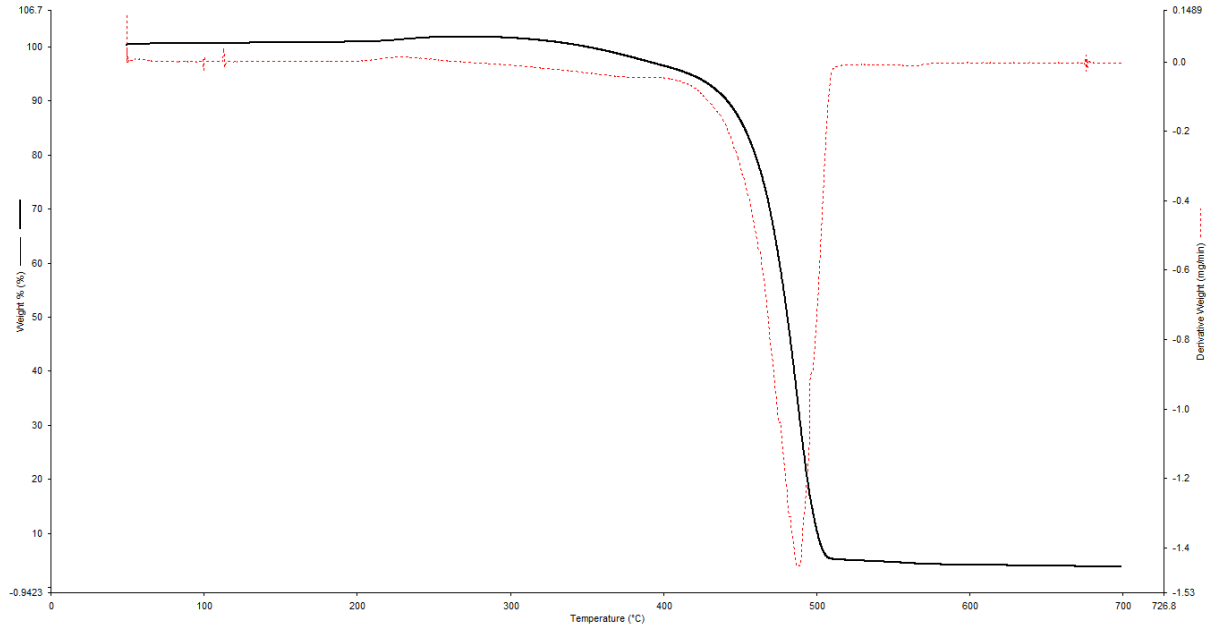
Figure B.2: TGA analysis of pure UHMWPE in an air atmosphere. Air atmosphere was used to simulate as precise as possible the environment experienced in compression molding. Even though, the degradation temperature is above the melting temperature used for the plates.

B.3 Roughness Analysis.

The information gathered from this study does not illustrate a clear change in the roughness of the material while the concentration of NPs is modified. But, as it is already know by many authors, the average roughness is increased in the all the samples (Reference and M1-M4) after the SPIF manufacturing process. This can be a positive opportunity for controlling the direction human cells growth. Further studies related with the surface roughness after SPIF procedures and the adhesion of human fibroblast must be made.

Table B.2: Minimum roughness before and after SPIF machining.

10 mm Tool										
	UHMWPE		0.25%		0.5%		0.75%		1.0%	
Direction	Ra	Rz	Ra	Rz	Ra	Rz	Ra	Rz	Ra	Rz
Longitudinal	17.14	108.64	11.52	72.8	10.96	81.1	11.16	85.2	11.34	73.96
Circumferential	11.64	51.9	7.13	50.49	6.53	34.41	6.94	42.8	10.09	49.89
5 mm Tool										
Longitudinal	11.74	48.57	9.68	59.87	7.16	43.75	6.34	38.62	8.87	54.5
Circumferential	7.41	37.69	6.46	35.06	5.28	34.75	4.55	32.19	7.83	43.39
Reference without SPIF										
Longitudinal	2.55	13.59	2.58	16.65	2.36	13.24	2.27	14.08	2.14	13.4
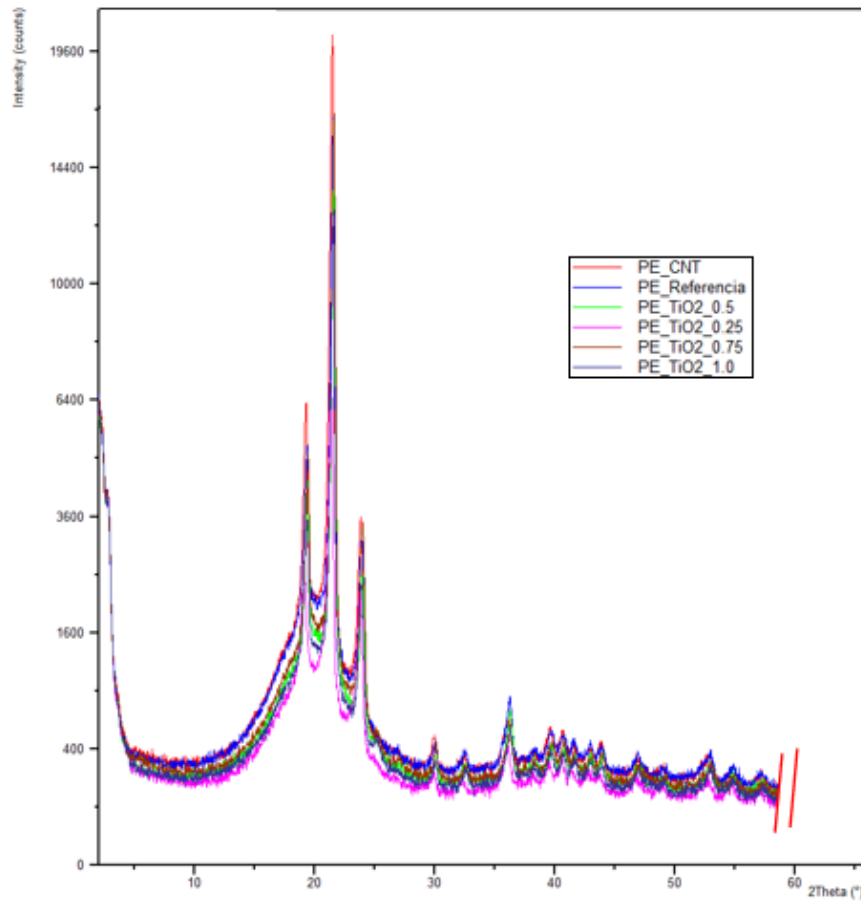
Figure B.3: XRD spectra of neat UHMWPE (Reference), UHMWPE-TiO$_2$ composites (M1-M4) and a comparison with UHMWPE-fMWCNTs (CNT).The change in crystallinity in the samples are not related with the addition of TiO$_2$ NPs. It is possible to observe the appearance of a monoclinic (001) crystal system due to the compression molding manufacturing process.

Appendix C

CNC Coding.

C.1 G-code used for the development of a 100 mm initial diameter part profile with a 28 mm depth, 80 mm generatrix, 5 mm tool diameter, 0 rpm, 300 mm/min feed rate and a 0.25 mm step down.

The code written in this appendix is an example of all the programs generated for the development of different part profiles. All of them follow the same code structure but with different dimensions and parameters previously calculated.

```
:0002
N0  G21  G92
N1  G17  G90  G54
N2  G00  X0.0  Y0.0
N3  G00   Z  50.0  S0  M03  F3000
N15  G00  Z  5.0

G00        X          47.5000
G00        Z          0.0000
G02        I          −47.5000          J  0.0
G00        X          47.2511
G00        Z          −0.2500
G03        I          −47.2511          J  0.0
G00        X          47.0044
G00        Z          −0.5000
G02        I          −47.0044          J  0.0
G00        X          46.7598
G00        Z          −0.7500
G03        I          −46.7598          J  0.0
G00        X          46.5174
G00        Z          −1.0000
```

G02	I	−46.5174	J	0.0
G00	X	46.2770		
G00	Z	−1.2500		
G03	I	−46.2770	J	0.0
G00	X	46.0388		
G00	Z	−1.5000		
G02	I	−46.0388	J	0.0
G00	X	45.8025		
G00	Z	−1.7500		
G03	I	−45.8025	J	0.0
G00	X	45.5683		
G00	Z	−2.0000		
G02	I	−45.5683	J	0.0
G00	X	45.3361		
G00	Z	−2.2500		
G03	I	−45.3361	J	0.0
G00	X	45.1059		
G00	Z	−2.5000		
G02	I	−45.1059	J	0.0
G00	X	44.8776		
G00	Z	−2.7500		
G03	I	−44.8776	J	0.0
G00	X	44.6513		
G00	Z	−3.0000		
G02	I	−44.6513	J	0.0
G00	X	44.4268		
G00	Z	−3.2500		
G03	I	−44.4268	J	0.0
G00	X	44.2043		
G00	Z	−3.5000		
G02	I	−44.2043	J	0.0
G00	X	43.9836		
G00	Z	−3.7500		
G03	I	−43.9836	J	0.0
G00	X	43.7647		
G00	Z	−4.0000		
G02	I	−43.7647	J	0.0
G00	X	43.5477		
G00	Z	−4.2500		
G03	I	−43.5477	J	0.0
G00	X	43.3325		
G00	Z	−4.5000		
G02	I	−43.3325	J	0.0
G00	X	43.1191		
G00	Z	−4.7500		

G03	I	−43.1191	J	0.0
G00	X	42.9074		
G00	Z	−5.0000		
G02	I	−42.9074	J	0.0
G00	X	42.6975		
G00	Z	−5.2500		
G03	I	−42.6975	J	0.0
G00	X	42.4893		
G00	Z	−5.5000		
G02	I	−42.4893	J	0.0
G00	X	42.2828		
G00	Z	−5.7500		
G03	I	−42.2828	J	0.0
G00	X	42.0780		
G00	Z	−6.0000		
G02	I	−42.0780	J	0.0
G00	X	41.8749		
G00	Z	−6.2500		
G03	I	−41.8749	J	0.0
G00	X	41.6735		
G00	Z	−6.5000		
G02	I	−41.6735	J	0.0
G00	X	41.4737		
G00	Z	−6.7500		
G03	I	−41.4737	J	0.0
G00	X	41.2756		
G00	Z	−7.0000		
G02	I	−41.2756	J	0.0
G00	X	41.0790		
G00	Z	−7.2500		
G03	I	−41.0790	J	0.0
G00	X	40.8841		
G00	Z	−7.5000		
G02	I	−40.8841	J	0.0
G00	X	40.6907		
G00	Z	−7.7500		
G03	I	−40.6907	J	0.0
G00	X	40.4989		
G00	Z	−8.0000		
G02	I	−40.4989	J	0.0
G00	X	40.3087		
G00	Z	−8.2500		
G03	I	−40.3087	J	0.0
G00	X	40.1200		
G00	Z	−8.5000		

G02	I	-40.1200	J	0.0
G00	X	39.9329		
G00	Z	-8.7500		
G03	I	-39.9329	J	0.0
G00	X	39.7472		
G00	Z	-9.0000		
G02	I	-39.7472	J	0.0
G00	X	39.5631		
G00	Z	-9.2500		
G03	I	-39.5631	J	0.0
G00	X	39.3804		
G00	Z	-9.5000		
G02	I	-39.3804	J	0.0
G00	X	39.1993		
G00	Z	-9.7500		
G03	I	-39.1993	J	0.0
G00	X	39.0196		
G00	Z	-10.0000		
G02	I	-39.0196	J	0.0
G00	X	38.8413		
G00	Z	-10.2500		
G03	I	-38.8413	J	0.0
G00	X	38.6645		
G00	Z	-10.5000		
G02	I	-38.6645	J	0.0
G00	X	38.4891		
G00	Z	-10.7500		
G03	I	-38.4891	J	0.0
G00	X	38.3152		
G00	Z	-11.0000		
G02	I	-38.3152	J	0.0
G00	X	38.1426		
G00	Z	-11.2500		
G03	I	-38.1426	J	0.0
G00	X	37.9714		
G00	Z	-11.5000		
G02	I	-37.9714	J	0.0
G00	X	37.8017		
G00	Z	-11.7500		
G03	I	-37.8017	J	0.0
G00	X	37.6333		
G00	Z	-12.0000		
G02	I	-37.6333	J	0.0
G00	X	37.4662		
G00	Z	-12.2500		

G03	I	-37.4662	J	0.0
G00	X	37.3006		
G00	Z	-12.5000		
G02	I	-37.3006	J	0.0
G00	X	37.1362		
G00	Z	-12.7500		
G03	I	-37.1362	J	0.0
G00	X	36.9732		
G00	Z	-13.0000		
G02	I	-36.9732	J	0.0
G00	X	36.8115		
G00	Z	-13.2500		
G03	I	-36.8115	J	0.0
G00	X	36.6512		
G00	Z	-13.5000		
G02	I	-36.6512	J	0.0
G00	X	36.4921		
G00	Z	-13.7500		
G03	I	-36.4921	J	0.0
G00	X	36.3344		
G00	Z	-14.0000		
G02	I	-36.3344	J	0.0
G00	X	36.1779		
G00	Z	-14.2500		
G03	I	-36.1779	J	0.0
G00	X	36.0227		
G00	Z	-14.5000		
G02	I	-36.0227	J	0.0
G00	X	35.8688		
G00	Z	-14.7500		
G03	I	-35.8688	J	0.0
G00	X	35.7161		
G00	Z	-15.0000		
G02	I	-35.7161	J	0.0
G00	X	35.5647		
G00	Z	-15.2500		
G03	I	-35.5647	J	0.0
G00	X	35.4145		
G00	Z	-15.5000		
G02	I	-35.4145	J	0.0
G00	X	35.2656		
G00	Z	-15.7500		
G03	I	-35.2656	J	0.0
G00	X	35.1179		
G00	Z	-16.0000		

G02	I	-35.1179	J	0.0
G00	X	34.9714		
G00	Z	-16.2500		
G03	I	-34.9714	J	0.0
G00	X	34.8261		
G00	Z	-16.5000		
G02	I	-34.8261	J	0.0
G00	X	34.6821		
G00	Z	-16.7500		
G03	I	-34.6821	J	0.0
G00	X	34.5392		
G00	Z	-17.0000		
G02	I	-34.5392	J	0.0
G00	X	34.3975		
G00	Z	-17.2500		
G03	I	-34.3975	J	0.0
G00	X	34.2570		
G00	Z	-17.5000		
G02	I	-34.2570	J	0.0
G00	X	34.1177		
G00	Z	-17.7500		
G03	I	-34.1177	J	0.0
G00	X	33.9795		
G00	Z	-18.0000		
G02	I	-33.9795	J	0.0
G00	X	33.8426		
G00	Z	-18.2500		
G03	I	-33.8426	J	0.0
G00	X	33.7067		
G00	Z	-18.5000		
G02	I	-33.7067	J	0.0
G00	X	33.5720		
G00	Z	-18.7500		
G03	I	-33.5720	J	0.0
G00	X	33.4385		
G00	Z	-19.0000		
G02	I	-33.4385	J	0.0
G00	X	33.3061		
G00	Z	-19.2500		
G03	I	-33.3061	J	0.0
G00	X	33.1748		
G00	Z	-19.5000		
G02	I	-33.1748	J	0.0
G00	X	33.0446		
G00	Z	-19.7500		

G03	I	−33.0446	J	0.0
G00	X	32.9156		
G00	Z	−20.0000		
G02	I	−32.9156	J	0.0
G00	X	32.7877		
G00	Z	−20.2500		
G03	I	−32.7877	J	0.0
G00	X	32.6608		
G00	Z	−20.5000		
G02	I	−32.6608	J	0.0
G00	X	32.5351		
G00	Z	−20.7500		
G03	I	−32.5351	J	0.0
G00	X	32.4105		
G00	Z	−21.0000		
G02	I	−32.4105	J	0.0
G00	X	32.2869		
G00	Z	−21.2500		
G03	I	−32.2869	J	0.0
G00	X	32.1645		
G00	Z	−21.5000		
G02	I	−32.1645	J	0.0
G00	X	32.0431		
G00	Z	−21.7500		
G03	I	−32.0431	J	0.0
G00	X	31.9227		
G00	Z	−22.0000		
G02	I	−31.9227	J	0.0
G00	X	31.8035		
G00	Z	−22.2500		
G03	I	−31.8035	J	0.0
G00	X	31.6853		
G00	Z	−22.5000		
G02	I	−31.6853	J	0.0
G00	X	31.5682		
G00	Z	−22.7500		
G03	I	−31.5682	J	0.0
G00	X	31.4521		
G00	Z	−23.0000		
G02	I	−31.4521	J	0.0
G00	X	31.3370		
G00	Z	−23.2500		
G03	I	−31.3370	J	0.0
G00	X	31.2230		
G00	Z	−23.5000		

G02	I	-31.2230	J	0.0
G00	X	31.1100		
G00	Z	-23.7500		
G03	I	-31.1100	J	0.0
G00	X	30.9981		
G00	Z	-24.0000		
G02	I	-30.9981	J	0.0
G00	X	30.8872		
G00	Z	-24.2500		
G03	I	-30.8872	J	0.0
G00	X	30.7773		
G00	Z	-24.5000		
G02	I	-30.7773	J	0.0
G00	X	30.6684		
G00	Z	-24.7500		
G03	I	-30.6684	J	0.0
G00	X	30.5605		
G00	Z	-25.0000		
G02	I	-30.5605	J	0.0
G00	X	30.4537		
G00	Z	-25.2500		
G03	I	-30.4537	J	0.0
G00	X	30.3478		
G00	Z	-25.5000		
G02	I	-30.3478	J	0.0
G00	X	30.2430		
G00	Z	-25.7500		
G03	I	-30.2430	J	0.0
G00	X	30.1391		
G00	Z	-26.0000		
G02	I	-30.1391	J	0.0
G00	X	30.0362		
G00	Z	-26.2500		
G03	I	-30.0362	J	0.0
G00	X	29.9343		
G00	Z	-26.5000		
G02	I	-29.9343	J	0.0
G00	X	29.8334		
G00	Z	-26.7500		
G03	I	-29.8334	J	0.0
G00	X	29.7335		
G00	Z	-27.0000		
G02	I	-29.7335	J	0.0
G00	X	29.6345		
G00	Z	-27.2500		

```
G03      I          −29.6345      J   0.0
G00      X          29.5365
G00      Z          −27.5000
G02      I          −29.5365      J   0.0
G00      X          29.4395
G00      Z          −27.7500
G03      I          −29.4395      J   0.0
G00      X          29.3435
G00      Z          −28.0000
G02      I          −29.3435      J   0.0
G00    Z  150.0
G00    Y  180.0
M05
M30
```

Appendix D

Geometrical Formability Error.

A representative image taken from each concentration (Reference sample and M1-M4 composites) are listed bellow. The main objective is to have a comparison in the geometrical error found per each concentration and according to different SPIF parameters. The procedure involve the use of a 3D scanner which allowed to obtain a virtual mesh (STL file) of the scanned topography. Care must be taken since it is a process that involves the use of adhesive dot references that will guide the software to obtain an exact measurement with the least error possible. If the reference dots are not placed uniformiously, the final mesh will present deformities or absence of nodes. Once the STL file was obtained, a software called GOM Inspect was used to define the distance difference between the scanned geometry mesh and the intended real computerized design (black lines). The colorized values, displayed in each figure, corresponds to the specific distance found at a particular point of the model. The numerical values are expressed in millimeters.

Figure D.1: SPIF geometrical errors in millimeters for UHMWPE-TiO$_2$ composite samples (10 mm tool diameter): (A) Reference (0%); (B) M1 (0.25%); (C) M2 (0.5%); (D) M3 (0.75%); (E) M4 (1%). The error between all samples behave partially equal with an average distance from bottom of 9.5 mm.
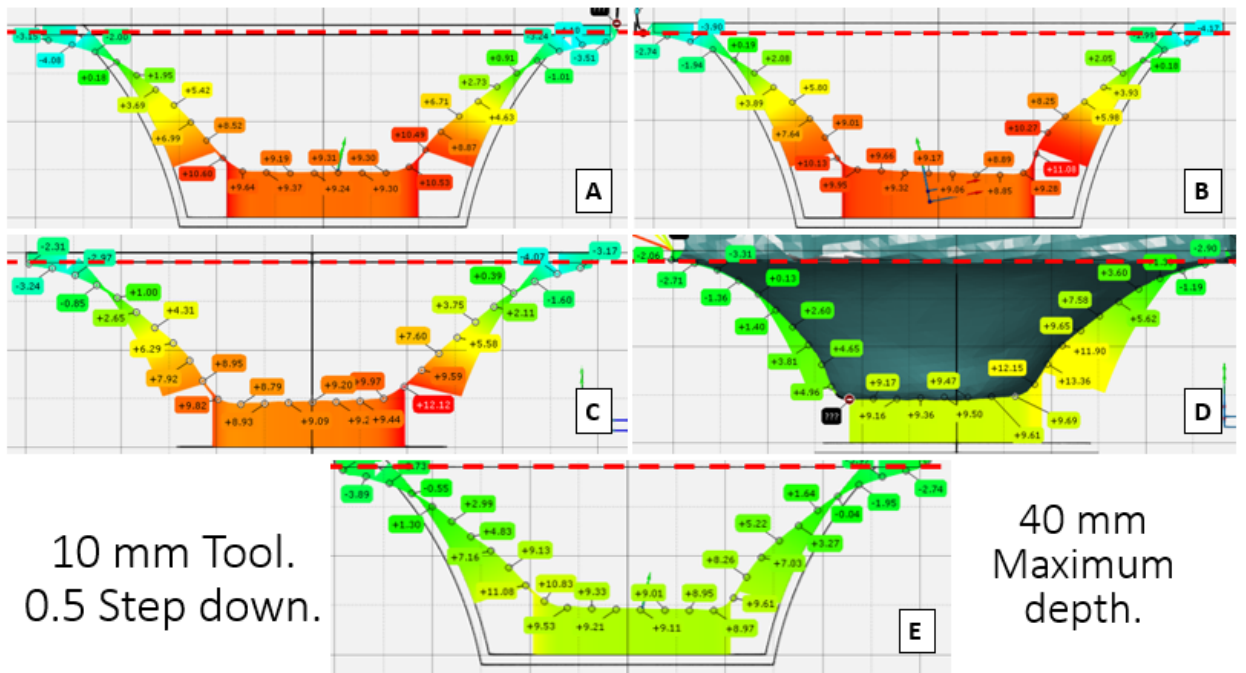

Figure D.2: SPIF geometrical errors in millimeters for UHMWPE-TiO$_2$ composite samples (5 mm tool diameter): (A) Reference (0%); (B) M1 (0.25%); (C) M2 (0.5%); (D) M3 (0.75%); (E) M4 (1%). The error between all samples behave partially equal with an average distance from bottom of 5.2 mm.
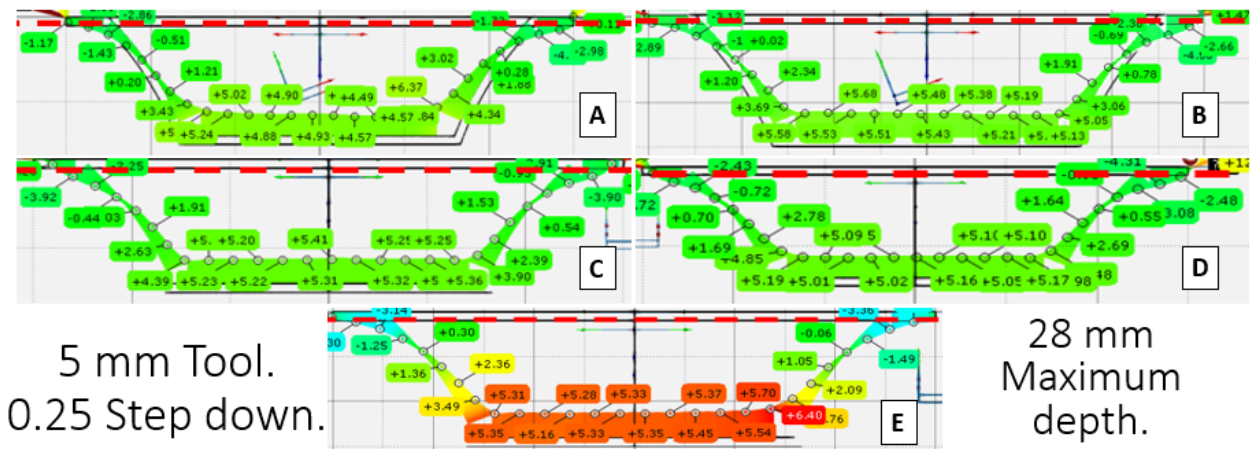
Bibliography

[1] W. Lao Gallardo and K. Sobalvarro Mojica, "Estudio de fracturas de malar, maxilar y mandÃbula de los egresos hospitalarios del 2010 a 2015 en la Caja Costarricense de Seguro Social.," *OdontologÃa Vital*, pp. 53 – 60, 06 2017.

[2] P. O. Ceallaigh, K. Ekanaykaee, C. J. Beirne, and D. W. Patton, "Diagnosis and management of common maxillofacial injuries in the emergency department. part 3: orbitozygomatic complex and zygomatic arch fractures," *Emergency Medicine Journal*, vol. 24, no. 2, p. 120122, 2007.

[3] E. Levine, L. C. Degutis, T. Pruzinsky, J. Shin, and J. A. Persing, "Quality of life and facial trauma: psychological and body image effects.," *Annals of plastic surgery*, vol. 54 5, pp. 502–10, 2005.

[4] R. Carrillo-Esper and J. M. Maeza-Marquez, "Trauma craneoencefalico," 2015.

[5] A. Khan, M. Jamal, A. Javed, M. Asim, and H. Sardar, "Frequency and etiology of zygomatic complex fractures in oral and maxillofacial trauma patients, a study done at ayub teaching hospital, abbottabad," *Pakistan Oral amp; Dental Journal*, vol. 37, pp. 543–546, Dec. 2017.

[6] M. Liviu Ciofu, D. Sulea, S. Luchian, and O. Boisteanu, "Aesthetic considerations in the reconstruction of orbito-zygomatic fractures," *Revista medico-chirurgicala a Societatii de Medici si Naturalisti din Iasi*, vol. 122, 04 2018.

[7] A. T. and J. C., "Osteoinduction, osteoconduction and osseointegration," *European spine journal : official publication of the European Spine Society, the European Spinal Deformity Society, and the European Section of the Cervical Spine Research Society*, vol. 10 Suppl 2, pp. S96–101, 11 2001.

[8] G. Centeno, I. Bagudanch, D. Morales-Palma, M. Garca-Romeu, B. Gonzalez-Perez-Somarriba, A. Martinez-Donaire, L. Gonzalez-Perez, and C. Vallellano, "Recent approaches for the manufacturing of polymeric cranial prostheses by incremental sheet forming," *Procedia Engineering*, vol. 183, pp. 180 – 187, 2017. 17th International Conference on Sheet Metal, SHEMET17.

[9] I. Bagudanch, L. M. Lozano-Snchez, L. Puigpins, M. Sabater, L. E. Elizalde, A. Elas-Ziga, and M. L. Garcia-Romeu, "Manufacturing of polymeric biocompatible cranial geometry by single point incremental forming," *Procedia Engineering*, vol. 132, pp. 267 – 273, 2015. MESIC Manufacturing Engineering Society International Conference 2015.

[10] A. Modabber, C. Legros, M. Rana, M. Gerressen, D. Riediger, and A. Ghassemi, "Evaluation of computer-assisted jaw reconstruction with free vascularized fibular flap compared to conventional surgery: a clinical pilot study," *The International Journal of Medical Robotics and Computer Assisted Surgery*, vol. 8, no. 2, p. 215220, 2011.

[11] N. Ayoub, A. Ghassemi, M. Rana, M. Gerressen, D. Riediger, F. Hlzle, and A. Modabber, "Evaluation of computer-assisted mandibular reconstruction with vascularized iliac crest bone graft compared to conventional surgery: a randomized prospective clinical trial," *Trials*, vol. 15, no. 1, p. 114, 2014.

[12] F. Wilde, K. Winter, K. Kletsch, K. Lorenz, and A. Schramm, "Mandible reconstruction using patient-specific pre-bent reconstruction plates: comparison of standard and transfer key methods," *International Journal of Computer Assisted Radiology and Surgery*, vol. 10, p. 129140, Sep 2014.

[13] S. Asgeirsson, "Method and kit for making prosthetic socket," U.S. Patent 7438843B2, Oct. 2008.

[14] P. Tack, J. Victor, P. Gemmel, and L. Annemans, "3d-printing techniques in a medical setting: a systematic literature review," *BioMedical Engineering OnLine*, vol. 15, no. 1, 2016.

[15] W. Donald R. Askeland, Pradeep P. Fulay, *The Science and Engineering of Materials, Sixth Edition*. Cengage Learning, 2011.

[16] S. M. Kurtz, *The UHMWPE handbook ultra-high molecular weight polyethylene in total joint replacement*. Academic Press, first ed., 2004.

[17] L. Costa, M. Luda, and L. Trossarelli, "Ultra high molecular weight polyetheneii. thermal- and photo-oxidation," *Polymer Degradation and Stability*, vol. 58, no. 1, pp. 41 – 54, 1997.

[18] A. R. Khataee and G. A. Mansoori, *Nanostructured Titanium Dioxide Materials: Properties, Preparation And Applications*. World Scientific, 2012.

[19] M. Malekshahi Byranvand, A. Nemati Kharata, L. Fatholahib, and Z. Malekshahi Beiranvandc, "A review on synthesis of nano-tio2 via different methods," vol. 3, pp. 1–9, 06 2013.

[20] D. Panaitescu, C. Radovici, M. Ghiurea, H. Paven, and M. Doina Iorga, "Influence of rutile and anatase tio_2 nanoparticles on polyethylene properties," vol. 50, pp. 196–202, 01 2011.

[21] G. C. Efe, I. Altinsoy, S. Trk, C. Bindal, and A. H. Ucisik, "Effect of particle size on microstructural and mechanical properties of uhmwpe-tio2 composites produced by gelation and crystallization method," *Journal of Applied Polymer Science*, vol. 136, no. 16, p. 47402, 2018.

[22] J. D. Menczel and R. B. Prime, *Thermal analysis of polymers: fundamentals and applications*. John Wiley, 2009.

[23] "Standard terminology relating to thermal analysis and rheology," standard, ASTM International, West Conshohocken, 2018.

[24] R. L. Danley, "New heat flux dsc measurement technique," *Thermochimica Acta*, vol. 395, no. 1, pp. 201 – 208, 2002.

[25] Perkin-Elmer, "Differential scanning calorimetry (dsc)." `https:// www.perkinelmer.com/CMSResources/Images/44-74542GDE_ DSCBeginnersGuide.pdf`, Aug. 2019.

[26] P. Gabbott, *Principles and applications of thermal analysis*. Blackwell Pub., 2008.

[27] M. Abd-Elghany and T. M. Klaptke, "A review on differential scanning calorimetry technique and its importance in the field of energetic materials," *Physical Sciences Reviews*, vol. 3, no. 4, 2018.

[28] W. D. Callister and D. G. Rethwisch, *Materials science and engineering: SI version*. John Wiley, 2 ed., 2015.

[29] M. Tilli and A. Haapalinna, "Chapter 1 - properties of silicon," in *Handbook of Silicon Based MEMS Materials and Technologies (Second Edition)* (M. Tilli, T. Motooka, V.-M. Airaksinen, S. Franssila, M. Paulasto-Krckel, and V. Lindroos, eds.), Micro and Nano Technologies, pp. 3 – 17, Boston: William Andrew Publishing, second edition ed., 2015.

[30] B. Cullity, *Elements of X-RAY diffraction, Second Edition*. Addison-Wesley, 1978.

[31] H. P. Klug and L. E. Alexander, *X-Ray Diffraction Procedures: For Polycrystalline and Amorphous Materials, Second Edition*. Wiley, 1974.

[32] G. E. Graksin, U. Ergn, and O. Deperlioglu, "The analysis of heart sounds and a pocket computer application via discrete fourier transform , fourier transforms - new analytical approaches and ftir strategies.," 2011.

[33] J. Quiroga Contreras, *Experimental Research of the Polyamidoamine Dendrimer as a Coating Layer for Micro-fabricated Silicon Bio-sensors*. PhD thesis, Instituto Tecnológico y Estudios Superiores de Monterrey, 2007.

[34] J. F. V. Vincent, *Structural biomaterials*. Princeton University Press, 2012.

[35] G. T. Mase, R. E. Smelser, and G. E. Mase, *Continuum mechanics for engineers*. CRC Press, 2019.

[36] S. R. S. Serope Kalpakjian, *Manufacturing, engineering and technology, Seventh Edition*. Pearson Education, 2013.

[37] W. D. Pilkey and O. H. Pilkey, *Mechanics of solids*. R.E. Krieger Pub. Co., 1986.

[38] K. Thornton, "Computational mechanics: Basic concepts and finite element method." 2014.

[39] O. C. Wells, F. K. LeGoues, and R. T. Hodgson, "Magnetically filtered lowloss scanning electron microscopy," *Applied Physics Letters*, vol. 56, no. 23, pp. 2351–2353, 1990.

[40] W. Zhou, R. Apkarian, Z. L. Wang, and D. Joy, "Fundamentals of scanning electron microscopy (sem)," *Scanning Microscopy for Nanotechnology*, p. 140, 2006.

[41] A. Khursheed, *Scanning Electron Microscope Optics And Spectrometers.* World Scientific, 2011.

[42] P. Martins, N. Bay, M. Skjoedt, and M. Silva, "Theory of single point incremental forming," *CIRP Annals*, vol. 57, no. 1, pp. 247 – 252, 2008.

[43] P. Martins, L. Kwiatkowski, V. Franzen, A. Tekkaya, and M. Kleiner, "Single point incremental forming of polymers," *CIRP Annals*, vol. 58, no. 1, pp. 229 – 232, 2009.

[44] T. McAnulty, J. Jeswiet, and M. Doolan, "Formability in single point incremental forming: A comparative analysis of the state of the art," *CIRP Journal of Manufacturing Science and Technology*, vol. 16, pp. 43 – 54, 2017.

[45] G. Hussain and L. Gao, "A novel method to test the thinning limits of sheet metals in negative incremental forming," *International Journal of Machine Tools and Manufacture*, vol. 47, no. 3-4, p. 419435, 2007.

[46] T. A. Marques, M. B. Silva, and P. A. F. Martins, "On the potential of single point incremental forming of sheet polymer parts," *The International Journal of Advanced Manufacturing Technology*, vol. 60, no. 1-4, p. 7586, 2011.

[47] W. Whitney and R. D. Andrews, "Yielding of glassy polymers: Volume effects," *Journal of Polymer Science Part C: Polymer Symposia*, vol. 16, no. 5, p. 29812990, 1967.

[48] R. Raghava, R. M. Caddell, and G. S. Y. Yeh, "The macroscopic yield behaviour of polymers," *Journal of Materials Science*, vol. 8, no. 2, p. 225232, 1973.

[49] R. Caddell, R. Raghava, and A. Atkins, "Pressure dependent yield criteria for polymers," *Materials Science and Engineering*, vol. 13, no. 2, p. 113120, 1974.

[50] V. P. Astakhov, "Surface integrity definition and importance in functional performance," *Surface Integrity in Machining*, p. 135, 2010.

[51] G. P. Petropoulos, C. N. Pandazaras, and J. P. Davim, "Surface texture characterization and evaluation related to machining," *Surface Integrity in Machining*, p. 3766, 2010.

[52] B. Bhushan, *Modern tribology handbook*, vol. 1. CRC Press, 2001.

[53] P. D. Inc., "Surface roughness terminology and parameters." `https://www.predev.com/pdffiles/surface_roughness_terminology_and_parameters.pdf`, Aug. 2019.

[54] E. Fernandez-Garcia, J. Guillem-Marti, C. F. Gutierrez-Gonzalez, A. Fernandez, M.-P. Ginebra, and S. Lopez-Esteban, "Osteoblastic cell response to spark plasma-sintered zirconia/titanium cermets," *Journal of Biomaterials Applications*, vol. 29, no. 6, p. 813823, 2014.

[55] D.-W. Lee, J.-G. Kim, M.-K. Kim, S. Ansari, A. Moshaverinia, S.-H. Choi, and J.-J. Ryu, "Effect of laser-dimpled titanium surfaces on attachment of epithelial-like cells and fibroblasts," *The Journal of Advanced Prosthodontics*, vol. 7, no. 2, p. 138, 2015.

[56] A. V. Ushakov, I. V. Karpov, L. Y. Fedorov, A. A. Lepeshev, A. A. Shaikhadinov, and V. G. Demin, "Nanocomposite material based on ultra-high-molecular-weight polyethylene and titanium dioxide electroarc nanopowder," *Theoretical Foundations of Chemical Engineering*, vol. 49, pp. 743–745, Sep 2015.

[57] G. C. Efe, C. Bindal, and A. Ucisik, "Characterization of uhmwpe-tio2 composites produced by gelation/crystallization method," *Acta Physica Polonica A*, vol. 132, p. 767769, Sep 2017.

[58] N. Mamidi, H. M. Leija, J. M. Diabb, I. L. Romo, D. Hernandez, J. V. Castrejn, O. M. Romero, E. V. Barrera, and A. E. Ziga, "Cytotoxicity evaluation of unfunctionalized multiwall carbon nanotubes-ultrahigh molecular weight polyethylene nanocomposites," *Journal of Biomedical Materials Research Part A*, vol. 105, no. 11, p. 30423049, 2017.

[59] B. Wunderlich, "Methodology of interpreting thermal analysis of polymers.," *Journal of Thermal Analysis Calorimetry*, vol. 106, no. 1, pp. 85 – 91, 2011.

[60] Y. Chen, Y. Qi, Z. Tai, X. Yan, F. Zhu, and Q. Xue, "Preparation, mechanical properties and biocompatibility of graphene oxide/ultrahigh molecular weight polyethylene composites," *European Polymer Journal*, vol. 48, no. 6, p. 10261033, 2012.

[61] H. Hagemann, R. G. Snyder, A. J. Peacock, and L. Mandelkern, "Quantitative infrared methods for the measurement of crystallinity and its temperature dependence: polyethylene," *Macromolecules*, vol. 22, no. 9, pp. 3600–3606, 1989.

[62] "Standard test method for tensile properties of plastics," standard, ASTM International, West Conshohocken, 2014.

[63] V. S. Le, A. Ghiotti, and G. Lucchetta, "Preliminary studies on single point incremental forming for thermoplastic materials," *International Journal of Material Forming*, vol. 1, no. S1, p. 11791182, 2008.

[64] L. Lozano-Snchez, A. Sustaita, M. Soto, S. Biradar, L. Ge, E. Segura-Crdenas, J. Diabb, L. Elizalde, E. Barrera, and A. Elas-Ziga, "Mechanical and structural studies on single point incremental forming of polypropylene-mwcnts composite sheets," *Journal of Materials Processing Technology*, vol. 242, pp. 218 – 227, 2017.

[65] B. P. Grady, F. Pompeo, R. L. Shambaugh, and D. E. Resasco, "Nucleation of polypropylene crystallization by single-walled carbon nanotubes," *The Journal of Physical Chemistry B*, vol. 106, no. 23, pp. 5852–5858, 2002.

[66] K. Russell, B. Hunter, and R. Heyding, "Monoclinic polyethylene revisited," *Polymer*, vol. 38, no. 6, pp. 1409 – 1414, 1997.

[67] S. Krimm, C. Y. Liang, and G. B. B. M. Sutherland, "Infrared spectra of high polymers. ii. polyethylene," *The Journal of Chemical Physics*, vol. 25, no. 3, pp. 549–562, 1956.

[68] V. G. Ngo, C. Bressy, C. Leroux, and A. Margaillan, "Synthesis of hybrid tio2 nanoparticles with well-defined poly(methylmethacrylate) and poly(tert-butyldimethylsilyl methacrylate) via the raft process," *Journal of Polymer*, vol. 50, pp. 3095–3102, 2009.

[69] G. C. Efe, I. Altinsoy, S. Trk, C. Bindal, and A. H. Ucisik, "Effect of particle size on microstructural and mechanical properties of uhmwpe-tio2 composites produced by gelation and crystallization method," *Journal of Applied Polymer Science*, vol. 136, no. 16, p. 47402, 2018.

[70] R. Pearce and J. Wood, *Sheet Metal Forming (New Manufacturing Processes Materials).* Adam Hilger, 1991.

[71] J. Duflou, B. Callebaut, J. Verbert, and H. D. Baerdemaeker, "Improved spif performance through dynamic local heating," *International Journal of Machine Tools and Manufacture*, vol. 48, no. 5, pp. 543 – 549, 2008. Advances in Sheet Metal Forming Applications.

[72] G. Palumbo and M. Brandizzi, "Experimental investigations on the single point incremental forming of a titanium alloy component combining static heating with high tool rotation speed," *Materials Design*, vol. 40, pp. 43 – 51, 2012.

[73] S. Mohanapriya, M. Mumjitha, K. PurnaSai, and V. Raj, "Fabrication and characterization of poly(vinyl alcohol)-tio2 nanocomposite films for orthopedic applications," *Journal of Mechanical Behavior of Biomedical Materials*, vol. 63, pp. 141–156, 2016.

[74] MathWorks, "Matlab cover page." `https://la.mathworks.com/products/matlab.html?s_tid=hp_products_matlab`, Aug. 2019.